Contents

Introduction

From molecular physics and organic chemistry to astrophysics, ability to measure the irradiance spectrum of an unknown source of light is of great interest for scientists. Both absorption and emission spectra reveal large amount of information about matter. They allow for the quantitative analysis of complex mixtures in the gas, liquid and solid phases, providing information about the chemical identity and the structure of molecules and atoms, but also about their physical environment (pressure and temperature). Optical spectroscopy is the field of sciences that studies systems by the electromagnetic radiation with which they interact or that they produce [1]. In polymer science, spectroscopic techniques are routinely used to study the functional groups present in compounds while almost all modern telescopes are equipped with a spectrometer to study the various phenomena that take place in stars and galaxies [2]. The study of interaction between light and atoms and simple molecules is at the origin of the discovery of quantum physics. Nowadays, novel spectroscopic techniques and instruments, with higher resolution and sensitivity, are used to push quantum physics to the very limits by studying atoms and molecules with always more and more details [3].

Optical spectroscopy involves the measurement of radiation intensity in terms of its frequency. Unfortunately, neither detectors nor electronic circuits are fast enough to respond to optical frequencies, and the magnitude of the radiation with respect to the frequency cannot be measured directly in the time domain [4]. Different kinds of instruments allow resolving light with regard to its frequency. Dispersive spectrometers make use of a prism or of a grating to spatially separate the spectral components of a light source. Photodetectors are then used to measure the intensity as a function of the frequency, *i.e.* the irradiance spectrum. Filter-based spectrometers rely on absorption or interference filters to transmit a selected range of frequencies to a photodetector. By switching filters, it is possible to reconstruct the light source spectrum. Filter-based spectrometers are mainly used in specific applications for which they are designed. In contrast to filter-based and dispersive spectrometers, Fourier transform spectrometers measure all the frequencies simultaneously by modulating the radiation in the time domain through interference. This measurement is the so-called interferogram of the light source. The spectrum is then recovered by applying a Fourier transform. Interference allows downconverting the signal from the optical frequency range to the radio frequency range, in which detectors and electronics work properly [4].

Advantages of Fourier transform spectrometers are numerous compared to dispersive and filter-based spectrometers. First, they allow to measure radiation at all frequencies simultaneously by measuring the interferogram of the light source under study. The Fourier transform is then applied on the interferogram to determine the contribution of each frequency to the signal. This advantage is known as the multiplex advantage, or Felgett's advantage. Second, for a given resolution, the throughput of a Fourier transform spectrometer, *i.e.* the allowable energy per unit of time that the system can let through, is always larger compared to dispersive and filter-based spectrometers. Thanks to this, spectra with higher signal-to-noise ratios can be acquired more rapidly with a Fourier transform spectrometer, compared to dispersive and filter-based instruments. This advantage is the so-called Jacquinot's advantage [5]. Finally, the frequency

scale of the spectrum is obtained via a reference laser in Fourier transform spectrometers. Thus, there is no need for any further calibration of the frequency scale for these instruments. This advantage is the Connes' advantage [5].

The goal of the master thesis was the design and fabrication of a high resolution Fourier transform spectrometer for the analysis of molecules in the gas phase. The setup presents some originality compared to more traditional instruments because of the use of a supercontinuum laser source instead of thermal light sources. Supercontinuum sources have the advantage of combining the brightness of lasers with the broad bandwidth of incandescent lamps. Moreover, supercontinuum sources are already collimated. Therefore, there is no need for collimating optics in the instrument [6]. This report presents the characterization of some of the elements of the experimental setup and the data processing pipeline which allowed retrieving the spectrum from the raw data recorded with our setup.

The report is divided into three main chapters. Chapter 1 aims at introducing the theoretical background necessary to understand the working principle of the instrument and the relation between the interferogram and the spectrum. In chapter 1, an intuitive way to understand the different features of the instrument is first presented, a more formal approach is given next.

Chapter 2 presents the setup that was built during the master thesis, along with experiments that were performed to characterize the behaviour of some of the elements that compose it. The optical configuration, aspects of the instrument design and the reference laser stabilization are addressed in distinct sections.

One of the major issues of Fourier transform spectroscopy is the data analysis. Each operation that is applied to the raw data will have consequences on the resulting spectrum. The goal of chapter 3 is to present the data analysis, from the data acquisition to the display of the spectrum on the computer screen.

Chapter 1

Theoretical background

Fourier transform spectrometers (FTS) are instruments working at the frontier of many disciplines, from optics and mechanics to data acquisition. One needs a certain background knowledge in all of these disciplines to comprehend all the issues behind Fourier transform spectroscopy.

Fourier transform spectrometers rely on a two-beam interferometer to measure a source spectrum. Introducing the Michelson interferometer permits to get a good insight of the working principle of all Fourier transform spectrometers. This is done in section 1.1.

The intensity measured at the output of a Michelson interferometer is modulated by varying the optical path difference between the two arms of the interferometer. The plot of the intensity as a function of the optical path difference cannot be interpreted directly. A mathematical operation must be performed to retrieve the information from the measurement. Section 1.2.1 explains what happens when a monochromatic source of light is injected into a Michelson interferometer. Generalization to polychromatic sources is performed in section 1.2.2 which also shows that the mathematical operation that must be applied on the interferogram to analyze it is the Fourier transform.

Every instrument somehow modifies the physical quantity that is studied, and FTS are subject to the same rule. Influence of the instrument on the real spectrum is described by means of its instrumental lineshape function (ILS). The concept is introduced in section 1.3, along with the effects of beam divergence and maximum optical path difference (OPD) on the real spectrum.

The signal is continuous, but its digital conversion obviously implies sampling which is the topic of section 1.4.

1.1 The Michelson interferometer

This section relies on references [4, 7, 8].

FTS are based on Michelson interferometers. The Michelson interferometer is depicted in Figure 1.1. In its simplest form, it consists of a beamsplitter (BS), a compensator (C) and two mirrors (M1 and M2). The ray coming from the source is split in two at the beamsplitter, one part is transmitted while the other is reflected. Both beams travel in free space until they reach one of the two mirrors. Both mirrors then reflect light beams back to the beamsplitter where they are recombined. Part of the recombined beam returns in direction of the source, the remaining part travels in the direction of the photodetector. Usually, one of the mirrors (M1) is maintained fixed and the other is mobile (M2) so that the relative distance traveled by light in the two arms before recombination can be varied. In other words, moving the mirror of one arm of

the interferometer allows to introduce a phase difference with respect to the second arm before recombination at the beamsplitter. Interference between the two beams occurs if they have a good spatial overlap from the beamsplitter to the photodetector. The measured intensity is then a function of the optical path difference, *i.e.* the difference of distance traveled by light in the two arms. The signal recorded at the photodetector for a purely monochromatic wave that undergoes an OPD equal to one wavelength is represented in Figure 1.1. It consists in a sine wave of period equal to the wavelength of the monochromatic source. A formal derivation of the interference pattern is detailed in the next section.

Light is subject to dispersion in the beamsplitter, leading to an optical path difference that depends on the wavelength λ. Indeed, light travels a greater distance in the material of the beamsplitter for one of the two arms. This is shown in Figure 1.1 where the beamsplitter is decomposed in a blue part corresponding to the material and a black part corresponding to the reflecting coating. One can see on this figure that light passes three times in the material of the beamsplitter for the arm with mirror M1 and only once for the arm with mirror M2. Adding a replica of the beamsplitter, with the exception of the reflecting coating, in the arm with mirror M2 ensures that light travels the same distance in the material for both arms. This replica is the so-called compensator. The compensator is mandatory in quantitative applications that involve broadband sources, as it is the case for Fourier transform spectroscopy [9]. Nowadays, the compensator and the beamsplitter are built together, resulting in a single optics on the optical bench.

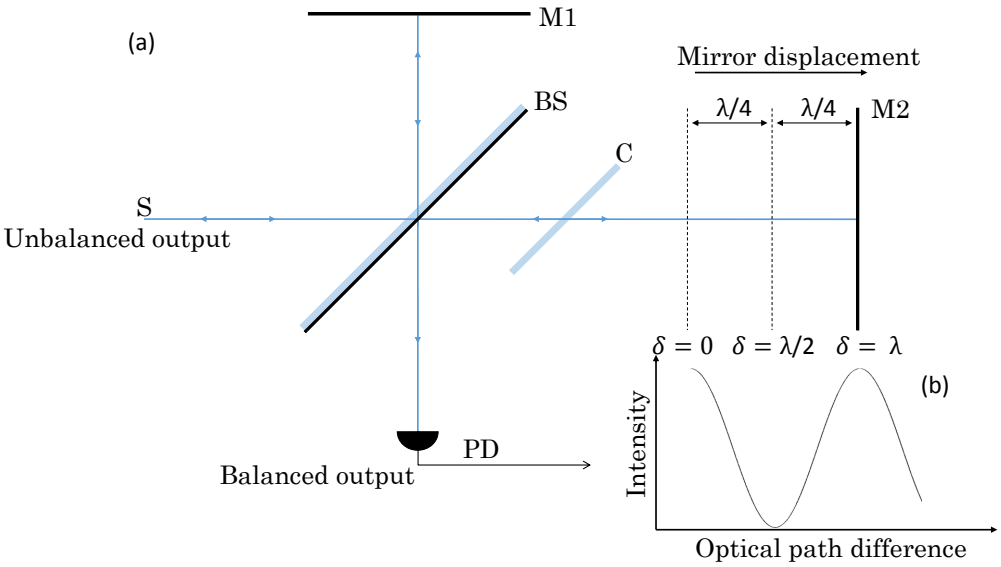

Figure 1.1: (a) schematic of a Michelson interferometer. BS stands for beamsplitter, C for compensator, PD for photodetector and S for source. M1 and M2 are respectively the fixed and the mobile mirrors. (b) Intensity at the photodetector with respect to retardation δ of a purely monochromatic source is shown. This figure is inspired from Ref. [10].

A Michelson interferometer has two outputs ports. The unbalanced output denotes the part of light which returns in direction of the source, whereas the balanced output corresponds to light that actually reaches the photodetector (PD). Both beams undergo a single reflection and a single transmission at the beamsplitter in the case of the balanced output. The source and the unbalanced output beams are overlapped in Figure 1.1, avoiding the recording of the signal of the unbalanced output. If retro-reflectors are used instead of mirrors, the source and the unbalanced output are spatially separated, allowing the measurement of the two output signals. This configuration is depicted in Figure 1.2. Advantages of measuring the unbalanced output and the balanced output simultaneously are emphasized in section 1.2.1.

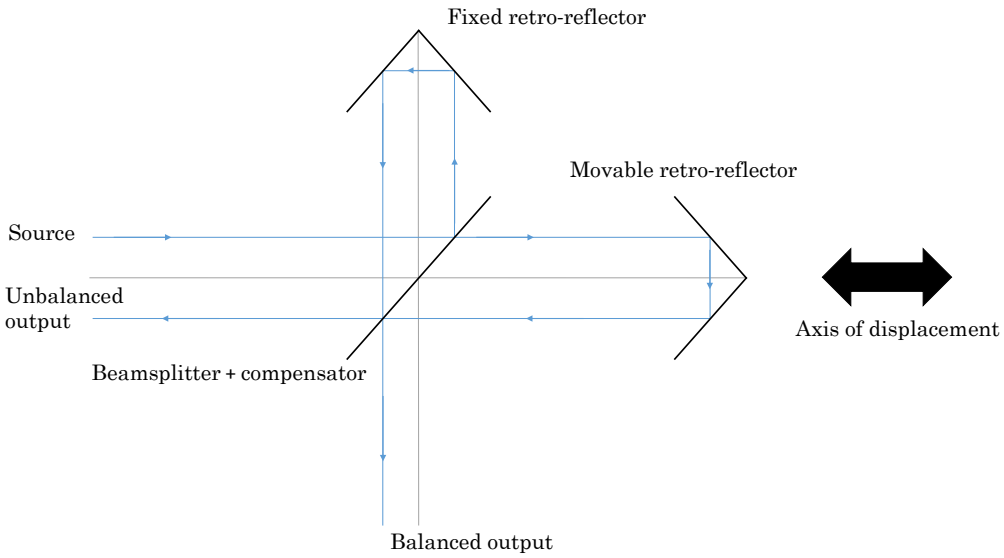

Figure 1.2: schematic of a Michelson interferometer using retro-reflectors. The grey lines correspond to the two optical axes of the interferometer.

The two optical axes of the interferometer are shown in Figure 1.2. They are imaginary lines that correspond to the directions along which light travels in the setup. They make a 45-degrees angle with the beamsplitter. For the arm with the movable retro-reflector, the optical axis also corresponds to the locus engendered by the translation of the apex of the retroreflector during its displacement.

1.2 Generation of an interferogram

This section introduces the main concepts of Fourier transform spectroscopy step by step. Section 1.2.1 first describes what happens when a purely monochromatic source is injected into an FTS by evaluating the intensity measured at the two outputs as a function of the mirror displacement. This measurement is the so-called interferogram. The usefulness of measuring both outputs is pointed out. Section 1.2.2 then generalizes the results for a polychromatic source and it demonstrates how to recover the source irradiance spectrum from the interferogram.

1.2.1 Interferogram of a monochromatic source

This section relies on references [4, 9].

In order to understand what happens in a Fourier transform spectrometer and how the spectrum is related to the Fourier transform of the measured signal, it is necessary to subdivide the problem by considering each arm separately. Figure 1.3 supports the demonstration given just below. It is convenient to have a look at it while reading the demonstration. This figure shows the influence of each optical component on the amplitude of the electric field of a source of monochromatic radiation producing an infinitely narrow and perfectly collimated beam. The importance of light collimation will appear obvious after the reading of section 1.3.2. This hypothesis allows considering plane waves which propagate parallel to the optical axes.

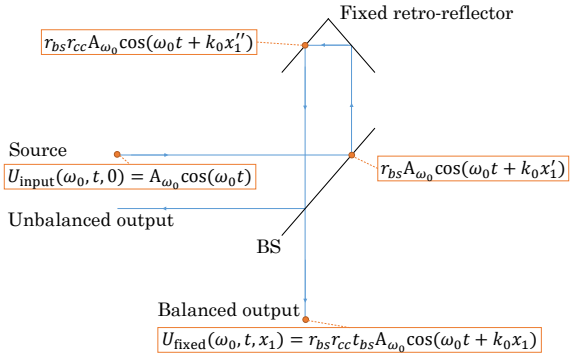

(a) Arm with the static retro-reflector.

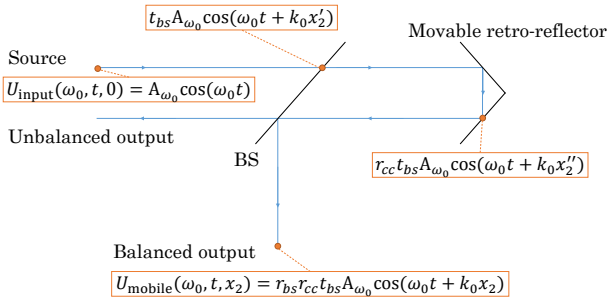

(b) Arm with the movable retro-reflector.

Figure 1.3: Expression of the electric field of a monochromatic source of angular frequency ω_0 at several positions (red dots) in the interferometer. The two arms are treated separately. $A_{\tilde{\nu}_0}$ is the electric field amplitude, r_{cc} is the effective reflection coefficient of the retro-reflectors, r_{bs} and t_{bs} are respectively the external reflection coefficient and the transmission coefficient of the beamsplitter.

Balanced output

Light emitted by a source of monochromatic radiation producing an infinitely narrow and perfectly collimated beam is best described by its electric field U which depends on both time t and position x :

$$U(\omega_0, t, x) = A_{\tilde{\nu}_0}\cos(\omega_0 t + 2\pi \mathrm{j}\tilde{\nu}_0 x) = \frac{1}{2}A_{\tilde{\nu}_0}\mathrm{e}^{\mathrm{j}\omega_0 t}\mathrm{e}^{2\pi \mathrm{j}\tilde{\nu}_0 x} + \text{c.c.}, \tag{1.1}$$

where ω_0 is the angular frequency of the monochromatic wave and $A_{\tilde{\nu}_0}$ is its amplitude. The notation c.c. stands for conjugate complex. Equation (1.1) is the equation of a plane wave propagating parallel to the optical axes. The electric field depends on the source angular frequency ω_0, the time t and the position x in which the field is observed. Finally, $\tilde{\nu}_0$ denotes the wavenumber of the wave and is defined as the inverse of the wavelength, *i.e.* $\tilde{\nu}_0 = \frac{1}{\lambda_0}$. The wavenumber is linked to the angular frequency by the following equation :

$$\omega_0 = 2\pi c\tilde{\nu}_0, \tag{1.2}$$

with c the velocity of light.

The source is located in $x = 0$ and the electric field U_{input} at the source is therefore given by :

$$U_{\text{input}}(\omega_0, t, 0) = A_{\tilde{\nu}_0}\cos(\omega_0 t) = \frac{1}{2}A_{\tilde{\nu}_0}\mathrm{e}^{\mathrm{j}\omega_0 t} + \text{c.c.}, \tag{1.3}$$

The beamsplitter splits the beam in two, one part is transmitted while the other is reflected on its surface. They next travel a certain distance in free space before being reflected back to the beamsplitter where they recombine. The electric field at the balanced output is obtained by summing the electric fields of both arms and is therefore given by :

$$U_{\text{balanced output}} = U_{\text{fixed}} + U_{\text{mobile}}. \tag{1.4}$$

Based on Figure 1.3, U_{fixed} and U_{mobile} at the photodetector and at time t are given by :

$$U_{\text{fixed}}(\omega_0, t, x_1) = \frac{1}{2}A_{\tilde{\nu}_0}r_{cc}r_{bs}t_{bs}\mathrm{e}^{\mathrm{j}\omega_0 t}\mathrm{e}^{2\pi \mathrm{j}\tilde{\nu}_0 x_1} + \text{c.c.}, \tag{1.5}$$

$$U_{\text{mobile}}(\omega_0, t, x_2) = \frac{1}{2}A_{\tilde{\nu}_0}r_{cc}r_{bs}t_{bs}\mathrm{e}^{\mathrm{j}\omega_0 t}\mathrm{e}^{2\pi \mathrm{j}\tilde{\nu}_0 x_2} + \text{c.c.}, \tag{1.6}$$

where r_{bs} is the external amplitude reflection coefficient at the beamsplitter, t_{bs} is the transmission coefficient of the beamsplitter and r_{cc} is the effective reflection coefficient of the retro-reflector which takes into account the multiple reflections taking place in the retro-reflector. Light travels a distance x_1 between the source and the photodetector if it goes through the arm with the fixed retro-reflector. The distance in between the source and the photodetector is equal to x_2 in the case of the arm with the movable retro-reflector. The difference $\delta = x_2 - x_1$ is the optical path difference (OPD) or retardation. If light travels the same distance in both arms, the path difference is equal to zero, and the movable mirror is said to be at zero path difference (ZPD).

Injecting equations (1.5) and (1.6) into equation (1.4) leads to :

$$U_{\text{balanced output}} = \frac{1}{2} A_{\tilde{\nu}_0} r_{cc} r_{bs} t_{bs} \mathrm{e}^{\mathrm{j}\omega_0 t} \left(\mathrm{e}^{2\pi \mathrm{j} \tilde{\nu}_0 x_1} + \mathrm{e}^{2\pi \mathrm{j} \tilde{\nu}_0 x_2} \right) + \text{c.c.}. \tag{1.7}$$

The photodetector does not directly measure the light electric or magnetic field but rather a time-averaged intensity of the signal. This is due to the very high frequencies of optical signals (10^5 GHz for a 3000 nm wavelength), compared to the bandwidth of the photodetector (up to a few GHz for the best detectors available). The time-averaged intensity at the balanced output is given by the following relationship :

$$I_{\text{balanced output}} = \left| U_{\text{balanced output}} \right|^2, \tag{1.8}$$

Injecting equation (1.7) in equation (1.8) leads to :

$$I_{\text{balanced output}}(\delta, \tilde{\nu}_0) = 2A_{\tilde{\nu}_0}^2 R_{cc} R_{bs} T_{bs} \left(1 + \cos\left(2\pi \tilde{\nu}_0 \delta\right)\right) = 2I_{\tilde{\nu}_0} R_{cc} R_{bs} T_{bs} \left(1 + \cos\left(2\pi \tilde{\nu}_0 \delta\right)\right), \tag{1.9}$$

where $R_{bs} = r_{bs}^2$ and $R_{cc} = r_{cc}^2$ are the intensity reflection coefficients of the beamsplitter and of the retro-reflectors, and $T_{bs} = t_{bs}^2$ is the intensity transmission coefficient of the beamsplitter. $I_{\tilde{\nu}_0}$ stands for the intensity of the input radiation of wavenumber $\tilde{\nu}_0$. An ideal beamsplitter exhibits a 50% transmittance and a 50% reflectance on its entire bandwidth. Equation (1.9) can be rewritten by regrouping all the factors before the brackets in a single wavenumber-dependent factor $B_{\tilde{\nu}_0}$, leading to the following relation :

$$I_{\text{balanced output}}(\delta, \tilde{\nu}_0) = B_{\tilde{\nu}_0} \left(1 + \cos\left(2\pi \tilde{\nu}_0 \delta\right)\right). \tag{1.10}$$

The intensity at the output is composed of a constant term and a modulated one. The modulated term is the so-called interferogram and it is the one of interest in spectroscopic measurements. For a monochromatic source, intensity at the photodetector varies in a sinusoidal manner with respect to the optical path difference, as depicted in Figure 1.4. It is convenient to remove the constant term from the signal since it is unnecessary and it adds noise at the amplifier. It can be done either with the use of a high-pass filter or with the use of both the balanced and the unbalanced output, as it will be explained in the next section. The interferogram is then given by :

$$I_{\text{balanced output}}(\delta, \tilde{\nu}_0) = B_{\tilde{\nu}_0} \cos\left(2\pi \tilde{\nu}_0 \delta\right). \tag{1.11}$$

Unbalanced output

There is neither creation nor destruction of energy in the process. Instead, energy is redistributed between balanced and unbalanced outputs depending on the retardation and they are therefore complementary. For an input of intensity $I_{\tilde{\nu}_0}$ and if there are only losses at the retro-reflectors, then the sum of the two outputs is constant and equal to $R_{cc} I_{\tilde{\nu}_0}$:

$$I_{\text{balanced output}} + I_{\text{unbalanced output}} = \text{Constant} = R_{cc} I_{\tilde{\nu}_0}, \tag{1.12}$$

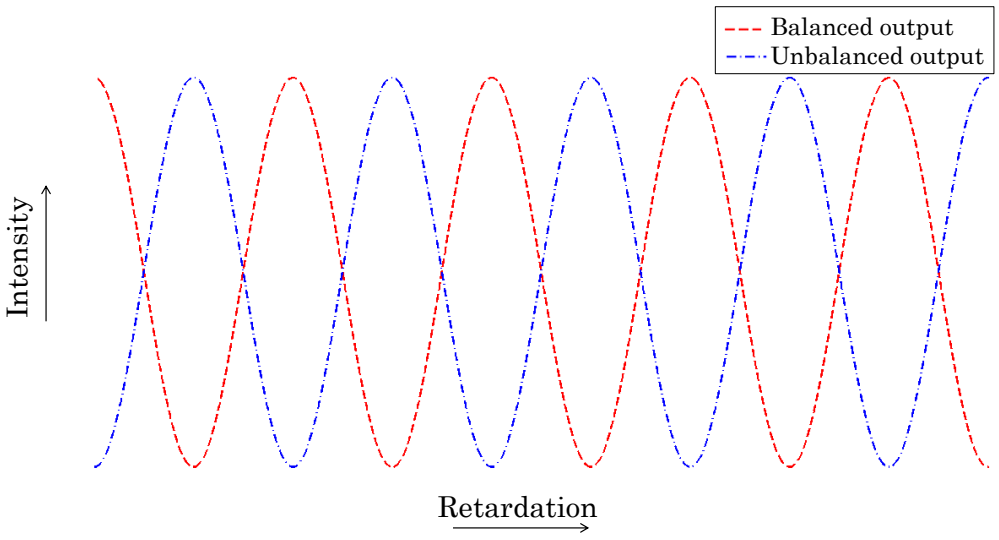

Figure 1.4: Intensity with respect to retardation for a purely monochromatic source.

Injecting equation (1.9) into equation (1.12) and solving for $I_{\text{unbalanced output}}$ leads to :

$$I_{\text{unbalanced output}} = I_{\tilde{\nu}_0} R_{cc} \left(1 - 4R_{bs}T_{bs}\left(\frac{1+\cos\left(2\pi\tilde{\nu}_0\delta\right)}{2}\right)\right). \tag{1.13}$$

This expression can be rewritten as follows :

$$I_{\text{unbalanced output}} = 4I_{\tilde{\nu}_0} R_{cc}R_{bs}T_{bs}\left(\frac{1-\cos\left(2\pi\tilde{\nu}_0\delta\right)}{2}\right) + I_{\tilde{\nu}_0} R_{cc}\left(1 - 4R_{bs}T_{bs}\right). \tag{1.14}$$

The unbalanced output is out of phase of π compared to the signal of the balanced output, *i.e.* equation (1.9). Both outputs thus contain the same information because they receive about the same amount of photons. Intensity at the output of the interferometer for a purely monochromatic source is shown in Figure 1.4 as well.

Subtracting the unbalanced output from the balanced output allows doubling the signal strength and to get rid of most of the dc term which is responsible for adding extra noise to the signal :

$$I_{\text{balanced output}} - I_{\text{unbalanced output}} = 4R_{cc}R_{bs}T_{bs}\cos\left(2\pi\tilde{\nu}_0\delta\right) - I_{\tilde{\nu}_0} R_{cc}\left(1 - 4R_{bs}T_{bs}\right). \tag{1.15}$$

In the previous equation, the term which is subtracted is nearly equal to zero because $R_{bs} \approx T_{bs} \approx \frac{1}{2}$.

Another advantage of measuring both outputs is to remove time-domain intensity variations of the source by adding both signals together.

1.2.2 Interferogram of a polychromatic source

This section relies on references [4, 11].

In the case of polychromatic sources, that is when more than one frequency is emitted by the source, the measured interferogram is a superposition of the interferograms of each different frequency. The participation of each individual interferogram to the measured interferogram

is weighted by a factor named spectral irradiance. Spectral irradiance characterizes the total amount of radiant power going through a unit area at wavenumber $\tilde{\nu}$. The objective of a Fourier transform spectrometer is to measure the spectral irradiance of a source on an interval of wavenumbers. The plot of the source spectral irradiance with respect to the wavenumber is the so-called spectrum. As mentioned in the previous section, optical elements and detectors are frequency-dependent, and the setup therefore modifies the true spectrum of the source. The measured irradiance spectrum is denoted by $B(\tilde{\nu})$. Influence of several instrument parameters on the true irradiance spectrum will be studied in section 1.3.

For a continuum source, the intensity measured at a retardation δ is obtained by integrating equation (1.11) over all the wavenumbers, leading to :

$$I(\delta) = \int_0^{+\infty} B(\tilde{\nu}) \cos(2\pi\tilde{\nu}\delta)\, \mathrm{d}\tilde{\nu}. \tag{1.16}$$

The quantity of interest is the spectral distribution $B(\tilde{\nu})$, which can be obtained by taking the inverse transform of the interferogram, that is :

$$B(\tilde{\nu}) = \int_0^{+\infty} I(\delta) \cos(2\pi\tilde{\nu}\delta)\, \mathrm{d}\delta. \tag{1.17}$$

Equations (1.16) and (1.17) only consider positive optical path differences and positive wavenumbers. An interferogram that only takes positive optical path differences is said to be single-sided. Since retarding one beam or the other must be equivalent, the interferogram is ideally an even function of retardation, *i.e.* $I(-\delta) = I(\delta)$. A double-sided interferogram is an interferogram measured on a symmetrical range of retardation around the zero path difference (ZPD). Extending the integral boundaries of equation (1.16) to minus infinity leads to :

$$I(\delta) = \frac{1}{2} \int_{-\infty}^{+\infty} B(\tilde{\nu}) \cos(2\pi\tilde{\nu}\delta)\, \mathrm{d}\tilde{\nu}. \tag{1.18}$$

Although negative wavenumbers have no physical meaning, it is necessary to extend integral boundaries from minus infinity to plus infinity in equation (1.17) to ensure complete symmetry in transforming back and forth from the interferogram domain to the spectral domain. This extension can be easily done since $\cos(2\pi\tilde{\nu}\delta) = \cos(-2\pi\tilde{\nu}\delta)$, $B(\tilde{\nu})$ should just be an even function of $\tilde{\nu}$ (*i.e.* $B(\tilde{\nu}) = B(-\tilde{\nu})$) to produce identical interferograms.

Equation (1.17) simply becomes

$$B(\tilde{\nu}) = \frac{1}{2} \int_{-\infty}^{+\infty} I(\delta) \cos(2\pi\tilde{\nu}\delta)\, \mathrm{d}\delta. \tag{1.19}$$

In practice, it is more convenient to use Fourier transforms instead of cosine Fourier transforms. Equations (1.18) and (1.19) are then given by :

$$I(\delta) = \frac{1}{2} \int_{-\infty}^{+\infty} B(\tilde{\nu}) \mathrm{e}^{-2\pi \mathrm{j} \tilde{\nu}\delta} \mathrm{d}\tilde{\nu}, \tag{1.20}$$

$$B(\tilde{\nu}) = \frac{1}{2} \int_{-\infty}^{+\infty} I(\delta) \mathrm{e}^{2\pi \mathrm{j} \tilde{\nu}\delta} \mathrm{d}\delta. \tag{1.21}$$

The use of equation (1.21) instead of equation (1.17) does not modify the spectrum as long as $I(\delta)$ is an even function of δ. This can be shown by rewriting $I(\delta)$ as a sum of an even function $E(\delta)$ and an odd function $O(\delta)$:

$$I(\delta) = \frac{1}{2}\left[I(\delta) + I(-\delta)\right] + \frac{1}{2}\left[I(\delta) - I(-\delta)\right] = E(\delta) + O(\delta). \tag{1.22}$$

Injecting the previous equation in equation (1.21) leads to

$$B(\tilde{\nu}) = \int_{-\infty}^{+\infty} (E(\delta) + O(\delta))\, \mathrm{e}^{2\pi \mathrm{j}\tilde{\nu}\delta} \mathrm{d}\delta, \tag{1.23}$$

or equivalently :

$$B(\tilde{\nu}) = \int_{-\infty}^{+\infty} \left(\frac{1}{2}\left[I(\delta) + I(-\delta)\right] + \frac{1}{2}\left[I(\delta) - I(-\delta)\right] \right) (\cos(2\pi\tilde{\nu}\delta) + \mathrm{j}\sin(2\pi\tilde{\nu}\delta))\, \mathrm{d}\delta. \tag{1.24}$$

Since the integral of an odd function on a symmetrical interval with respect to 0 is vanishing, equation 1.24 is equal to :

$$B(\tilde{\nu}) = \int_{-\infty}^{+\infty} E(\delta) \cos\left(2\pi\tilde{\nu}\delta\right) \mathrm{d}\delta + \mathrm{j} \int_{-\infty}^{+\infty} O(\delta) \sin\left(2\pi\tilde{\nu}\delta\right) \mathrm{d}\delta. \tag{1.25}$$

As long as $I(\delta)$ is even, that is $O(\delta) = 0$, and real, $B(\tilde{\nu})$ is real.

Even if all the information on the source spectrum can be theoretically recovered from the positive retardation interferogram by evaluating equation (1.16), the use of equation (1.21) exhibits two main advantages. Firstly, information about the phase and the ability to correct it are mandatory and imply the use of Fourier transforms instead of cosine Fourier transforms. Phase errors arise from the discrete sampling of the interferogram. Also, dispersive phenomena taking place in optical elements make the optical path difference to be a function of the wavenumber and they are therefore at the origin of phase errors too [9]. These phase errors would modify the spectrum if negative retardation was not considered. Phase correction and its implementation are the topics of section 3.2.6. Secondly, it is computationally more efficient to evaluate Fourier transforms instead of cosine Fourier transforms.

Figure 1.5 shows the double-sided interferogram of a blackbody source with its associated spectrum. All the waves interfere constructively at ZPD. It results in a bright central fringe, the so-called centerburst. On both sides of that peak, there are ripples that extend to large optical path differences. These ripples contain most of the information, as it will be explained in section 1.3.1. The spectrum is recovered from the interferogram by taking its Fourier transform following a procedure described in chapter 3.

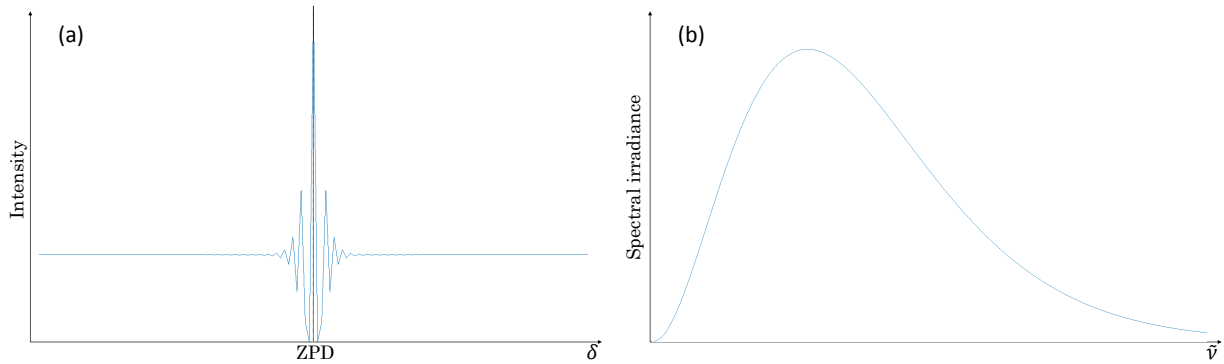

Figure 1.5: Interferogram of a blackbody source in panel (a) and its associated spectrum in panel (b).

1.3 Instrumental lineshape function

Section 1.2 introduced the working principle of a perfect instrument. The spectrum that was obtained was the true spectrum of the source. However, all physical instruments exhibit devia-

tions from this perfect apparatus, leading to the notion of instrumental lineshape function. The ILS is formally defined as the instrumental response to a monochromatic input signal [4, 9].

Two physical phenomena that have an influence on the instrumental lineshape function are the maximum path difference and the finite dimension of the source. They are respectively the topics of section 1.3.1 and section 1.3.2. In each of these two sections, a comprehensive and intuitive way to understand what happens is first presented. Then, a more formal approach is given.

1.3.1 Effect of maximum path difference

This section relies on references [7, 9].

The maximum path difference allowed by the spectrometer, denoted by $\delta_{\max}$, determines the maximum achievable spectral resolution $\Delta\tilde{\nu}$ of the spectrometer. The spectral resolution of the spectrometer measures its ability to distinguish two spectral peaks that are close to each other.

The relationship between $\delta_{\max}$ and $\Delta\tilde{\nu}$ is given by the following equation :

$$\Delta\tilde{\nu} = \frac{1}{\delta_{\max}}. \tag{1.26}$$

An intuitive way to illustrate it is to consider the beating between two monochromatic waves of slightly different frequencies $\tilde{\nu_1}$ and $\tilde{\nu_2}$ such that $\Delta\tilde{\nu} = \tilde{\nu_2} - \tilde{\nu_1}$. The interferogram, along with its spectrum, is depicted in Figure 1.6. It is necessary to measure a complete period of the beat pattern to distinguish the two frequencies that build the interferogram, imposing the optical path difference to be greater than $(\Delta\tilde{\nu})^{-1}$. The smaller the frequency interval between the two lines, the greater the retardation before the cosine waves become in phase again. The spectral resolution thus depends on the maximum optical path difference the interferometer can perform.

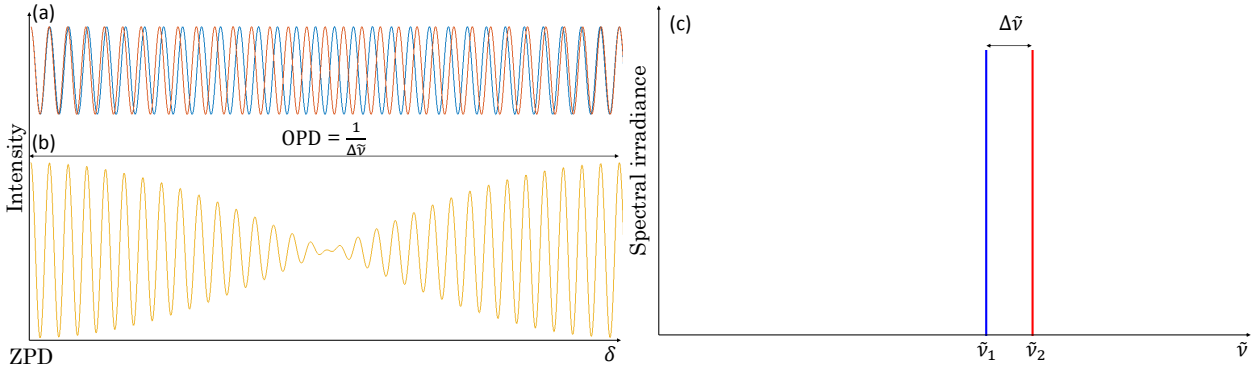

Figure 1.6: Interferogram of two monochromatic waves with slightly different wavenumbers. (a) Interferogram of each single monochromatic wave. (b) Interferogram resulting from the beating between the two monochromatic waves. (c) The spectrum consists of two lines of equal intensity.

The statement of equation (1.26) can be formally derived by multiplying the complete interferogram $I(\delta)$ (*i.e.* extending from $\delta = -\infty$ to $\delta = +\infty$) by a boxcar truncation function $D(\delta)$ that is equal to unity for $|\delta| < \delta_{\max}$, and zero otherwise :

$$D(\delta) = \begin{cases} 1 & \text{if } -\delta_{\max} \leq \delta \leq \delta_{\max} \\ 0 & \text{otherwise.} \end{cases} \tag{1.27}$$

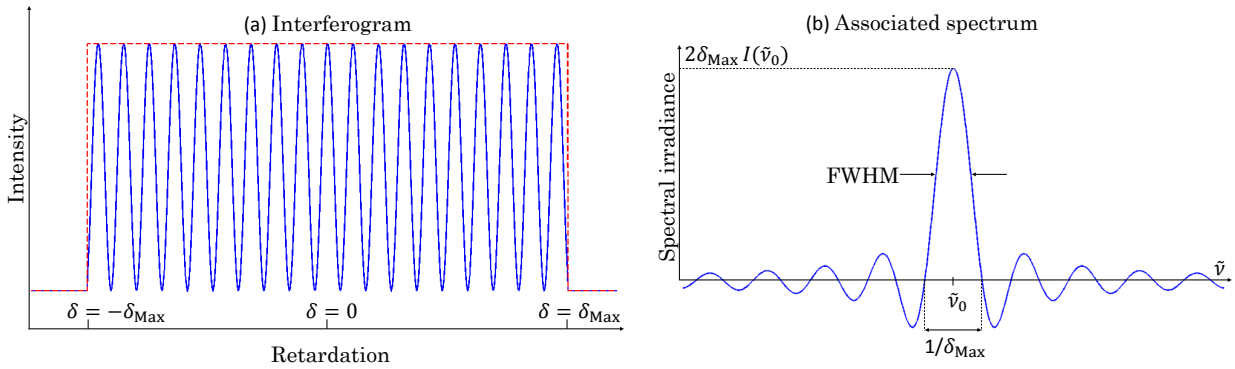

Figure 1.7: Influence of finite path length on a monochromatic source of wavenumber $\tilde{\nu_0}$. (a) The cosine signal is truncated at $\delta = \pm\delta_{\text{Max}}$. (b) The resulting spectrum consists in a sinc function centred in $\tilde{\nu} = \tilde{\nu}_0$. The width in between the two first zero-crossings of the sinc function is equal to $\frac{1}{\delta_{\text{Max}}}$.

The spectrum is then obtained by taking the Fourier transform of the product $I(\delta)D(\delta)$, that is by evaluating the following relationship :

$$B(\tilde{\nu}) = \int_{-\infty}^{+\infty} D(\delta)I(\delta)\mathrm{e}^{2\pi \mathrm{j}\tilde{\nu}\delta}\mathrm{d}\tilde{\nu}. \tag{1.28}$$

Since the Fourier transform of a product of two functions is equal to the convolution of the Fourier transforms of the two functions, the measured spectrum is equal to the true spectrum convolved by the Fourier transform of $D(\delta)$. The Fourier transform of a boxcar function of width $2\delta_{\text{max}}$ is the sinc function given by :

$$f(\tilde{\nu}) = 2\delta_{\text{max}} \frac{\sin\left(2\pi\tilde{\nu}\delta_{\text{max}}\right)}{2\pi\tilde{\nu}\delta_{\text{max}}} = 2\delta_{\text{max}}\text{sinc}\left(2\pi\tilde{\nu}\delta_{\text{max}}\right). \tag{1.29}$$

The interferogram of a truncated cosine and its associated spectrum are depicted in Figure 1.7. The sinc function is centred about $\tilde{\nu} = \tilde{\nu}_0$. The width of the first lobe is equal to $\frac{1}{\delta_{\text{Max}}}$. The full width at half maximum (FWHM) of the sinc function is known as the theoretical maximum resolution $R_{\text{theoretical}}$ achievable by the FTS and is given by :

$$\text{FWHM} = R_{\text{theoretical}} = \frac{1.207}{2\delta_{\text{Max}}}. \tag{1.30}$$

Figure 1.8 shows how the two lines of Figure 1.6 are modified by the measurement of the interferogram on a finite path difference. Each line is broadened by a sinc function with a width that depends on the maximum path difference. In Figure 1.8a, the maximum path difference is long enough to resolve both peaks while the translation stage is too short to clearly distinguish them in Figure 1.8b.

1.3.2 Effect of beam divergence

This section relies on references [2, 4, 7, 9].

Plane waves, all moving parallel to the optical axes, were considered in section 1.2, but light issuing from a finite aperture size is never perfectly collimated. Instead, it travels through the spectrometer on a range of off-axis angles that limit the achievable resolution of the spectrometer, as shown in Figure 1.9. The two extreme rays are traced. α_{max} denotes the maximum angle that can be accepted by the entrance aperture which is located at the focus of the collimating lens. A similar situation is encountered in sources of finite size, such as laser beams.

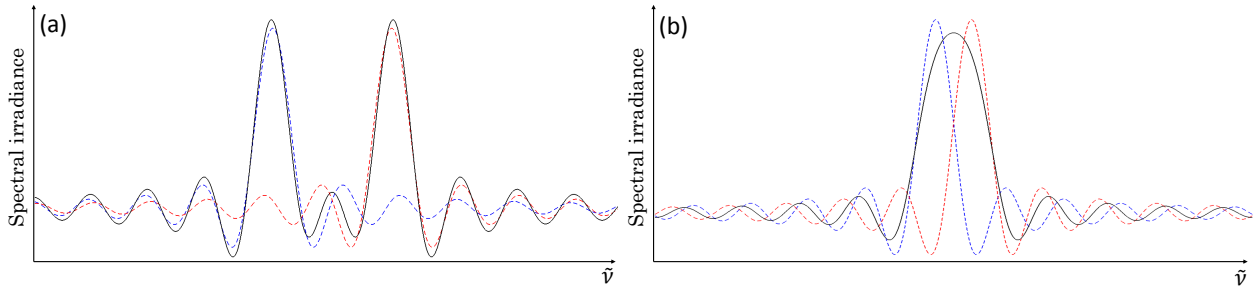

Figure 1.8: Spectra of two single lines of equal intensity modified by the finite length of the translation stage which is the same for both figures. The relative position of the two lines varies from one figure to another. (a) The maximum path difference is long enough to clearly distinguish the two peaks, i.e. $\Delta\tilde{\nu}$ is large enough. (b) The maximum path difference is too short to resolve the two peaks, i.e. $\Delta\tilde{\nu}$ is too small.

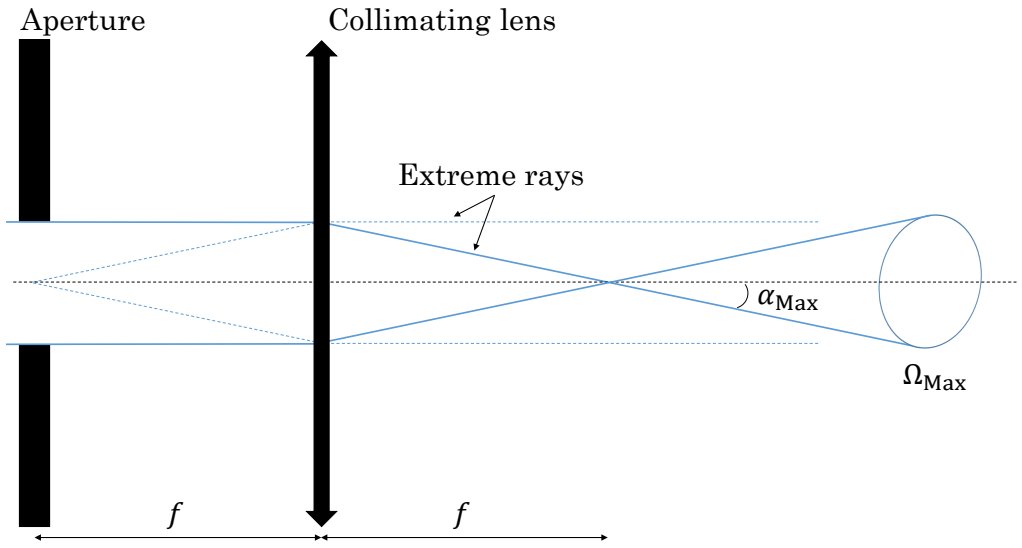

Figure 1.9: schematic of the interferometer entrance aperture. The aperture is located at the focus of the collimating lens. Extreme rays are traced in blue. This figure is inspired by Ref. [4].

In order to study the consequences of a source of finite size, it is convenient to consider a unique point source located at the focus of the collimating lens but aside from the optical axis of the instrument, as represented in Figure 1.10. Rays entering the spectrometer at a specific angle take different paths depending on the position of the moving mirror. The change in optical path difference can be evaluated by considering two interfering rays issued from the same wavefront. Figure 1.10 sketches the situation. On this figure, ray 1 interferes with the ray issued from the fixed arm (ray A) at ZPD while ray 2 interferes with this same ray A for a mechanical displacement l.

For a better insight of what is going on, it is convenient to look at Figure 1.11 which is a zoom of Figure 1.10 on the movable mirror. Both rays travel the same distance before reaching points B and C. However, ray 1 travels the supplementary distance BA compared to ray 2 whereas ray 2 travels the supplementary distances OA and CO with respect to ray 1, leading to an optical

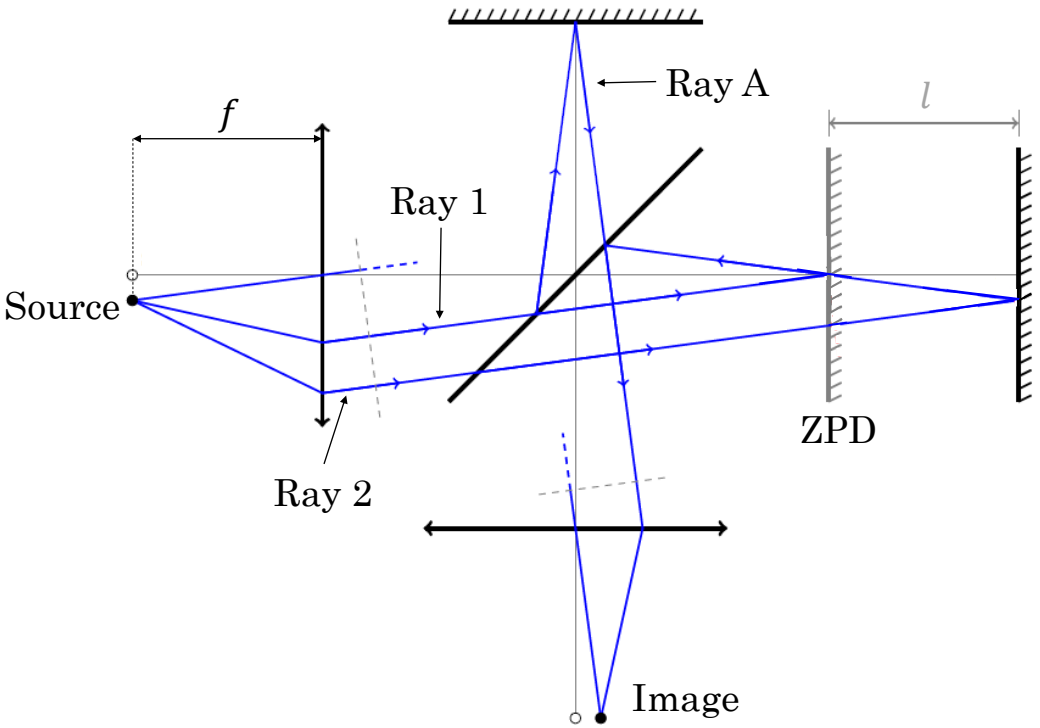

Figure 1.10: Ray tracing of a point source away from the centre of the optical axis and injected in a Michelson interferometer. The point source is in the focal plan of the collimating lens. The wavefront is represented by the dashed grey lines. This figure is adapted from Ref. [2].

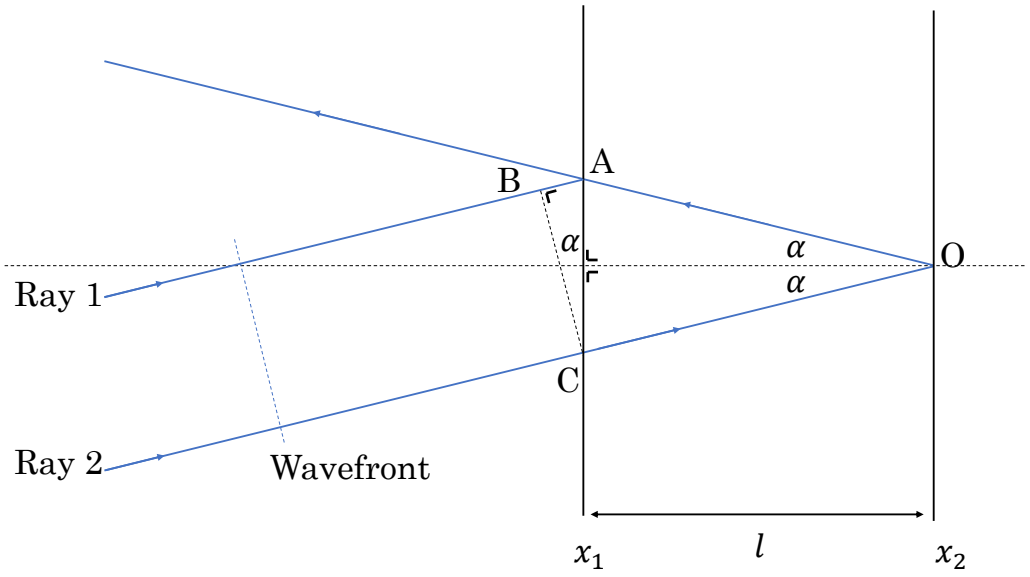

Figure 1.11: schematic of an off-axis ray striking the mobile mirror at different mirror displacements. This figure is adapted from Ref. [2].

path difference δ' between the two paths given by :

$$\delta' = OA + CO - BA. \tag{1.31}$$

Applying some geometry and trigonometry leads to :

$$\delta' = 2l\cos(\alpha) = \delta\cos(\alpha), \tag{1.32}$$

where δ is the on-axis optical path difference.

Optical path difference induced by a mechanical displacement l of the mirror is dependent on the divergence angle and equation (1.10) has to be modified to take into account off-axis rays :

$$I(\delta, \tilde{\nu}, \alpha) = B(\tilde{\nu}) \left(1 + \cos\left(2\pi\tilde{\nu}\delta\cos\left(\alpha\right)\right)\right). \tag{1.33}$$

Since α can take a continuum of values between zero and $\alpha_{\max}$, a same mechanical displacement leads to a set of apparent wavenumbers or measured wavenumbers, denoted $\tilde{\nu}_{\mathrm{m}}$, that depends on the off-axis angle :

$$\tilde{\nu}_{\mathrm{m}} = \tilde{\nu}\cos(\alpha). \tag{1.34}$$

It is necessary to consider all divergence angles for a single wavenumber. This is done by integrating over all the solid angles Ω that can be subtended by the entrance aperture (see Figure 1.9). This is done by integrating equation (1.33) with respect to Ω. A second integration over all the wavenumbers gives the measured intensity as a function of the on-axis optical path difference :

$$I(\delta) = \int_{-\infty}^{+\infty}\int_{0}^{\Omega_{\mathrm{Max}}} B(\tilde{\nu})\cos\left(2\pi\tilde{\nu}\delta\cos(\alpha)\right)\mathrm{d}\tilde{\nu}\mathrm{d}\Omega. \tag{1.35}$$

The divergence angle α is related to the solid angle Ω by the following definite integral :

$$\Omega = \int_{0}^{2\pi}\int_{0}^{\alpha'} \sin(\alpha')\mathrm{d}\alpha\mathrm{d}\phi = 2\pi\left(1 - \cos(\alpha)\right), \tag{1.36}$$

where ϕ is the azimuthal angle.

Substituting the $\cos(\alpha)$ of equation (1.35) by the expression of equation (1.36) leads to :

$$I(\delta) = \int_{-\infty}^{+\infty}\int_{0}^{\Omega_{\mathrm{Max}}} B(\tilde{\nu})\cos\left(2\pi\tilde{\nu}\delta\left(1 - \frac{\Omega}{2\pi}\right)\right)\mathrm{d}\tilde{\nu}\mathrm{d}\Omega. \tag{1.37}$$

This expression can be rewritten in a more convenient way by applying consecutively the three following trigonometric identities and by integrating with respect to Ω :

$$\cos(a-b) = \cos(a)\cos(b) + \sin(a)\sin(b), \tag{1.38}$$

$$\sin(a-b) = \sin(a)\cos(b) - \cos(a)\sin(b), \tag{1.39}$$

$$\sin(a) + \sin(b) = 2\sin\left(\frac{a+b}{2}\right)\cos\left(\frac{a-b}{2}\right), \tag{1.40}$$

giving :

$$I(\delta) = \Omega_{\mathrm{Max}}\int_{-\infty}^{+\infty} B(\tilde{\nu})\mathrm{sinc}\left(\frac{\tilde{\nu}\delta\Omega_{\mathrm{Max}}}{2}\right)\cos\left(2\pi\tilde{\nu}\delta\left(1 - \frac{\Omega_{\mathrm{Max}}}{4\pi}\right)\right)\mathrm{d}\tilde{\nu}. \tag{1.41}$$

Figure 1.12 consists of a plot of equation (1.41) for a monochromatic source with three different maximum divergence angles. For each wavenumber, the interferogram consists of a cosine of wavenumber $\frac{\tilde{\nu}(1+\cos(\alpha_{\mathrm{Max}}))}{2}$ multiplied by a sinc function vanishing for the first time for an optical path difference equal to $\pm\frac{1}{\tilde{\nu}(1-\cos(\alpha_{\mathrm{Max}}))}$. A large entrance aperture leads to a more rapid decrease in contrast as the optical path difference increases. This phenomenon is named self-apodization. It should be pointed out that the interferogram, given by equation (1.41), is also multiplied by Ω_{Max}, meaning that increasing the throughput at the entrance aperture increases the signal at the photodetector. Since the sinc function depends on the wavenumber, the sinc will first vanish for important wavenumbers leading to a decrease in signal. Opening of the entrance aperture represents a trade-off between optical throughput and the spectral resolution that must be achieved.

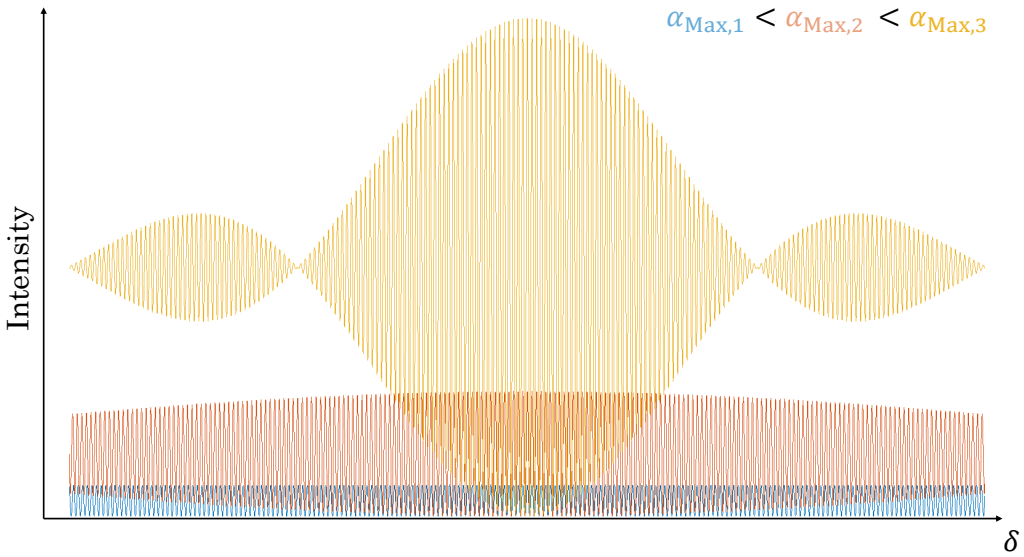

Figure 1.12: Interferogram of a coherent monochromatic source for three maximum divergence angles.

In order to obtain the instrumental lineshape function, a monochromatic source of wavenumber $\tilde{\nu}_0$ is considered. Equation (1.41) simply becomes :

$$I(\delta) = \Omega_{\text{Max}} B(\tilde{\nu}_0) \text{sinc}\left(\frac{\tilde{\nu}_0 \delta \Omega_{\text{Max}}}{2}\right) \cos\left(2\pi\tilde{\nu}_0\delta\left(1 - \frac{\Omega_{\text{Max}}}{4\pi}\right)\right). \tag{1.42}$$

The product between the cosine function (interferogram) and the sinc function gives rise to a convolution in the spectral domain. The spectrum is then given by :

$$I(\tilde{\nu}) = \begin{cases} \frac{B(\tilde{\nu}_0)\Omega_{\text{Max}}}{\tilde{\nu}_0(1-cos\alpha_{\text{Max}})} & \text{if } \tilde{\nu}_0 \cos(\alpha_{\text{Max}}) \leq \tilde{\nu} \leq \tilde{\nu}_0 \\ 0 & \text{otherwise.} \end{cases} \tag{1.43}$$

It is a boxcar function centred in $\frac{\tilde{\nu}(1+\cos(\alpha_{\text{Max}}))}{2}$, with a width equal to $\tilde{\nu}_0(1-\cos(\alpha_{\text{Max}}))$. It should be emphasized that the width of the boxcar depends on the wavenumber,

Another phenomenon resulting from beam divergence is the spatial interference pattern observable in the image field of view if a monochromatic source is injected in the interferometer. It is the so-called Haidinger fringe pattern that is represented in Figure 1.13a. A lens is used to condense light at the photodetector. Light propagating at an angle α is brought into focus at a distance $r = f\sin(\alpha)$ from the optical axis, with f the focal length. The situation is shown in Figure 1.13b. Interference between rays that propagate at a given angle in the two arms will occur since they are spatially overlapped in the image plane. There is no azimuthal dependence in the optical path difference, leading to a pattern that consists of concentric circular disks of equal inclination. The distance between the bright fringes is a function of the optical path difference and of the wavenumber.

The simultaneous detection of several disks leads to a decrease in contrast of the interference pattern. If all the disks were measured with a single photodetector, there would be no overall change of intensity with respect to the retardation. The dimension of the entrance aperture is chosen so that only the central filled disk can be formed [7].

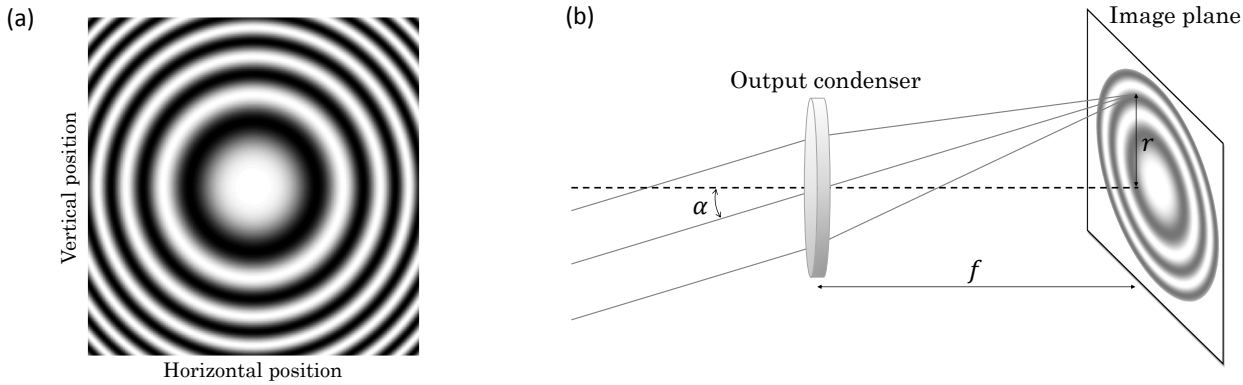

Figure 1.13: Haidinger Fringe pattern. Rays with a same inclination angle are mapped at a same distance r from the optical axis.(a) Pattern in the image plane. (b) Action of a lens on rays of equal inclination.

1.4 Sampling

Interferograms are continuous functions of the retardation, but digitally convert them imposes their discretization. In practice, the interferogram can be either sampled at uniform OPD or at uniform time intervals. However, the final interferogram should be sampled on a constant OPD sampling grid to recover the spectrum (see equation (1.21)). Both sampling methods imply the use of a spatial reference which usually consists in a helium-neon (He:Ne) laser. Its role is detailed in section 1.4.1.

For the discrete signal to be mathematically equivalent to the continuous interferogram, requirements on the sampling frequency must be satisfied. These requirements are described in section 1.4.2.

1.4.1 Reference Laser

This section relies on references [5, 7].

The spectrum is retrieved from the interferogram by applying a Fourier transform. This operation implies that the interferogram was first sampled at uniform OPD spacing. Therefore, it is mandatory to have a spatial reference to generate the constant OPD sampling grid. Continuous wave (cw) lasers usually serve this purpose in a Fourier transform spectrometer. Indeed, injecting a quasi-monochromatic light in a Michelson interferometer leads to a cosine signal when varying the OPD. The period of this cosine signal is equal to the wavelength of the laser and can be used as a spatial reference. The sampling process is shown in Figure 1.14.

He:Ne lasers are typically used as reference lasers in Fourier transform spectrometers. Sampling the interferogram can be performed in two different ways using the He:Ne laser. The first method consists in detecting the zero crossings with an analog circuit which then triggers the analog-to-digital converter (ADC). The second method makes use of an ADC with two channels that are simultaneously triggered by an external stable clock. One of the channels records the interferogram of interest while the other records the He:Ne interferogram. The sampling at constant OPD of the interferogram is done at the software level with the help of the reference laser signal.

The sampling grid obtained with the reference laser also permits to add several interferograms in order to improve the signal-to-noise ratio (SNR).

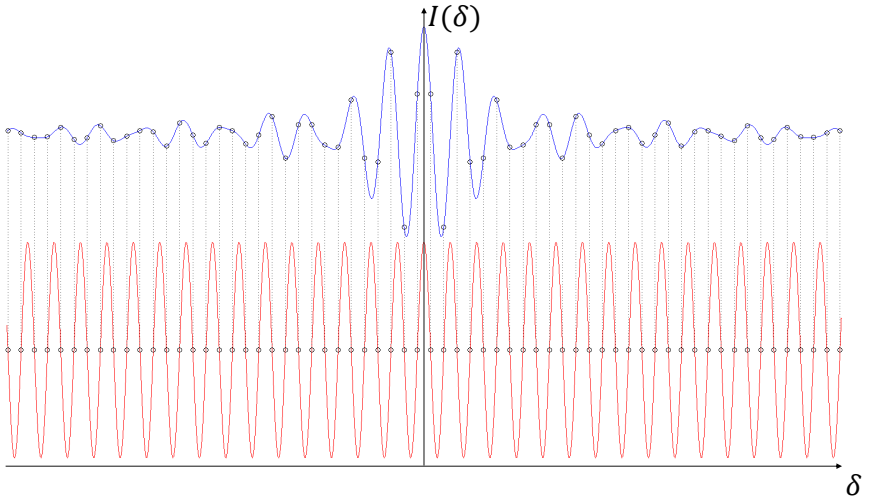

Figure 1.14: The interferogram is sampled at each zero-crossing of the He:Ne reference laser (black bullets). The red curve corresponds to the interferogram of the He:Ne reference laser and the blue curve to the interferogram of the light source.

1.4.2 Sampling frequency and aliasing

This section relies on reference [12].

Sampling the continuous interferogram implies to take measurements at some specific moments. This operation is mandatory to numerically represent and manipulate the signal. However, one has to be careful when determining the sampling frequency to avoid spectrum distortion due to aliasing. This section describes the origin of aliasing for a continuous signal $x(t)$ uniformly sampled at time intervals T_s.

The sampled function $x_s(t)$ can be mathematically expressed as the product of the original continuous function $x(t)$ with an impulse train, that is a comb of impulse functions uniformly spaced by the sampling period T_s.

$$x_s(t) = x(t) \cdot \sum_{n=-\infty}^{\infty} \delta(t - nT_s). \tag{1.44}$$

In this equation, $\delta(t)$ corresponds to the impulse function which is defined as follows :

$$\delta(t) = \begin{cases} 1 & \text{if } t = 0 \\ 0 & \text{if } t \neq 0. \end{cases} \tag{1.45}$$

The sampled function thus only takes non-zero values at times $t = nT_s$, where n is an integer. Figure 1.15a depicts the situation for the continuous function $x(t) = \text{sinc}^2(t)$. Its Fourier transform, denoted by $X(f)$, is the triangular function which is shown in Figure 1.15b. The bandwidth of the spectrum extends from $-f_{\text{Max}}$ to f_{Max}.

The Fourier transform of a product of two functions is equal to the convolution[1] of the Fourier transforms of each function. The Fourier transform of equation (1.44) is thus given by the convolution of the spectrum of $x(t)$ with the Fourier transform of the impulse train. The Fourier transform of a comb of impulse functions, each spaced by an interval T_s is another comb with each impulse separated by a value $f_s = \frac{1}{T_s}$ and scaled by a factor $\frac{1}{T_s}$. The spectrum of the

[1]The convolution product is written $\circledast$

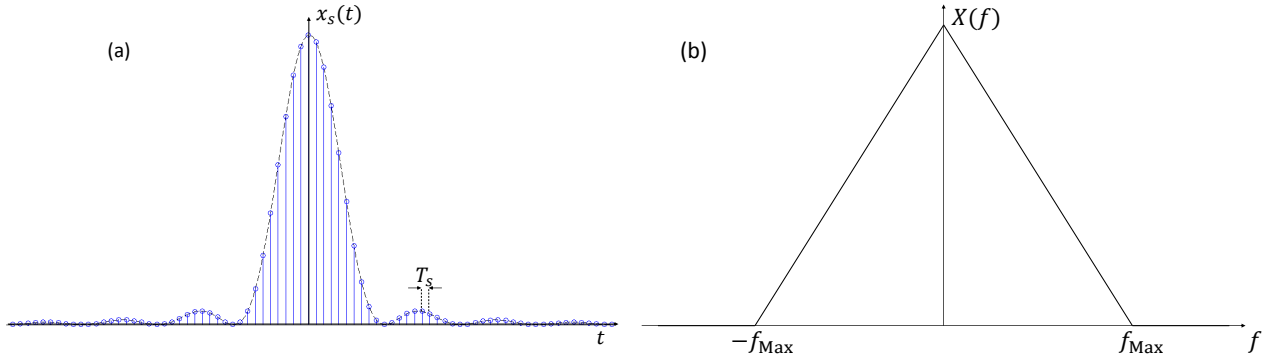

Figure 1.15: (a) Sampled squared sinc function. The black dashed curve corresponds to the continuous function. The comb of delta functions is represented by blue lines ended by a circle. (b) Fourier transform of the continuous squared sinc function.

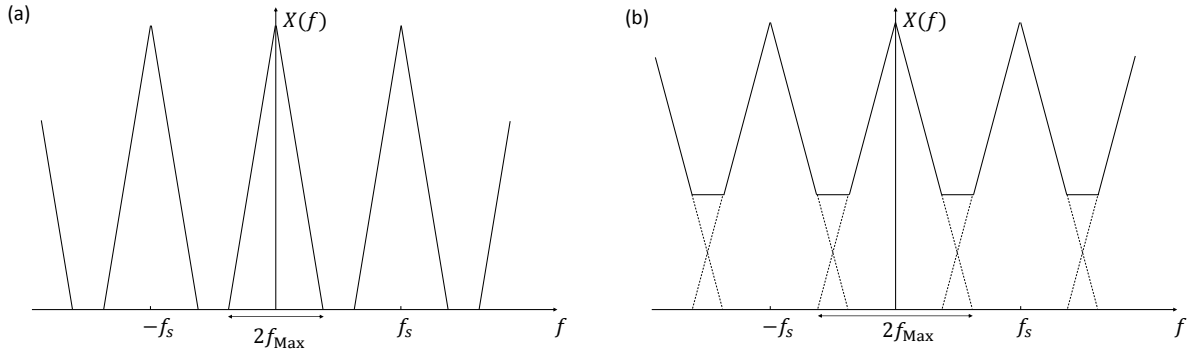

Figure 1.16: Fourier transform of a sampled squared sinc function. (a) The sampling theorem is satisfied : the spectrum is not distorted. (b) The sampling theorem is not satisfied : aliasing occurs, leading to spectrum distortion.

sampled signal of equation (1.44) is therefore given by :

$$X_s(f) = X(f) \circledast \frac{1}{T_s} \sum_{k=-\infty}^{\infty} \delta(f - kf_s). \tag{1.46}$$

A function convoluted with an impulse function remains unchanged. Thus, a function convoluted with a comb of impulse functions simply repeats itself with a spacing f_s between two consecutive repetitions :

$$X_s(f) = \frac{1}{T_s} \sum_{k=-\infty}^{\infty} X(f - kf_s). \tag{1.47}$$

These repetitions will overlap if the sampling frequency is not large enough compared to the frequency extend of the sampled signal. This phenomenon is called aliasing and it causes a distortion of the signal. Figure 1.16 represents the Fourier transform of the sampled sinc^2 of Figure 1.15a for two distinct sampling frequencies. On the left figure, the sampling frequency is high enough to avoid signal distortion. On the right figure, the sampling frequency is too low for the signal. Consecutive replicas of the spectrum add together, modifying its shape. Thus, the spectrum of the sampled signal cannot be employed to analyze the original continuous-time signal.

In order to prevent aliasing, the sampling frequency f_s must be equal to or greater than twice the maximum frequency component f_{Max} of the signal that has to be sampled :

$$f_{\text{Max}} \leq \frac{1}{2} f_s. \tag{1.48}$$

In a Fourier transform spectrometer, different methods are employed to avoid aliasing. One way is to use optical filters as low-pass filters. It allows a control on the shortest wavelength that can reaches the photodetector. Another way relies on anti-aliasing low-pass electronic filters. The second category has the advantage to suppress high-frequency noise as well [4, 7].

Conclusion

Fourier transform spectrometers are instruments that entirely rely on a simple and elegant mathematical idea : the Fourier transform [4]. However, they are also complex instruments that are at the intersection of many disciplines. A good knowledge in all of these disciplines is necessary to understand the physical limitations of FTS (maximum OPD and beam divergence), but also the many advantages they encompass compared to the other technologies that are available to perform irradiance spectrum measurements. Sections 1.1 and 1.2 were dedicated to the working principle of a perfect instrument while sections 1.3 and 1.4 expose some issues of all modern FTS.

Section 1.1 was dedicated to Michelson interferometers which lie at the heart of Fourier transform spectrometers. In practice, other optical configurations than the original Michelson interferometer do exist, but they somehow all rely on the same principle : an incoming beam is divided into two parts that travel different distances before being recombined. This permits to induce an optical path difference that will modulate the intensity at the output. This modulation allows to downscale optical frequencies in the audio range, making their measurement possible with the available technologies [4].

Section 1.2 showed that the measured interferogram and the spectral irradiance spectrum are related by a Fourier transform. The benefits of recording both outputs of an FTS were emphasized.

The notion of instrumental lineshape function was introduced in section 1.3. These functions express the relationship between the true spectrum of the source and the one measured by the instrument. Moreover, it was shown that maximum path difference and beam divergence, both inherent to any FTS, have unavoidable consequences on the resolution.

Finally, the consequences of sampling the interferogram were mentioned in section 1.4. The use of a quasi-monochromatic laser as a spatial reference was first outlined. Then, constraints on the sampling frequency were made explicit.

Chapter 2

Setup

This chapter aims at introducing some of the elements of the spectrometer and the way they are arranged together to form the instrument. Experiments that were performed to study the behaviour of these elements are detailed. Some aspects of the instrument design are presented as well.

Section 2.1 introduces the optical design of our FTS. The configuration of the optics on the optical bench is first presented. The use of retro-reflectors instead of mirrors is justified. Influence of the beam divergence on the resolution of the FTS is detailed, along with the methodology adopted to select the beam expanders that are used to counteract the beam divergence.

Section 2.2 concerns the characterization of the He:Ne laser stabilization.

2.1 Optical design

The goal of this section is to present the optical aspects of the instrument, that is the optical configuration, the choice of some of the optics and consequences of beam divergence. They are discussed in three distinct subsections.

Section 2.1.1 is a general description of the setup. Configuration of the optics on the optical bench is detailed.

Section 2.1.2 aims at justifying the use of retro-reflectors instead of mirrors for the movable parts of the interferometer.

Finally, section 2.1.3 concerns the divergence of the beams and their influence on both the visibility of the interference fringes and on the resolution of the FTS.

2.1.1 Configuration

The Fourier transform spectrometer is an instrument that depends on a two-beam interferometer to downconvert light frequencies in the audio frequency range. In its simplest form, the two-beam interferometer is the Michelson interferometer which was introduced in section 1.1 but more complex optical configurations are usually preferred. Indeed, these configurations allow reducing the sensitivity of the setup to the tilt or shear of the optics [9], but they also permit to measure both the balanced and unbalanced outputs of the interferometer and to increase its opto-mechanical gain, that is the optical path difference generated by a given mechanical displacement of the movable optics.

A schematic of the optical bench is depicted in Figure 2.1 while a photograph is shown in Figure 2.2. Path followed by the He:Ne laser beam is traced in red and path followed by the source beam is traced in blue. The green lines represent the places where both beams are spatially overlapped. Choice was made to overlap the two beams in the interferometer for two reasons. Firstly, if interference fringes are observed for the He:Ne laser, then interference should be observed as well for the light source under study. Secondly, the retro-reflectors that are used are corner cubes and there are great chances that one of the beams hits an edge of the corner cube if they are not overlapped in the interferometer, resulting in a deterioration of the beam profile. Overlap of the two beams in the interferometer at the input of the spectrometer and separation at its output were performed with the help of dichroic mirrors. Dichroic mirrors allow to spatially separate light beams of different frequencies by transmitting or reflecting light depending on its frequency. Description of the paths followed by the He:Ne laser and the light source are the topics of the next two paragraphs.

The beam of the stabilized He:Ne laser is expanded by the beam expander BE1 (model GBE05-A of Thorlabs) and it is injected parallel to the translation stage in the interferometer thanks to the injection mirrors IM1. The S-polarization of the He:Ne laser is rejected with the help of the CCM1-PBS25-633/M polarizing beamsplitter (PBS) of Thorlabs (see Figure A.6 for the transmission and reflection coefficients of the PBS with respect to the wavelength.). The dichroic mirror DM1 is transparent for the He:Ne laser and the beam is thus transmitted through it (unknown model). The beam is then split in two parts at the VIS/Q IT501/2 beamsplitter BS of Bruker. Part of the light is reflected by the beamsplitter and it travels in the arm containing the three mirrors M1, M2 and M3 before being reflected back by a PS976M retro-reflector placed in the carriage. The other part is transmitted by the beamsplitter and travels in the arm containing the two mirrors M4 and M5 before being reflected by the second PS976M retro-reflector. The two beams are then recombined at the beamsplitter. Part of the recombined beam reaches the dichroic mirror DM2 that reflects the He:Ne beam in the direction of the optical filter OF1 which is a very narrow bandpass filter centred on the wavelength of the He:Ne laser. The dichroic mirror DM2 is the DLMP650 dichroic mirror of Thorlabs. Reflectance and transmittance of the dichroic mirror with respect to the wavelength are shown in Figure A.4. The cutoff wavelength of this dichroic filter is equal to 650 nm, meaning that no measurement at wavelengths smaller to 650 nm can be performed for the moment. The beam is then focused on the PDA36A-EC photodetector (PD1) of Thorlabs with the help of a lens (L1). The responsivity of the PDA36A-EC photodetector is shown in Figure A.8.

The light source used in the FTS is a Fianium SC450-4 supercontinuum source. Its power spectral density is depicted in Figure A.9. Advantages of a supercontinuum laser compared to more traditional thermal sources are its high brightness and the fact it is already collimated. The laser beam at the output of the supercontinuum first passes through a FELH0700 optical filter manufactured by Thorlabs (transmission with respect to the wavelength of the FELH0700 optical filter (OF2) is shown in Figure A.3). The role of this optical filter is to reduce the spectral range of the supercontinuum in order to avoid aliasing. The laser beam is then expanded by the beam expander BE2 (model GBE03-B of Thorlabs). The injection mirrors IM2 and the mirror M6 permit to inject the supercontinuum laser in the interferometer. The dashed orange frame in Figure 2.1 indicates the position of the gas sample under study in the setup. The dichroic mirror DM1 is reflective for the supercontinuum laser, and the path followed by the supercontinuum laser beam is now the same as the one followed by the He:Ne laser in the interferometer. They are separated by the dichroic mirror DM2 just before the detection optics. The dichroic mirror is transparent for the wavelength range of the supercontinuum. The lens L2, placed behind the dichroic mirror, is used to focus the beam on the PDA36A-EC photodetector PD2. For the moment, the unbalanced output of the spectrometer remains unexploited, but it would be interesting to record both outputs in a future prototype of FTS (cf. section 1.2).

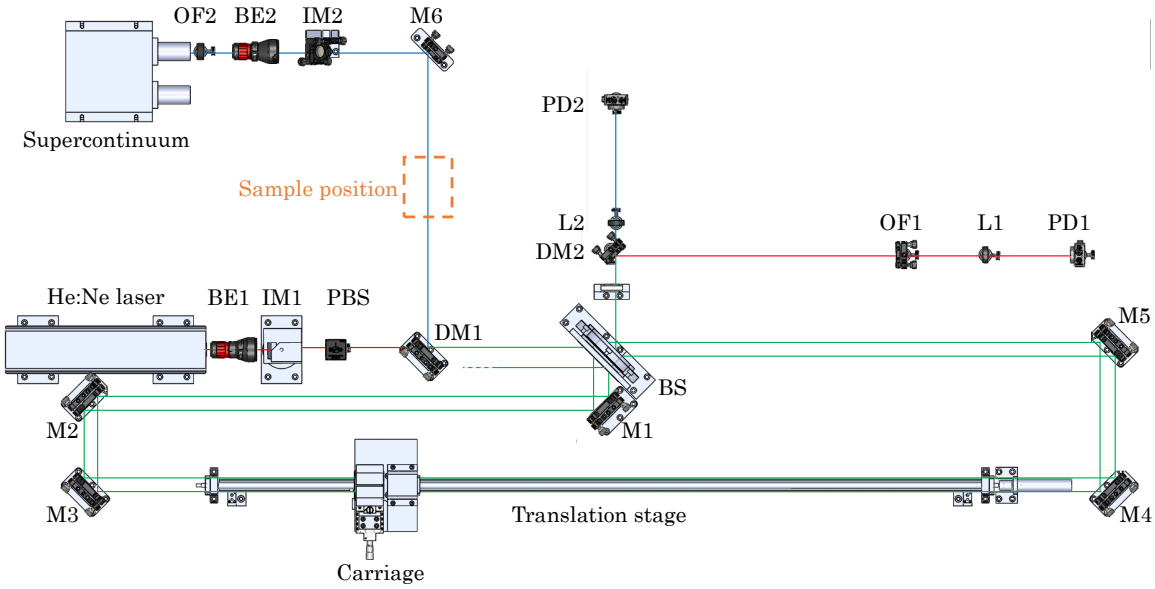

Figure 2.1: Schematic of the optical bench. BE stands for beam expander, BS for beamsplitter, CC for corner cube, D for diaphragm, DM for dichroic mirror, IM for injection mirrors, L for lens, M for mirror, OF for optical filter, PBS for polarized beamsplitter and PD for photodetector. The blue beam represents the supercontinuum beam, the red beam is the He:Ne laser beam and the green beam depicts the overlapping of the two beams. The assembly was performed on SOLIDWORKS by Daniel Dedouaire.

The role of the two beam expanders is to diminish consequences of the intrinsic divergence of the laser beams on the contrast of the interference fringes and on the resolution of the FTS. The way they accomplish this task is detailed in section 2.1.3, along with the methodology adopted to select their expansion coefficient. All the mirrors of the setup are silver-coated mirrors. These mirrors were chosen because they offer the highest reflectance in the visible and near-visible ranges [13]. The reflectance of the silver coated mirrors with respect to the wavelength is shown in Figure A.1. The average reflectance is superior to 97.5% in the 250 nm $-$ 2μm range. The two PS976M retro-reflectors are made of N-BK7 glass. The transmission coefficient of N-BK7 with respect to the wavelength is shown in Figure A.2.

The two retro-reflectors are placed on the carriage which is guided by a dovetail slide and driven by a ball screw and a threaded shaft. The carriage displacement allows inducing an optical path difference by varying the optical path length of the two arms. The translation stage is 1.5 meters long but its work run is about 1.35 meters long. The advantage of placing the two retro-reflectors on the carriage is that the optical path difference varies by a factor 4 with respect to the mechanical displacement of the carriage. In other words, the mechanical gain is equal to 4. The optical contact is approximately located at halfway of the translation stage, meaning that double-sided interferograms are recorded. The maximum OPD that can be induced by the translation stage is equal to 2.7 meters, leading to a resolution of $3.7 \cdot 10^{-3}$ cm^{-1}. Advantages and drawbacks of using reflectors instead of mirrors are given in section 2.1.2.

The alignment procedure of the FTS is described in appendix B. The optical configuration is the one suggested by Cossel [14].

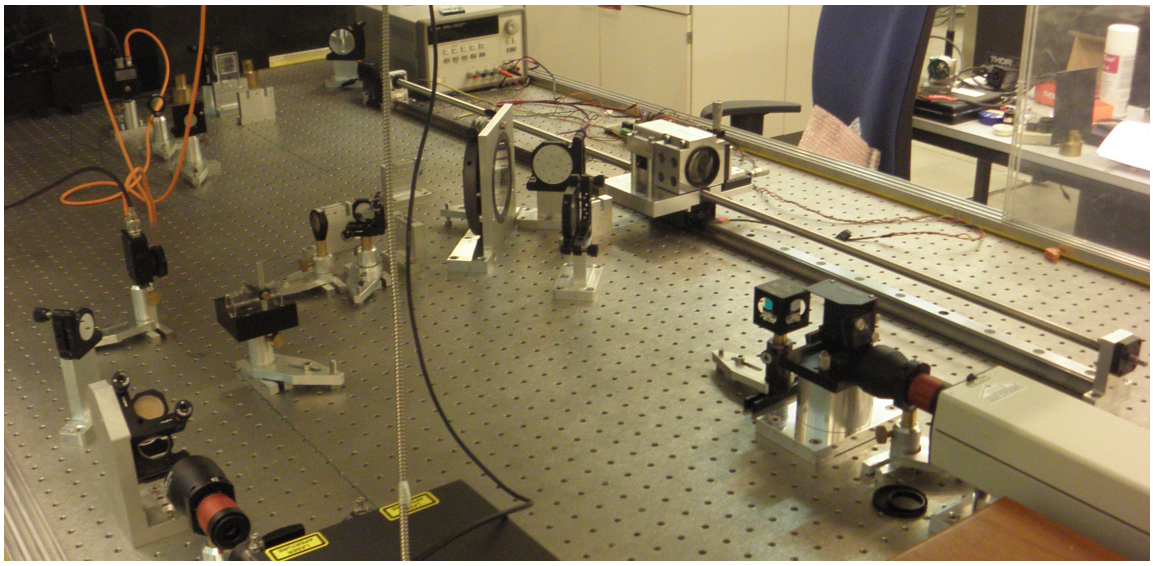

Figure 2.2: Photograph of the setup.

2.1.2 Retro-reflectors

In a Michelson interferometer, light must be reflected back to the beamsplitter after having travelled a certain distance in the two arms. When mirrors are used to fulfil this task, any misalignment can result in a loss of signal. Indeed, any mirror tilt induces optical path difference that varies with the lateral position of the beam. Since the whole beam is measured at once, a range of optical path differences due to the mirror tilt is measured simultaneously. Therefore, integration of the fringe pattern due to the collimating optics results in a loss of fringe visibility and ultimately in a loss of signal. Even mirror tilts of a few micro-radians can produce notable effects on the interferogram [9]. Influence of the mirror tilt on the interferogram is deeply studied in references [5, 7, 9].

There are two common methods to overcome problems resulting from mirror tilts : either a dynamic alignment technique is employed or the mirrors are replaced by retro-reflectors. In dynamic alignment techniques, the reference beam of the He:Ne laser is split into three parts that are modulated in the interferometer and that are then detected by three distinct photodetectors. In the absence of tilt, the three beams travel the same distance and are in phase. Any difference in the phase arises from mirror tilting. Actuators allow counteracting the mirror tilting in real time. Such a method is only possible when the measured interferogram lies in the infrared. Indeed, the short wavelength of the He:Ne laser compared to the infrared range allows correcting the tilt before the infrared signal is significantly impacted by the tilt [7]. Since we are interested in obtaining interferograms in the visible range too and because of the complexity of such a feedback system, dynamic alignment was not considered at all in the design of the FTS.

As already mentioned, another method to overcome problems arising from tilt misalignments consists in the use of retro-reflectors instead of mirrors. Retro-reflectors are optical assemblies that reflect light parallel to the incoming beam, whatever the incident angle. The retro-reflectors that are used in our setup are the so-called corner cube retro-reflectors. Such optical assemblies are not sensitive to tilt. However, they are sensitive to lateral displacements. If one of the two retro-reflectors is laterally shifted with respect to the ideal positioning imposed by both the other retro-reflector and the beamsplitter, the output beams may no longer be perfectly superimposed spatially at the image field of view (FOV) [9]. Consequence of the lateral displacement on a reflected ray is illustrated in Figure 2.3b while Figure 2.3a gives a good insight of the behaviour of the corner cube when it is tilted.

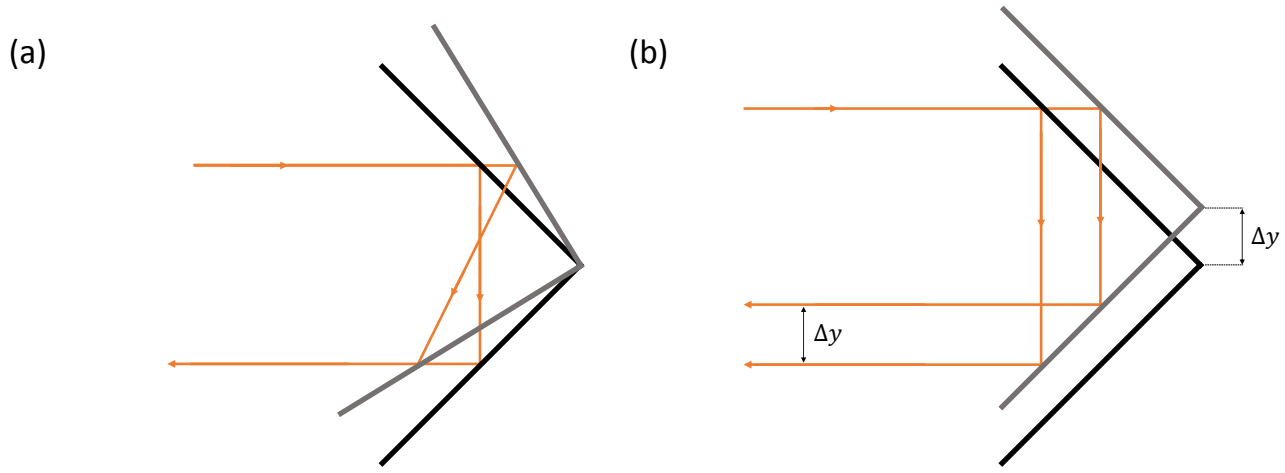

Figure 2.3: Response of a retro-reflector to (a) tilt and to (b) lateral displacement.

The ability to adjust the lateral positioning of one corner cube with respect to the other is mandatory. The first prototype of the carriage did not allow this fine adjustment, making impossible to correctly align the interferometer on the complete course of the carriage. Figure 2.4 illustrates the sensitivity of a lateral misalignment. To obtain Figure 2.4a, the interferometer was first aligned following the first four steps of the procedure described in appendix B. The beam hits the apex of the two corner cubes and it is reflected back on itself everywhere in the interferometer. Two photographs of the interferometer image FOV were then taken without modifying the camera FOV. For each photograph, a different arm was obstructed. The colour of one of these two photographs was then modified and they were finally superimposed to form a single picture. In the case of Figure 2.4b, the fifth step of the alignment procedure described in appendix B was performed as well, and the laser beam now hits one of the two top quadrants and it leaves the corner cube from one of its two bottom quadrants. The spatial overlap issuing from the two arms seems to correctly overlap spatially in Figure 2.4a. The star-like pattern is caused by the fact that the beam hits the apex of the corner cubes. Even if one of these two star-like patterns has undergone a rotation with respect to the other, they are still centred. This good spatial overlap is maintained on the complete course of the carriage, certifying the correct alignment of the interferometer. On the other hand, the spatial overlap is poor in Figure 2.4b. This poor overlap is imputed to a bad lateral positioning of one corner cube with respect to the other that is emphasized when injecting the light elsewhere than on the apex of the two corner cubes.

Retro-reflectors that are used in our setup are the PS976M uncoated corner cubes of Thorlabs. The use of these retro-reflectors permits to get rid of tilting problems. However, they suffer from two drawbacks : they induce extra-losses compared to the silver mirrors that are used everywhere else in the setup but they also modify the polarization of the light. Comparison between losses in silver mirrors and losses in corner cubes is performed in Figure 2.6 while Figure 2.5 depicts the change in polarization induced by the retro-reflectors for two linearly polarized beams with orthogonal polarizations. No matter its initial polarization direction, a linearly polarized light becomes elliptically polarized after being reflected by the corner cubes, leading to a reduction in the fringe visibility since orthogonal polarizations do not interact with one another. One way to overcome this problem relies on the use of a linear polarizer placed just before the detection optics. The linear polarizer will project the polarization along its polarization axis, resulting in a gain of contrast. In order to demonstrate there is in fact a gain of contrast when using a linear polarizer, the He:Ne laser was first linearly polarized using a PBS before being injected in the spectrometer, and the fringe visibility was evaluated by taking a record of the He:Ne signal at the output of the interferometer for different polarization angles of the output linear

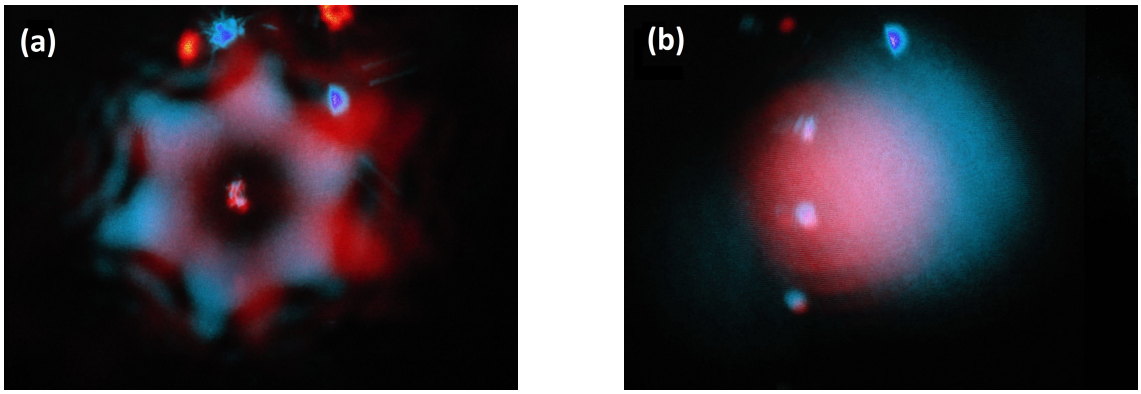

Figure 2.4: Spatial overlap between the He:Ne laser beams issuing from the two arms of the Michelson interferometer at the image FOV. (a) The beam is reflected on the apex of the corner cubes; the spatial overlap is good. (b) The beam hits one of the two quadrants at the top of the corner cube; the spatial overlap is poor.

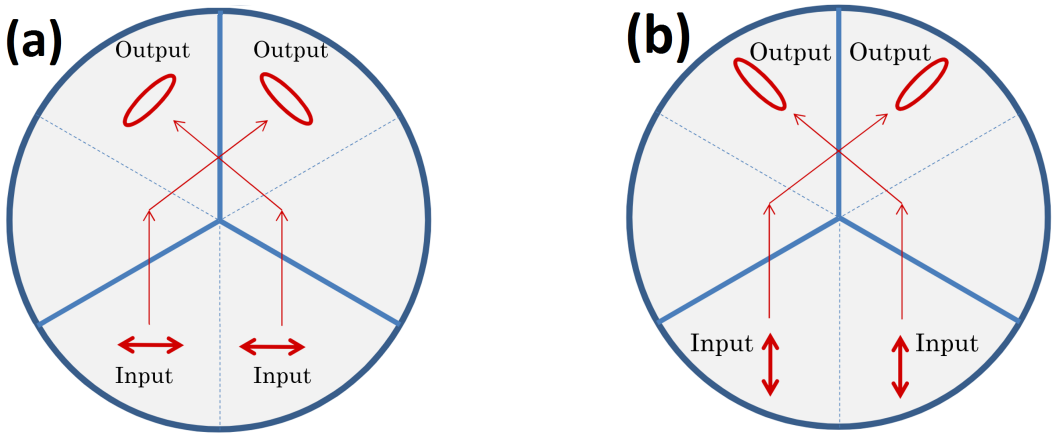

Figure 2.5: Change in polarization induced by the cube corners. (a) Horizontal polarization. (b) Vertical polarization. From Ref. [15].

polarizer. For each measurement, the carriage traveled a small distance on both sides of the optical contact, leading to a sinusoidal signal of a few thousands periods. All the minimum and maximum values $I_{\min}$ and $I_{\max}$ of this signal were then determined and the mean fringe visibility was finally evaluated thanks to the following expression [8] :

$$\text{Visibility} = \frac{I_{\max} - I_{\min}}{I_{\max} + I_{\min}}. \tag{2.1}$$

Variation of the fringe visibility with respect to the polarization angle of the linear polarizer placed just before the detection optics is depicted in Figure 2.7. The horizontal axis is only relative and coincides with the graduations written on the rotation mount that holds the linear polarizer. The continuous black horizontal line corresponds to the case where there is no linear polarizer placed before the detection optics. For a series of polarization angles, contrast is greater than in the absence of polarizer while for the other polarization angles, there is a reduction in contrast compared to the situation where no polarizer is used at the output of the interferometer. The gain in contrast is imputed to the situation where the linear polarizer is directed along the major axis of the elliptical polarization of the retro-reflected light while a loss in contrast occurs when the polarizer is orientated along the minor axis of the elliptical polarization.

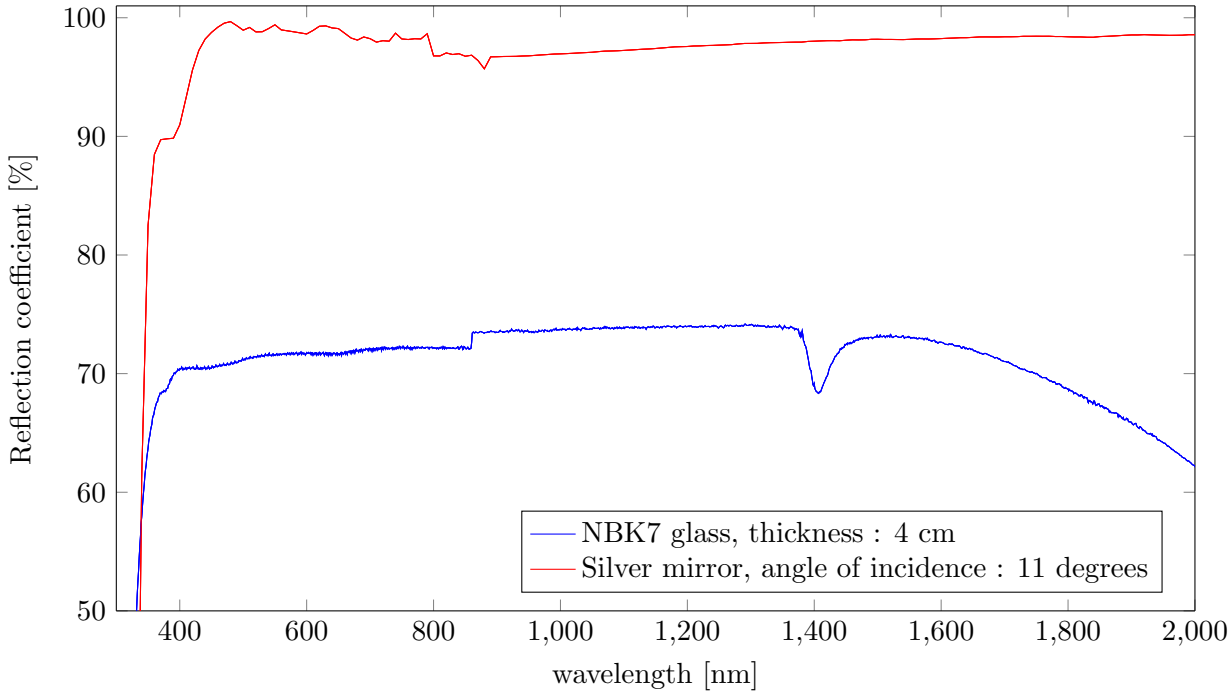

Figure 2.6: Comparison between the reflection coefficient of a silver mirror and the effective reflection coefficient of a NKB-7 glass corner cube. The effective reflection coefficient of the corner cube was estimated using the transmission coefficient of the NKB-7 glass and by considering that light travels 4 cm in the material. The data are available on the THORLABS website.

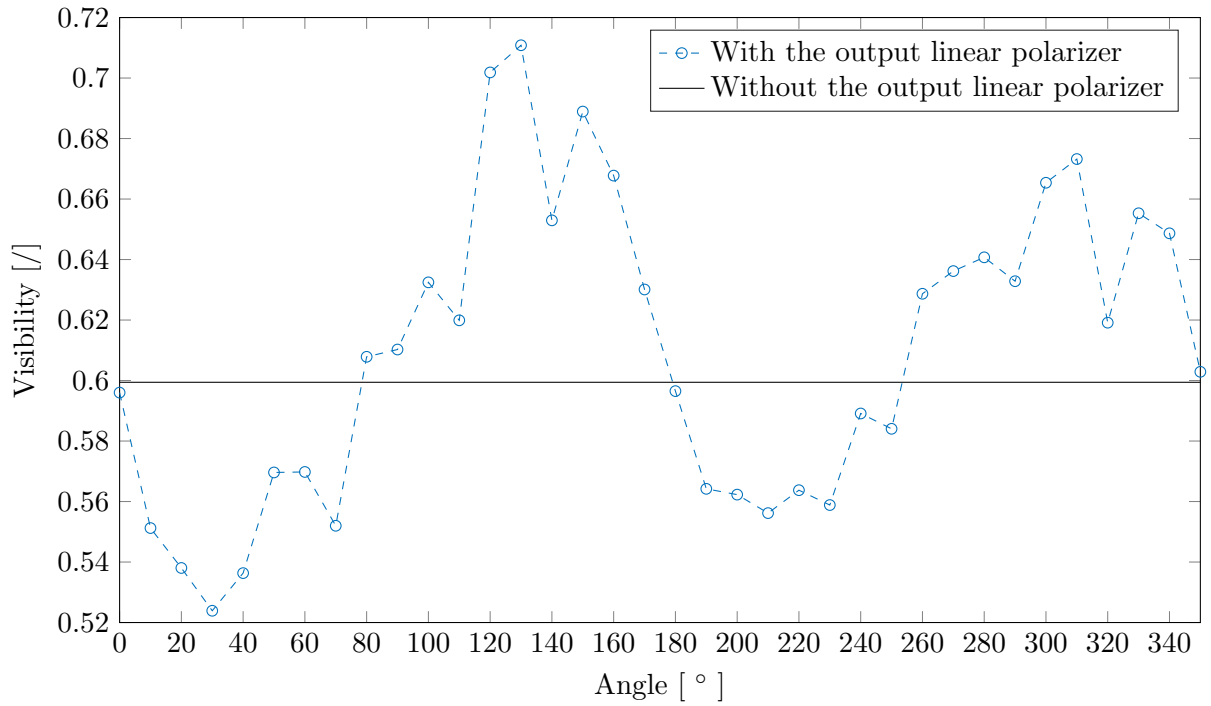

Figure 2.7: Mean fringe visibility of the He:Ne signal with respect to the polarization angle of the polarizer placed before the detection optics.

2.1.3 Divergence

All laser beams diverge. Beam divergence has consequences on both the contrast and the resolution of the FTS. Effect of beam divergence on the resolution of the spectrometer was theoretically analyzed in section 1.3.2. In this section, effect of beam divergence on the contrast is first addressed along with the selection of beam expanders that allow decreasing the divergence so that the contrast is not significantly impacted by the movement of the retro-reflectors. In a second part, influence of the beam divergence of the supercontinuum laser on the resolution is studied.

Beam expanders

Evolution of the spot size w with the distance z from the laser waist w_0 for a Gaussian beam is given by :

$$w(z) = w_0\sqrt{1+\left(\frac{\lambda z}{\pi w_0^2}\right)^2}, \tag{2.2}$$

where λ is the laser wavelength. Formally, the spot size is defined as half the width of the Gaussian intensity profile of the laser beam at a height $\frac{I_0}{e^2}$, where I_0 is the maximum of intensity and e is the mathematical constant of the natural logarithm [16, 17]. The beam waist corresponds to the width of the beam at its focus.

If the distance travelled by light in one of the two arms of the interferometer is longer than the distance travelled in the other arm, the spot size will be larger for this arm compared to the other spot size, leading to a ring in the image FOV where there is no spatial overlap and thus to a reduction of fringe visibility. To maximize contrast, the spot sizes of the two beams should remain close to each other, even for large optical path differences. The worst situation is encountered when the carriage is located at one extremity of the translation stage. In such a case, light travels about 6.75 m for one arm and 4.00 m for the other. Fortunately, it is possible to reduce the beam divergence by increasing the laser waist (see equation (2.2)). The evaluation of the expansion coefficient necessitates the knowledge of both the wavelength and the initial beam waist. These two features are specified in the datasheet of the supercontinuum laser and are summarized in Table 2.1. However, in the case of the He:Ne laser, only the wavelength is known and the beam waist has to be measured. To do so, the spot size is measured at two unknown distances z_1 and $z_2 = z_1 + l$ from the beam waist, where l is known and corresponds to the spacing in between z_1 and z_2. l is equal to 30 cm in our case. The intensity profile of the He:Ne laser beam was obtained with the help of the experimental setup shown in Figure 2.8. A very narrow slit (240μm) is translated perpendicular to the beam propagation direction and the intensity behind the slit is measured as a function of the slit lateral position. The measured intensity profiles at these two points are shown in Figure 2.9. Data are fitted by Gaussian functions. The spot sizes $w(z_1)$ and $w(z_2) = w(z_1 + l)$ are then evaluated analytically based on the fitting. The knowledge of these two values permits to estimate the waist by solving the following system of two equations with the two unknowns w_0 and z_1 :

$$\begin{cases} w(z_1) &= w_0\sqrt{1+\left(\frac{\lambda z_1}{\pi w_0^2}\right)^2} \\ w(z_1+l) &= w_0\sqrt{1+\left(\frac{\lambda (z_1+l)}{\pi w_0^2}\right)^2}. \end{cases} \tag{2.3}$$

The non-linear equation solver `fsolve` of MATLAB was utilized to do so. The system admits $w_0 = 0.40$ mm as a solution.

Table 2.1: Waist of the Fianium SC450-4 supercontinuum at different wavelengths. Information about the waist and the wavelength were found in the laser datasheet (Ref. [18]).

Wavelength [nm]	Spot diameter [mm]
530	1.5
633	2.0
1100	3.0

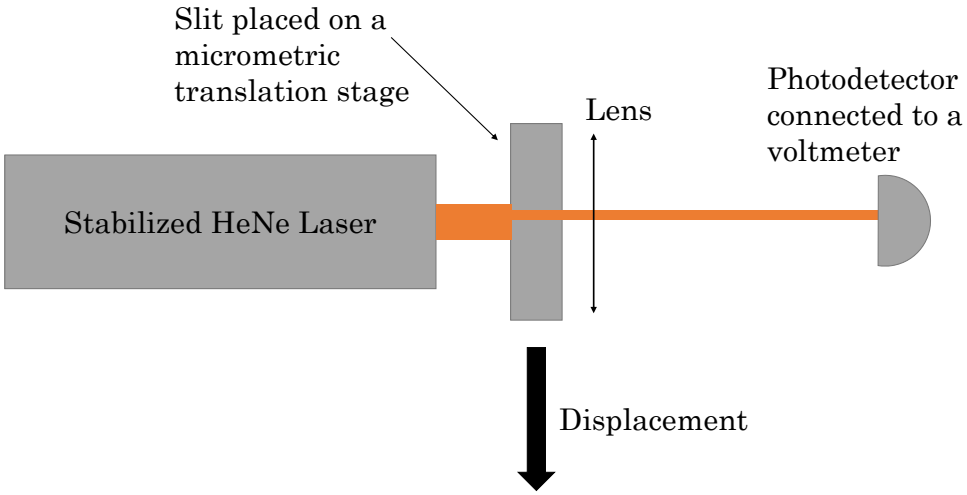

Figure 2.8: Experimental setup used for the measurement of the laser transverse mode profile.

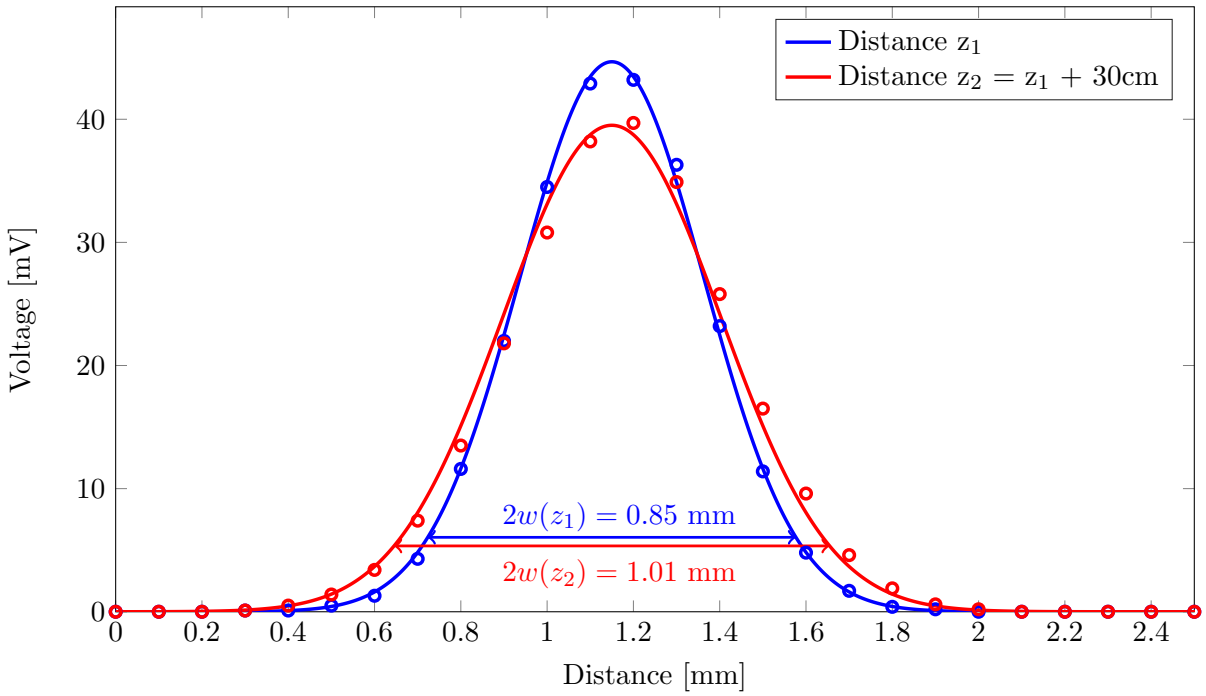

Figure 2.9: Intensity profile of the He:Ne laser at distances z_1 and $z_2 = z_1 + 0.3$ m from the waist w_0. Root mean squared error of the blue/red curve : 0.39 mV/1.03 mV.

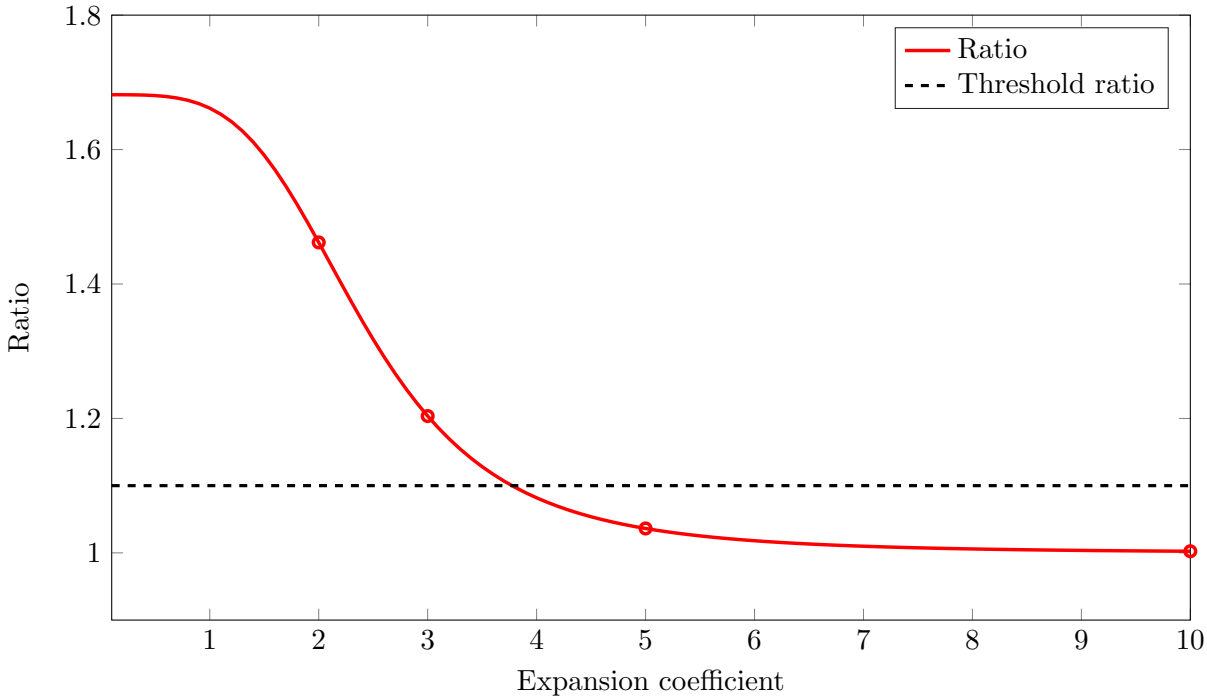

Figure 2.10: Plot of equation (2.4) with respect to the expansion coefficient for the He:Ne laser. The dashed black line is the 10% tolerance. Circled points are the expansion coefficients of the beam expanders available in the THORLABS catalog.

The beam expansion coefficient, denoted by c, was determined by imposing the variation in the spot size to be inferior to 10% in the worst case scenario. Figure 2.10 depicts the evolution of the ratio of the spot sizes of the two arms with respect to the expansion coefficient, that is :

$$\text{Ratio}(c) = \frac{w(6.75)}{w(4.02)}(c) = \frac{\sqrt{1 + \left(\frac{6.75\lambda}{\pi c w_0}\right)^2}}{\sqrt{1 + \left(\frac{4.02\lambda}{\pi c w_0}\right)^2}}. \tag{2.4}$$

The He:Ne beam waist must be expanded at least five times to satisfy the 10%-tolerance. Since the emission wavelength of the He:Ne is equal to 632.8 nm, the model of the beam-expander that was chosen is the GBE05-A of THORLABS with a 5× expansion ratio and which includes an anti-reflection coating that works properly in the 400-650 nm range.

The supercontinuum light source must be expanded as well to maintain the contrast as constant as possible on the complete trajectory of the carriage. The beam diameter of the light source varies with the wavelength. As already mentioned, values of the beam waist are specified in the datasheet of the supercontinuum source and are given in Table 2.1. In a similar manner to the He:Ne laser, evolution of the ratio of the spot sizes of the two arms with respect to the expansion coefficient c is obtained using equation (2.4) and it is plotted in Figure 2.11. The 10%-tolerance is fulfilled even for a beam expander with a 2× expansion ratio. However, it was out of stock and a beam expander with a 3× expansion ratio was bought instead. The model that was purchased is the GBE03-B of THORLABS with an anti-reflection coating that works properly in the 650-1050 nm range.

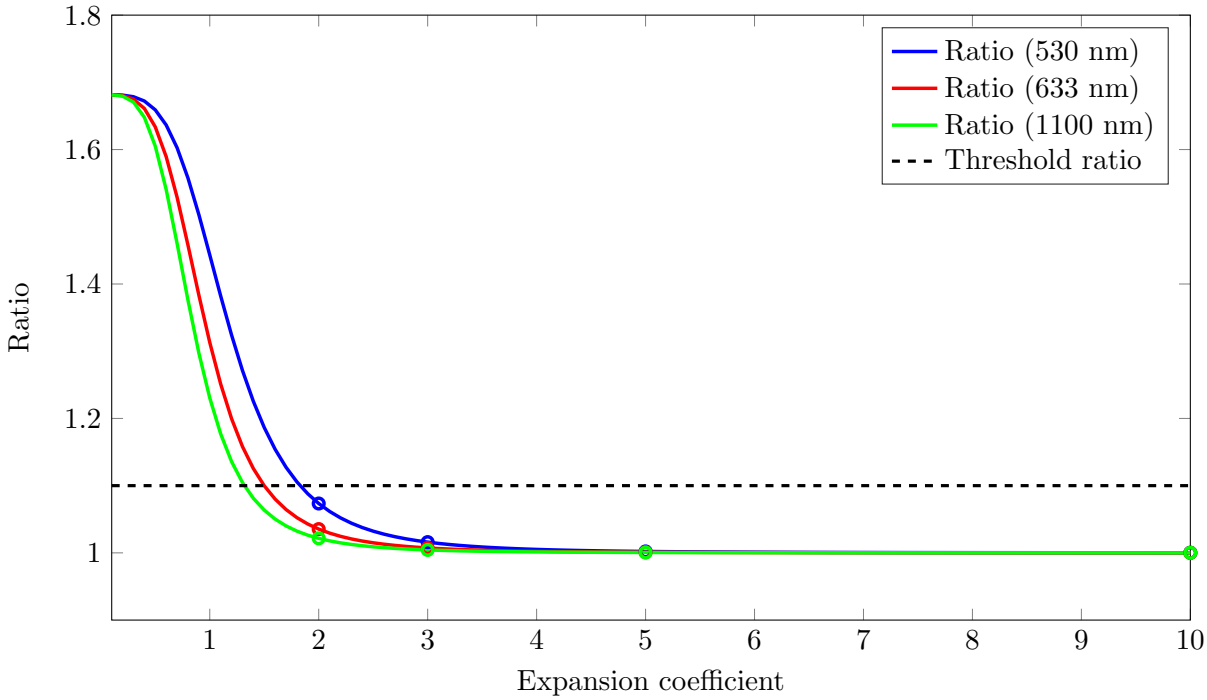

Figure 2.11: Plot of equation (2.4) with respect to the expansion coefficient for the supercontinuum laser at 3 different wavelengths. The dashed black line is the 10% tolerance. Circled points are the expansion coefficients of the beam expanders available in the THORLABS catalog.

Influence on the resolution

In section 1.3.2, it was shown that off-axis rays affect the resolution of the FTS. In usual FTS, the source that has to be characterized is not directional and it is necessary to first collimate the light. A typical collimation arrangement relies on the use of four mirrors : an off-axis ellipsoid mirror, an off-axis paraboloid mirror and two plane mirrors. This arrangement is sketched in Figure 2.12. The maximum divergence angle accepted by the system is determined by the spot size at the intermediate focus of the two aspherical mirrors. If the maximum divergence angle is too large, it can alter the resolution and it is of common practice to place a diaphragm at the intermediate focus. This diaphragm is the so-called Jacquinot stop which is present in all high resolution FTS. The determination of the aperture opening dimension represents a trade-off between the optical throughput and the achievable resolution. Indeed, opening the aperture allows increasing the amount of light that is accepted in the interferometer, but this is done at the expense of the resolution since a larger aperture implies a larger maximum divergence angle [7, 9].

However, in the present setup, a supercontinuum laser is used instead of more conventional light sources. Lasers are already collimated and highly directional, and no Jacquinot stop is required. However the waist dimension of the supercontinuum laser will play a role in the maximum divergence angle that can enter in the FTS. Supposing that the laser beam is Gaussian allows evaluating the maximum divergence angle α_{Max} thanks to the following equation :

$$\alpha_{\text{Max}} = \frac{\lambda}{\pi w_0}. \tag{2.5}$$

Once again, information available in the datasheet of the supercontinuum laser was used to evaluate the divergence angles at different wavelengths. The results are summarized in Table 2.2. To avoid loss in resolution due to the beam divergence, the maximal divergence acceptable

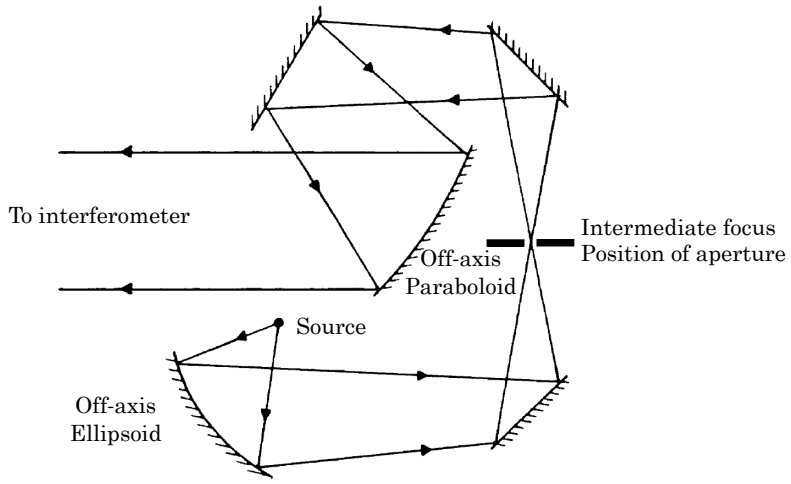

Figure 2.12: Typical source optics that incorporates a Jacquinot stop at the intermediate focus. From Ref. [7].

Table 2.2: Evaluation of the divergence angle of the Fianium SC450-4 supercontinuum. Information about the waist and the wavelength were found in its datasheet (Ref. [18]).

Wavelength [nm]	Waist [mm]	Divergence angle α_{Max} [°]		Tolerated divergence angle α'_{Max} [°]
		Expansion ratio ×1	Expansion ratio ×3	
530	0.75	$1.3 \cdot 10^{-2}$	$4.3 \cdot 10^{-3}$	$3.9 \cdot 10^{-2}$
633	1	$1.2 \cdot 10^{-2}$	$3.8 \cdot 10^{-3}$	$4.2 \cdot 10^{-2}$
1100	1.5	$1.3 \cdot 10^{-2}$	$4.5 \cdot 10^{-3}$	$5.6 \cdot 10^{-2}$

in the interferometer, denoted by α'_{Max}, has to be greater than the actual divergence angle α_{Max} of the laser beam. This maximal acceptable divergence can be evaluated by imposing the boxcar broadening due to off-axis rays, given by equation (1.43), to be equal to the FWHM of the sinc function associated with the finite optical path difference of the interferometer given by equation (1.43) [19]. Equaling these two equations gives :

$$\frac{1.207}{2\delta_{\text{Max}}} = \tilde{\nu}\left(1 - \cos(\alpha'_{\text{Max}})\right). \tag{2.6}$$

Since the maximum retardation δ_{Max} is known and equal to 2.7 meters, it is possible to evaluate α'_{Max} for a given wavenumber and to compare it with the divergence angle evaluated thanks to equation (2.5). The results are given in Table 2.2 as well. Since the divergence of the laser beam is always below the maximal divergence acceptable in the interferometer, either or not there is a beam expander, no loss in resolution is imputed to the divergence of the supercontinuum source.

2.2 Reference laser stabilization

As explained in section 1.4.1, a cw laser is used as a spatial reference in the FTS. In our setup, a He:Ne laser plays this role for several reasons : it provides an intense collimated beam, a narrow bandwidth, a high mechanical stability and good visibility [20]. Stringent constraints on the stability of the laser output frequency are imposed whenever precision length measurements are involved. Even slight variations in the laser cavity length lead to significant changes in the output frequency. In our case, these changes are mainly induced by thermal expansion of the discharge tube. Tight control of the cavity length is mandatory to stabilize the output

frequency of the He:Ne laser. This section is divided into four subsections. The theoretical background necessary to understand the stabilization scheme is first introduced in section 2.2.1. Section 2.2.2 then explains how stabilization is actually performed. Section 2.2.3 concerns the characterization of the laser stability. Finally, section 2.2.4 retakes the main results of the reference laser stabilization along with future improvements of the setup.

2.2.1 Theoretical background

Lasers usually consist of an amplification medium placed in an optical cavity. Both the amplification medium and the optical cavity geometry vary with the nature of the laser. These two features influence the output frequency of the laser. In the case of the He:Ne laser, the amplification medium is a gas mixture composed of helium and neon placed in a discharge tube. In our case, the cavity mirrors that build the optical cavity are directly sealed onto the ends of the discharge tube. The amplification medium and the optical cavity are introduced separately in the two following subsections. Each time, the factors that influence the output frequency are emphasized.

Amplification medium

He:Ne lasers are cw gas lasers that are based on radiative transitions in neon atoms. Composition of the gas mixture is approximately 85%He-15%Ne and the total pressure is about 1 Torr. Helium atoms are placed in the metastable energy level 2^1S_0 thanks to an electric discharge. These excited helium atoms provide selective excitation of the neon atoms by means of collisions. During the collisions, neon atoms are excited to the 5s energy level and they can then undergo stimulated radiative emissions to the 3p level. The wavelength of the photon emitted during this process is equal to 632.8 nm, the so-called red line of the He:Ne lasers.[1] Atoms in the 3p level then undergo a fast radiative decay to the 3s level. A last transition, from the 3s to the ground state ($1s^22s^22p^6$), occurs when neon atoms collide with the walls of the gas reservoir. Population inversion is easily maintained since the lifetime of the 5s energy level ($\approx$ 110 ns) is about five times longer than the lifetime of the level 3p ($\approx$ 20 ns). The energy-level diagram of Figure 2.13 summarizes all the information given in this paragraph [8, 16, 21].

Since the He:Ne laser is based on the 632.8 nm radiative transition of neon atoms, the profile of the gain curve should be approximated to a Lorentzian centred on the transition frequency with an FWHM equal to the A_{21} Einstein coefficient of the 5s $\rightarrow$ 3p transition, that is about 3.39 MHz [21]. In practice, it is not the case because the transition is broadened by the Doppler effect and the gain curve is best described by a Voigt profile, *i.e.* the convolution of the Lorentzian function resulting from the effective lifetime of the energy level with the Gaussian function associated with the Doppler broadening which is evaluated using the Maxwell-Boltzman velocity distribution (FWHM $\approx$ 1.5 GHz). Because of the several orders of magnitude between the FWHM of the Lorentzian and the FWHM of the Gaussian, the gain curve can be approximated to a Gaussian centred on the 5s $\rightarrow$ 3p transition frequency of the neon. Light amplification will occur only if the gain overcomes the losses. Thus, only the frequencies that are above a certain threshold represented by the dashed line in Figure 2.14 can result in light amplification [16].

[1] In practice, more than 200 other laser lines can be produced by neon atoms but they are of no interest for our purpose and they will not be discussed throughout this report.

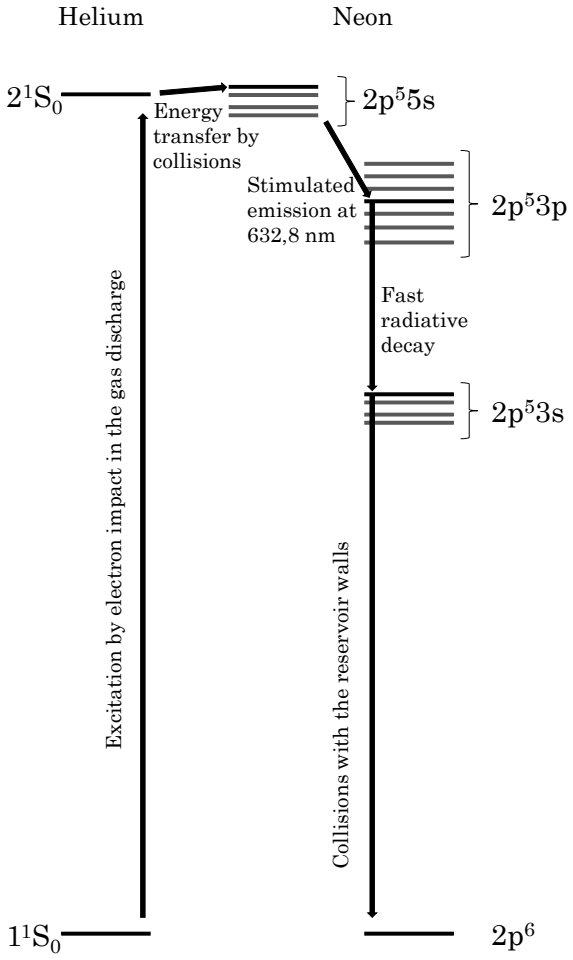

Figure 2.13: Partial energy level diagram of the helium and neon atoms relevant for the He:Ne laser emission at 632.8 nm.

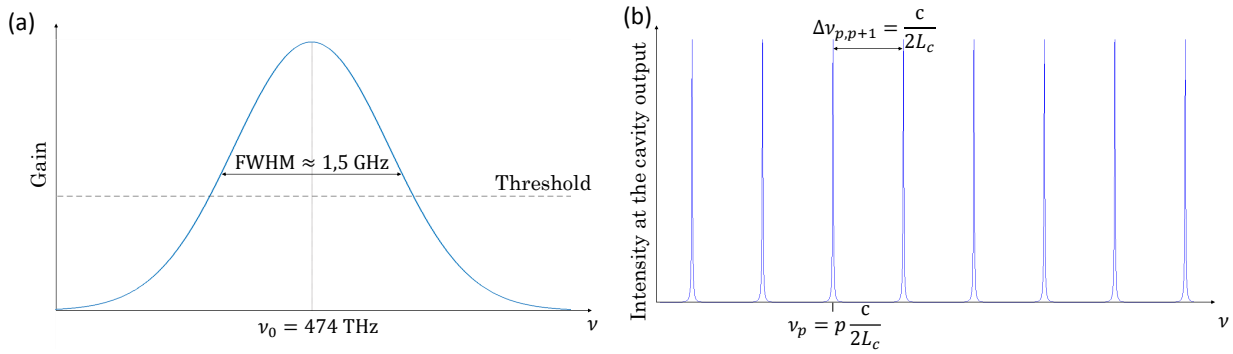

Figure 2.14: (a) Gain curve for a Doppler broadened He:Ne gas laser. The curve is approximated by a Gaussian centred in $\nu = 474$ THz with an FWHM of about 1.5 GHz. Light amplification occurs when the gain overcomes the losses, that is for a gain above threshold. (b) Intensity at the output of an optical cavity with respect to the frequency. L_c denotes the cavity length. The width of each peak depends on the cavity finesse.

Optical cavity

The optical cavity consists of two mirrors that are placed at both extremities of the tube in which the gas discharge takes place. The two mirrors form the so-called Fabry-Perot interferometer. Light bounces back and forth in between the two mirrors that build the cavity. At each reflection, some light passes through the mirrors. If they have a high reflection coefficient, only light that is resonant with the cavity is significantly transmitted. The optical cavity ensures that light travels a long distance before leaving the laser to maximize light amplification. One of the mirrors is a high reflector coated for maximum reflectivity, while the other transmits 0.5% to 1% of light [16].

A second feature of the cavity is to restrict oscillations to longitudinal modes that have frequencies determined by the cavity attributes (cavity length, mirror reflection coefficients, etc.). The frequency of the p^{th} mode can be approximated to :

$$\nu_p = p\frac{c}{2L_c}, \tag{2.7}$$

where L_c is the cavity length. The difference in frequency between two consecutive modes is the free spectral range (FSR) of the cavity. It is given by :

$$\Delta\nu_{p+1,p} = \nu_{p+1} - \nu_p = \frac{c}{2L_c}. \tag{2.8}$$

The intensity spectrum of the optical cavity consists of a comb of narrow peaks with a width that depend on the reflectivity of the mirrors, each peak being spaced by a frequency $\Delta\nu$ from adjacent peaks. The situation is depicted in Figure 2.14b. The cavity is also responsible for the directivity of the laser and for the transverse spatial profile of the laser beam. The divergence of the laser is lower than in the absence of the cavity [16].

When the amplification medium is placed between the two mirrors that build the cavity and if there is a population inversion between the energy levels involved in the stimulated optical transition, light will be emitted at frequencies for which the longitudinal modes of the cavity have a gain high enough to overcome the losses. In the case of the He:Ne laser, the spectral width of these longitudinal modes are very much narrower compared to the gain curve of the amplification medium [16]. The cavity of the He:Ne used in our setup is about 24 cm long. From equation (2.8), difference of frequency between the two modes is equal to 625 MHz. Up to three modes can be simultaneously emitted by the He:Ne laser for one atomic transition. Because of mode competition, two adjacent modes of the He:Ne laser have perpendicular polarizations [22].

2.2.2 Implementation

Since instabilities in the emission frequency of the He:Ne laser are mainly due to variations in the cavity length, tight control of the distance between the two mirrors of the resonator maintain these frequency variations to a minimum. One way to control the cavity length relies on the use of a heater placed around the plasma tube of the He:Ne laser. The heater allows making use of the thermal expansion of the discharge tube to control the cavity length. The behaviour of the heater is controlled by a feedback system.

For the feedback system to work properly, a setpoint has to be defined. The setpoint permits to define an error signal that characterizes the departure of the output signal from it. An appropriate response is generated from the error signal and allows correcting the output frequency of the He:Ne laser. An astute way to generate an error signal relies on the measurement of the intensity of the two modes that are sustained within the gain curve of the He:Ne laser. Indeed, the

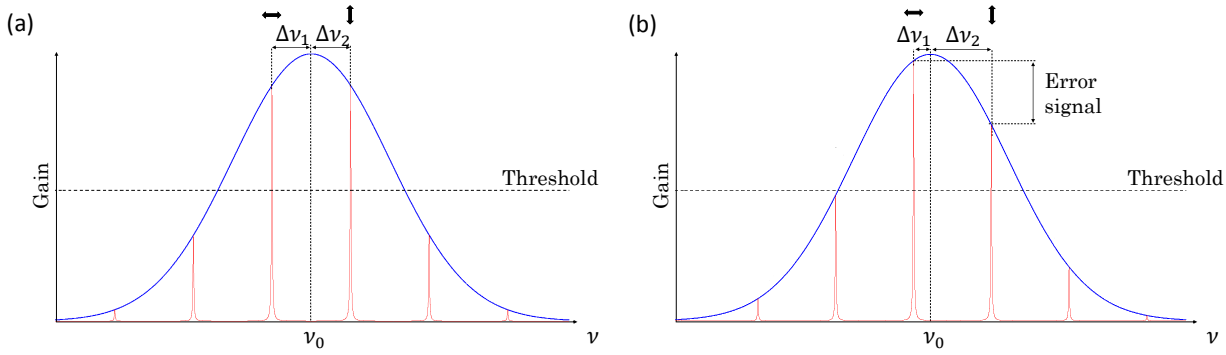

Figure 2.15: Gain profile of the He:Ne laser. The cavity modes are represented in orange. They determine the emission frequencies of the laser. Their position in the gain curve determines the emission intensity. Double-sided arrows indicate the polarization of the modes. (a) The two modes are symmetric with respect to the transition line at ν_0 ($\Delta\nu_1 = \Delta\nu_2$). They have the same intensity and the error signal is equal to zero. (b) The two modes are not symmetric with respect to the transition line at ν_0 ($\Delta\nu_1 \neq \Delta\nu_2$). They do not have the same intensity, resulting in a non-zero error signal.

intensity of a mode depends on its position in the gain curve, as shown in Figure 2.15. The error signal is obtained by subtracting the intensity of one mode from the other. If the two modes are symmetric with respect to the neon transition, as shown in Figure 2.15a, the error signal is equal to zero. However, if one mode is more intense than the other, like in Figure 2.15b, it results in a non-zero error signal that is processed by the feedback system which in turns controls the flow of current in the heater to counteract the change in intensity. A feedback system based on the intensity of the two modes sustained by the laser allows stabilizing the output frequency as well since the frequency is related to the intensity by means of the gain curve. It should be pointed out that the laser would be stable in any situation where the difference of output voltages at the photodetectors is kept constant [23]. However, imposing the two modes to have equal intensities permits to have a very good sensitivity on any frequency change since $\frac{\mathrm{d}I}{\mathrm{d}\nu}$ is maximum at this point [22].

To measure the intensity of each mode, they need to be spatially separated. Since the two lasing modes are polarized orthogonal to each other, a polarizing beamsplitter (PBS) allows to spatially separate them. Each mode is then measured by a distinct photodetector. Output voltages issuing from these two detectors are then subtracted from each other to create the error signal. The error signal is then processed by the feedback system which in turn controls a transistor that determines the current passing through the heater [21, 22]. The whole stabilization setup is depicted in Figure 2.16. It should be stressed that the stabilization system uses the low power output of the He:Ne laser. Therefore, stabilizing the laser does not put any constraint on the high power output that can be used for the FTS.

It is common practice to set the response of the system proportional to the instantaneous value of the error. However, the feedback system response is improved by adding integral and derivative responses as well. The integral part takes past values of the error into account in order to get rid of steady-state errors while the derivative part allows to avoid overshooting the setpoint and to damp out oscillations around it [22, 24]. These three responses form the so-called Proportional-Integral-Derivative control system (PID).

Fabrication of the stabilization setup was performed by Marc Daman who based himself on reference [22] for the implementation of the PID circuit.

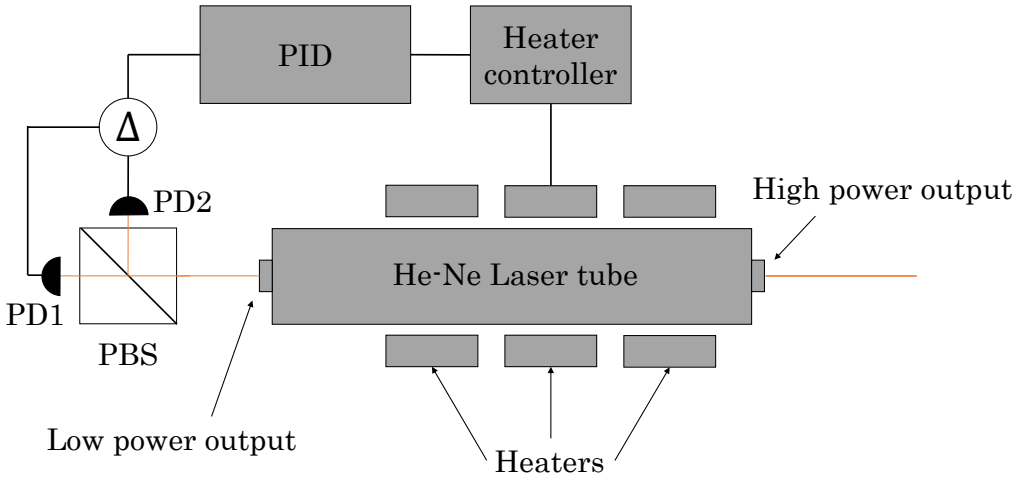

Figure 2.16: Laser Stabilization scheme. An error signal is generated thanks to the two orthogonal modes sustained by the He:Ne laser. This error signal is treated by the PID system which controls the heater placed around the plasma tube.

2.2.3 Characterization

Transient regime

Output frequency of the He:Ne laser depends on its cavity length. Before being switched on, the laser is at room temperature. When turned on, the laser produces heat. This heat production results in an uninterrupted rise of temperature of the discharge tube until thermal equilibrium is reached. The cavity length increases with temperature due to thermal expansion of the discharge tube, leading to mode sweeping in the gain curve. No overall change in intensity is observed at the output of the laser. However, if the two modes that can be sustained by the amplification medium are separated using a PBS, then substantial fluctuations in their intensity is observable [22, 25].

Intensity of the two polarizations of the He:Ne laser were recorded by measuring the voltage across the two photodetectors PD1 and PD2 of Figure 2.16. Variation in intensity with respect to time for one of the two polarizations is shown in Figure 2.17. The laser was switched on just before the record. Sinusoidal fluctuations in the intensity are due to mode sweeping. The period of the oscillations increases with time because the laser approaches its equilibrium temperature and thermal expansion slows down. The length of the cavity increases of $\frac{632.8\text{ nm}}{2}$ between a maximum of intensity and the adjacent minimum [25]. Therefore, finding the times of the maxima and minima in the sinusoidal intensity curve permits to get a good insight of the behaviour of the He:Ne laser in the transient regime and to obtain a good estimation of the time necessary to reach the steady-state regime. Figure 2.18 shows the cavity lengthening of the He:Ne laser against time. The red circles are the experimental data retrieved from the measurement shown in Figure 2.17. Expansion slows down as time passes by. However, the record is too short to observe the plateau that corresponds to the steady-state temperature. The experimental data were approximated by the following function $f(t)$:

$$f(t) = a * \left(1 - \exp\left(\frac{-(t-c)}{b}\right)\right), \tag{2.9}$$

where a, b and c are fitting parameters that were evaluated using MATLAB. They are respectively

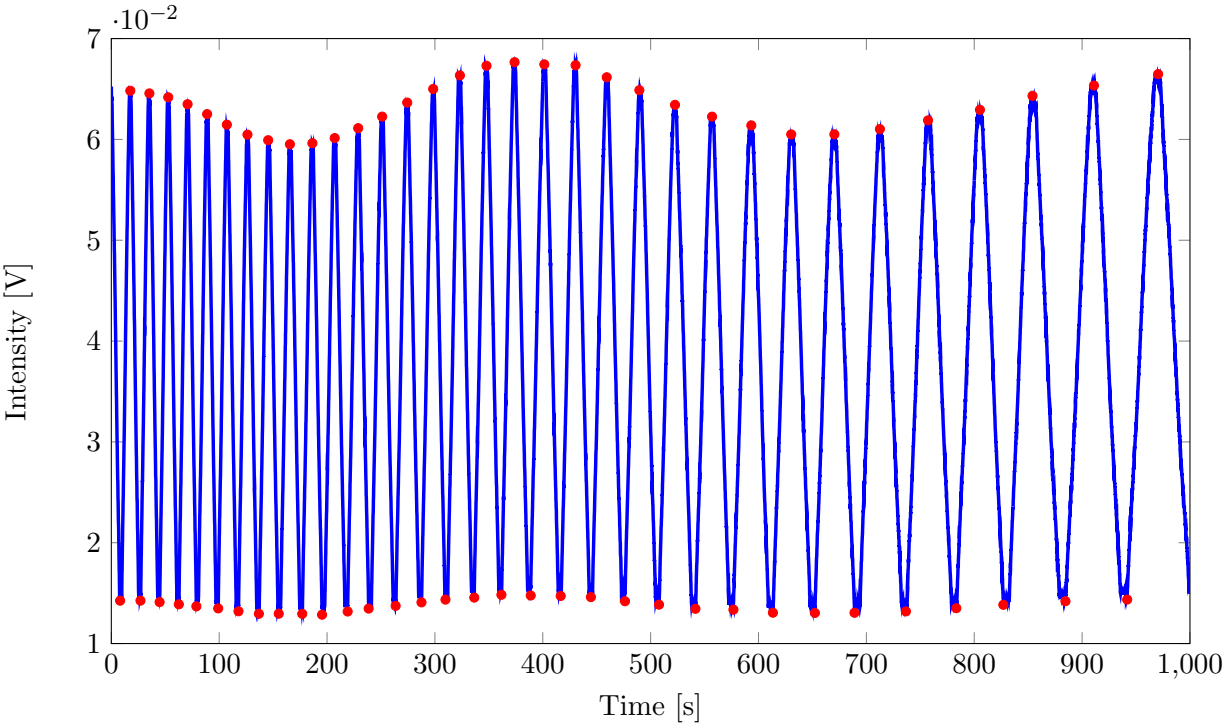

Figure 2.17: Intensity of one mode of the He:Ne laser with respect to time. The stabilization system is turned off. The red dots are the extrema in intensity used to plot Figure 2.18.

equal to 28060, 725.20 and 8.15. The resulting fitting curve is plotted in blue in Figure 2.18. The black dashed line corresponds to the asymptotic value of the steady-state regime. More than one hour is necessary to correctly stabilize the laser if no pre-heater system is used. Unfortunately, even small perturbations in the surrounding area of the He:Ne laser cause the laser to leave its equilibrium position, leading to variations in the output frequency. Using a stabilization scheme is therefore mandatory for our application.

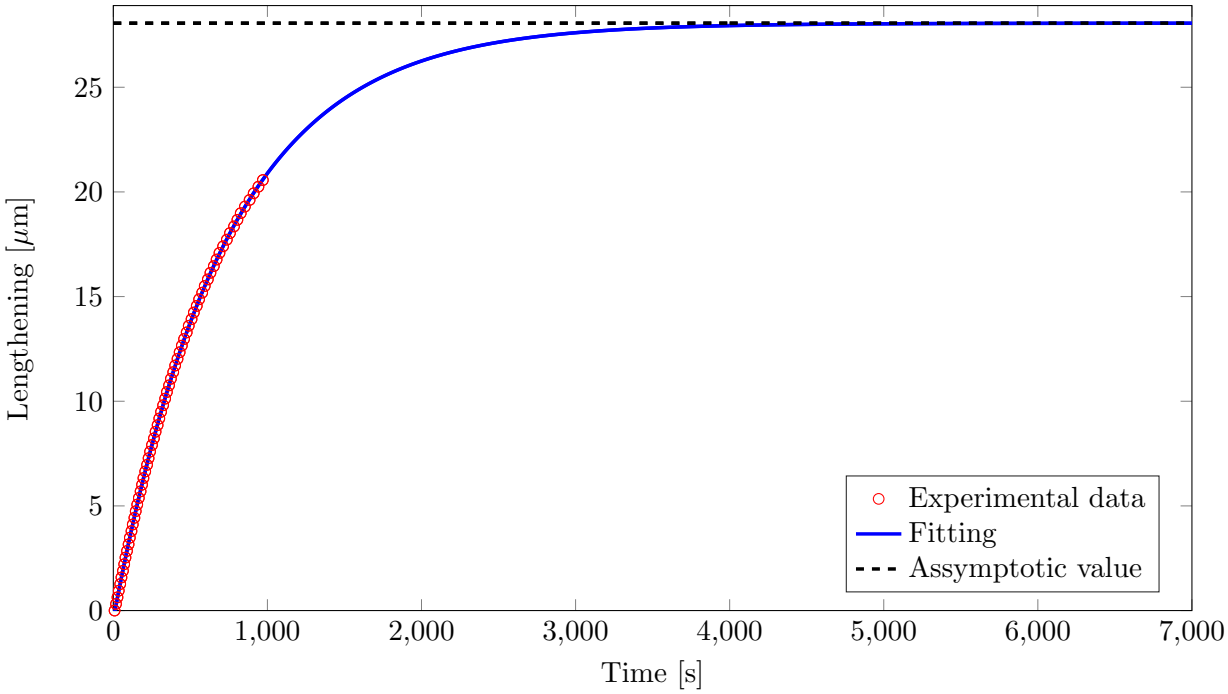

Figure 2.18: Lengthening of the laser optical cavity with respect to time. The root mean squared error of the fit is equal to 28.5 nm.

Steady-state regime

Figure 2.19 represents the experimental setup used to characterize the laser stability when it has reached its steady-state temperature. The main beam of the stabilized laser is injected in a temperature-stabilized Fabry-Perot interferometer. Frequencies that are transmitted by the Fabry-Perot interferometer depend on the distance between the two mirrors that build the cavity. Displacement of one of the mirrors modifies the cavity length, and thus the frequency of the transmitted light. This displacement permits to scan the free spectral range of the Fabry-Perot interferometer. The mirror displacement is performed with the help of a piezoelectric crystal.

Signal from the piezoelectric crystal controller is recorded along with the signal at the photodetector located behind the Fabry-Perot cavity. The first signal is only used to retrieve the information from the second one. A small portion of the recorded data is depicted in Figure 2.20. The signal from the piezoelectric controller is a step-like function generated by comparing the ramp function that actually controls the deformation of the piezoelectric crystal with a threshold value, as shown in Figure 2.20. When a mode of cavity of the Fabry-Perot interferometer matches with one of the longitudinal modes of the He:Ne laser, light is transmitted through the Fabry-Perot cavity and it reaches the photodetector. The free spectral range of the Fabry-Perot cavity is specified in its datasheet and it is equal to 1 GHz. Several free spectral ranges of the Fabry-Perot interferometer are scanned during a single voltage ramp applied to the piezoelectric crystal. Therefore, the pattern is repeated many times during a complete scan. Data were analyzed by only considering the first two peaks after a rising edge. Information about the stability in frequency of the He:Ne laser could not be directly measured with this experimental setup because a drift in frequency of the Fabry-Perot interferometer was observed. However, this information could be indirectly retrieved from the stability in intensity of the two modes since the emission frequency is related to the intensity by means of the gain curve. However, the Fabry-Perot interferometer allowed to ensure that only two modes of the He:Ne laser cavity were sustained in the gain curve and to evaluate in a precise manner the difference of frequency

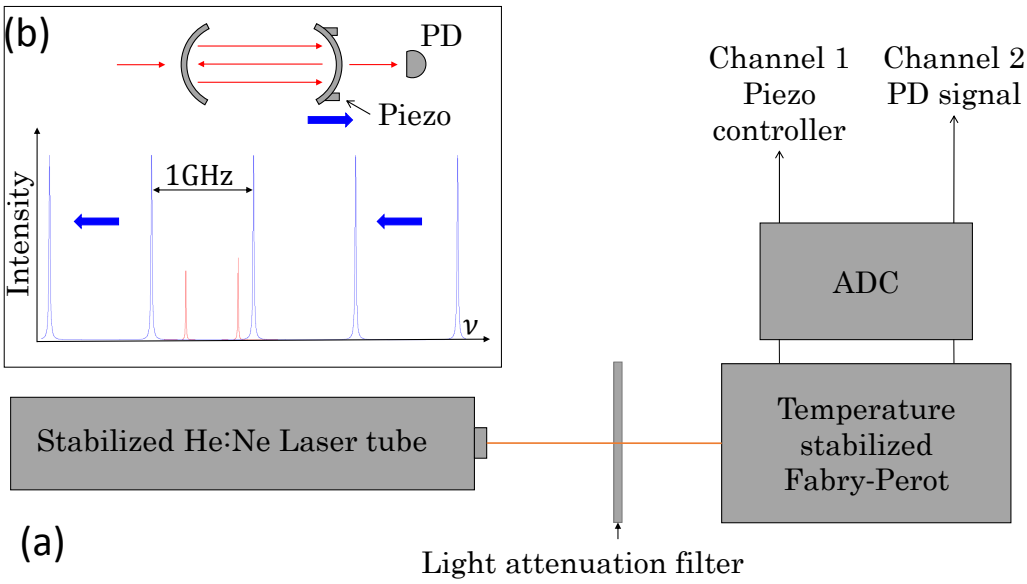

Figure 2.19: Experimental setup used for evaluating the performances of the frequency locking. (a) The main beam of the stabilized He:Ne is injected in a temperature stabilized Fabry-Perot cavity. Signal from the piezoelectric crystal controller is recorded along with the signal at the photodetector (PD) behind the Fabry-Perot cavity. (b) Modes of the He:Ne laser (in red) are detected by the PD when they match with the modes of cavity of the Fabry-Perot (in blue).

between these two modes. Indeed, the same peak pattern is observed for each rising edge of the voltage ramp and its replica is observed for each falling edge, *i.e.* two peaks with a small spacing in between them followed by one peak far apart from the first two peaks. The peak which is far apart corresponds to the same mode of the He:Ne laser than the first of the two other peaks. It is simply detected by another mode of cavity of the Fabry-Perot interferometer. A glance at Figure 2.19b facilitates the understanding.

As already mentioned, it is also possible to measure the difference in frequency between the two modes of the He:Ne laser. As a matter of fact, two peaks associated with the same mode are separated by the free spectral range of the Fabry-Perot, that is 1 GHz. Thus, difference in frequency between the two modes is given by the following equation :

$$\Delta\nu = \frac{\text{Index of the peak of mode 2} - \text{Index of the first peak of mode 1}}{\text{Index of the second peak of mode 1} - \text{Index of the first peak of mode 1}} \times 1 \text{ GHz}.$$

The difference in frequency is equal to 640 MHz. Since the He:Ne laser gain curve FWHM is about 1.5 GHz, only two laser modes can be sustained by the laser gain curve.

Figure 2.21 shows the intensity of the two modes against time. The He:Ne laser was stabilized and supposed at its setpoint at the time of the measurement and both channels of the Fabry-Perot interferometer were recorded. The data were then analyzed by only considering the first two peaks after each rising edge. Almost no change in intensity was observed during the first fifty minutes of the record. The two modes are not equal in intensity, perhaps because the gains of the two photodetectors PD1 and PD2 of Figure 2.16 are not perfectly equal. Since the output frequency of the He:Ne laser is related to its output intensity via the gain curve, the fact that the intensities of the two modes did not vary with time indicates that the laser was stable in frequency during these fifty minutes. The laser then left its setpoint for some unknown reason and it remained unstable during the rest of the record, *i.e.* more than seventy minutes.

The main drawback of the stabilization setup is that it can only heat up the discharge tube. In some situations, the tube should be cooled down to keep both modes equal in intensity but the

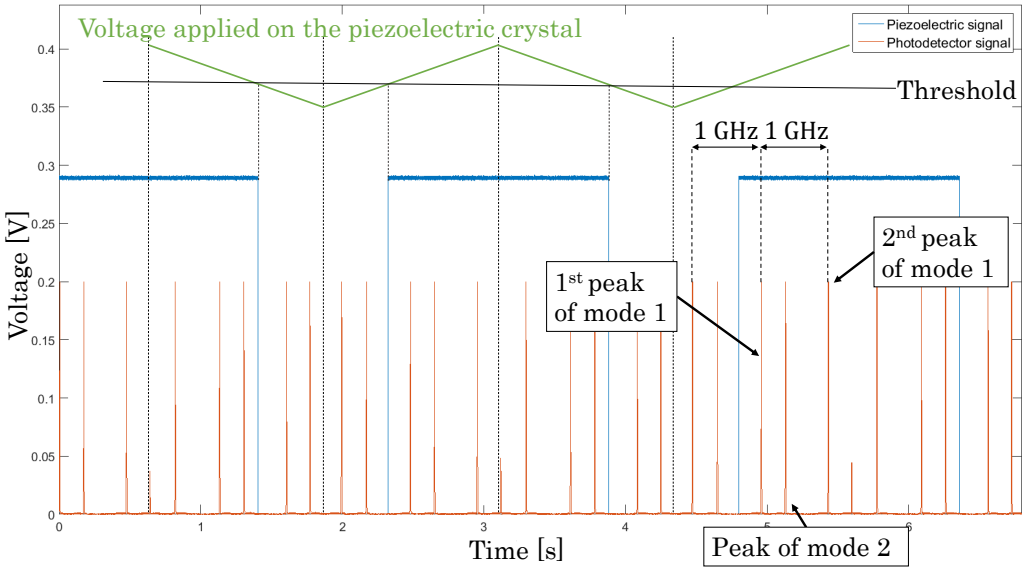

Figure 2.20: Small portion of the recorded data. Two signals were recorded : the output signal of the piezoelectric crystal controller in blue and the signal at the photodetector behind the Fabry-Perot cavity in red. There are two peaks per free spectral range of the Fabry-Perot cavity which is equal to 1GHz. The ramp voltage is schematically represented in green. The horizontal black line is the threshold value used to generate the output signal of the piezo controller.

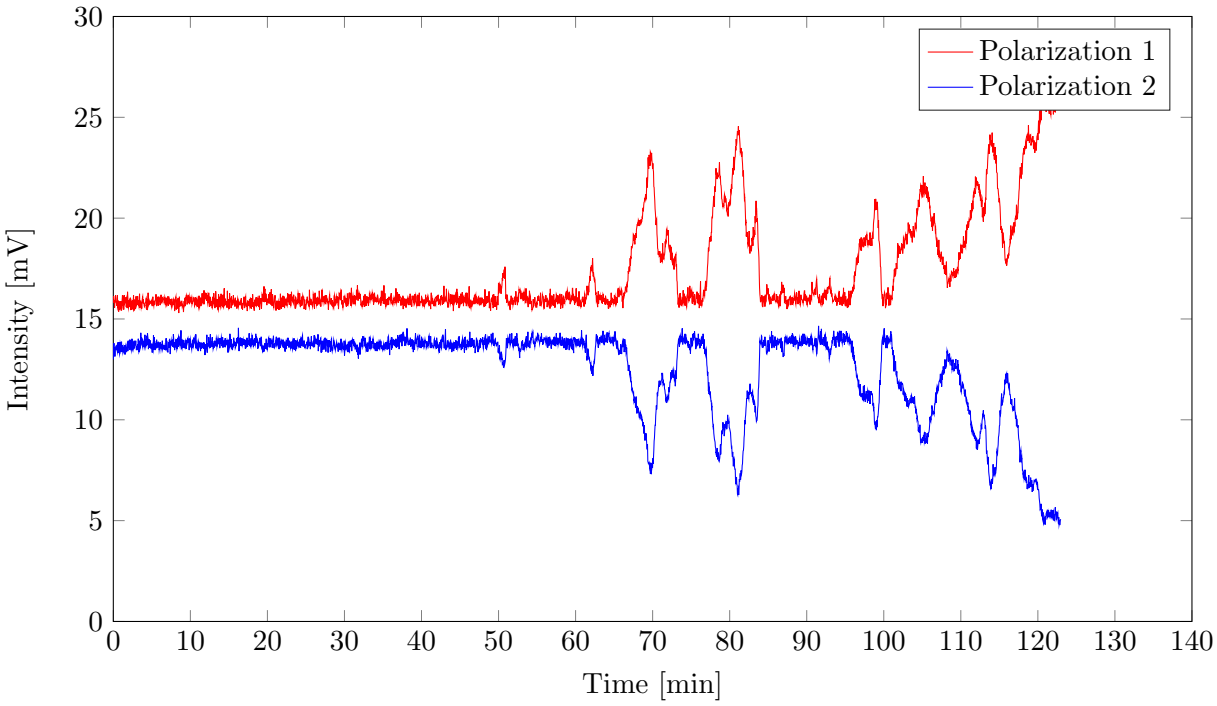

Figure 2.21: Intensity with respect to time for the two modes of the He:Ne stabilized laser.

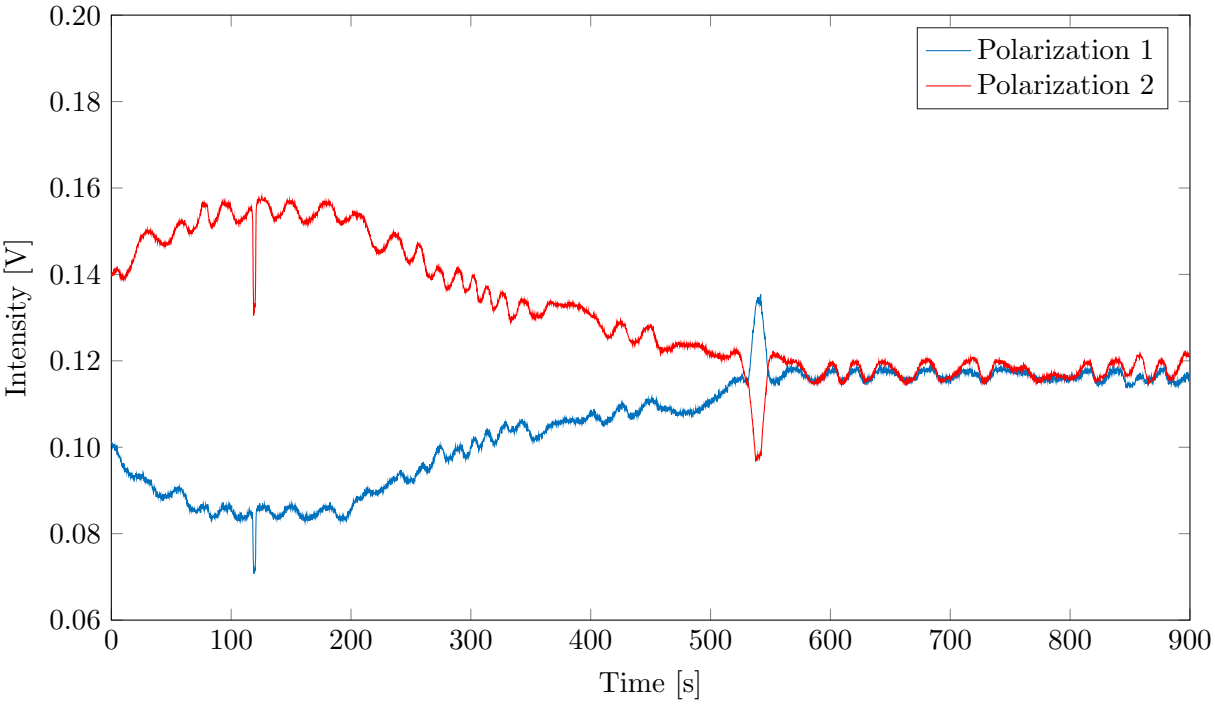

Figure 2.22: Intensity with respect to time for the two modes of the He:Ne stabilized laser. The stabilization scheme is turned on during the complete measurement. When the blue curve is under the red curve, the system cannot respond adequately to the perturbation, leading to a slow intensity drift of more than 500 seconds. When the blue curve is over the red curve, the system responds to the perturbation by heating the gas discharge tube.

PID cannot respond efficiently to the perturbation. When such a situation is encountered, the operator should switch off the system during a short period of time (about 5 seconds). Another solution is to wait long enough for the system to sufficiently cool down or heat up by itself so that the stabilization system can operate properly again. This problem is well illustrated by Figure 2.22. Intensity of both modes was recorded using the two photodetectors PD1 and PD2 depicted in Figure 2.19. The system cannot respond to the fact that polarization 2 is more intense than polarization 1 since the appropriate response would be to cool down the discharge tube. More than 500 seconds are necessary for polarization 2 to become equal to polarization 1. At that point, the error signal becomes equal to zero. If the intensity of polarization 2 becomes smaller than polarization 1, current flows in the thin resistance film as a response to the generated error signal. The cavity expands until the two modes have the same intensity again. If this point is not overshot, the two modes remain at the same intensity, as it is the case in Figure 2.22.

2.2.4 Conclusion

Slight changes in the laser cavity length can lead to variations in frequency of the He:Ne laser emission frequency. In our case, these changes are mainly induced by the thermal expansion of the laser optical cavity. Tight control of the cavity length allows stabilizing this frequency. Specifically, the stabilization scheme of our He:Ne laser relies on the measurement of the intensity of the two longitudinal modes with orthogonal polarizations at which it emits light.

The laser can be stable for sufficiently long periods of time to perform measurements with the Fourier transform spectrometer. However, it still suffers from several drawbacks. Firstly, there is no efficient pre-heating system. Therefore, it is necessary to switch on the laser at least

one or two hours before using it as a distance measurement reference for the Fourier transform spectrometer. Secondly, it is not possible to impose a particular polarization to be always located on the same side of the neon transition line. The reference laser frequency will thus vary of 640 MHz from one day to another. Also, there is no precise control of the equilibrium temperature and the reproducibility of the frequency is not guaranteed [26]. Finally, the only response of the stabilization system is to heat the discharge tube. The laser sometimes quit its stable regime due to some perturbation in such a way that the system cannot respond to the perturbation. The operator has to switch off the laser for five seconds in order to cool it down a bit.

Chapter 3

Data analysis

Besides the optics, an adequate acquisition system and a correct computational treatment of the data are two crucial aspects of a high resolution Fourier transform spectrometer. Indeed, information about the source spectrum can be retrieved only after having applied a mathematical operation : the Fourier transform. The quality of the spectra obtained with a Fourier transform spectrometer is dependent on the quality of the software that is used to analyze the data. Moreover, a good understanding of each step of the data acquisition and of the data processing pipeline permits to understand the artefacts related to the Fourier transformation. The goal of this chapter is to introduce and explain each step of the data analysis from the analog signal produced by the detector to the irradiance spectrum.

Section 3.1 concerns the data acquisition, that is the digitalization of the output signal of the FTS.

Section 3.2 develops one by one all the stages of the data processing pipeline.

The first interferogram that was recorded with the FTS and the resulting spectrum are discussed in section 3.3, where they are compared with interferograms and spectra obtained with commercialized spectrometers.

3.1 Data acquisition

Fourier transform spectroscopy implies to retrieve the irradiance spectrum from a given interferogram, meaning that the analog signal produced by the photodiode which measures the light intensity at the output of the interformeter has to be digitalized in order to be analyzed with the help of a computer. The analog-to-digital converter (ADC) is the device in charge of the digitization. ADCs have two functioning modes : they can be either triggered by an external signal or by a clock. The choice of the functioning mode is justified in section 3.1.1. The two main characteristics of an ADC are its maximum sampling frequency, *i.e.* the maximum amount of data it can acquire in a given time, and its resolution, that is how accurately the analog signal can be represented numerically. These two characteristics are respectively the topics of sections 3.1.2 and 3.1.3.

In this work, all the acquisitions were performed with a two-channels 16-bits Handyscope HS5 oscilloscope of TiePie working at 625 kHz. This oscilloscope will be denoted Tie-Pie in the rest of the text. The next three subsections only aim at justifying the requirements specification of the ADC in order to present guidelines for future improvements.

3.1.1 Uniform time-sampling

The irradiance spectrum of the source is retrieved from the interferogram by applying a Fourier transform, the Fourier conjugate variables being the wavenumber $\tilde{\nu}$ and the OPD δ. Thus, the interferogram has to be sampled at constant OPD before the transformation. The uniform OPD grid is obtained thanks to the use of a spatial reference; the He:Ne laser in our case (cf. section 1.4.1). Two different approaches allow achieving a spatial uniform sampling : either the data acquisition is triggered electronically from the zero-crossings of the He:Ne interferogram or the spatial uniform sampling is performed at the software level by recording both the He:Ne laser and the supercontinuum interferograms at constant time intervals. Both techniques present advantages but they also suffer from some drawbacks. They are compared in the next two paragraphs, alongside with the justification of the use of the uniform time-sampling technique for our homemade Fourier-transform spectrometer.

The first approach is a hardware approach. The clock signal of the ADC is generated by a circuit which detects the rising zero-crossings. The advantage is that the interferogram recorded following this method can readily be Fourier transformed. The computation time needed to obtain the spectrum is thus seriously reduced. Spectrometry at wavelengths smaller than 1265.6 nm cannot be performed if the interferogram of the supercontinuum is sampled only once per period of the He:Ne laser, otherwise aliasing will occur. Thankfully, it is possible to double the sampling frequency by detecting both rising and falling edges, extending the inferior wavelength limit to 632.8 nm. If the He:Ne signal is integrated and the falling and rising edges are detected on this new signal as well, it is even possible to extend spectrometry down to 316.4 nm. Unfortunately, these reference fringe subdivision methods are subject to sampling errors. For example, if there is any offset in the comparators used to sense the zero-crossings, a periodic error at the reference laser frequency could appear, leading to ghost lines in the irradiance spectrum [27].

A second approach consists in measuring both the He:Ne and the supercontinuum interferograms at constant time intervals and to generate a constant-OPD grid via a software evaluation of the zero-crossings of the He:Ne laser interferogram. It is then possible to create a denser constant-OPD grid from the knowledge of the times of the zero-crossings via a cubic interpolation. The supercontinuum interferogram is then resampled by interpolating it at the times of the reference fringe subdivisions [27, 28]. The second method was preferred to the first one due to its greater flexibility, to the possibility of recording higher frequencies and to the availability of the Tie-Pie oscilloscope. Moreover, the software method also permits to easily check the correct behaviour of the resampling. Finally, this technique permits to take advantage of commercial ADCs at an accessible price which are developed for other domains of applications, like the audio market, in which high-sampling frequencies ($\approx$ 1 Megasamples per second) and high resolution ($>$ 20 bits) are both required [27, 28]. Unfortunately, this method suffers from a severe drawback : it is computationally intensive to correctly resample an interferogram recorded on a large OPD. Interferograms taken on the complete translation stage (140 cm) can take several hours to be analyzed when one uses Matlab on an Intel E6750 processor working at 2.67 GHz.

3.1.2 Sampling frequency

The two interferograms have to be sampled over a certain sampling frequency to ensure that there are enough data to recover the true signals. At least two experimental data have to be measured on each period of the He:Ne laser to unequivocally define it. But, in practice, a minimum of 4 points per period must be taken to correctly evaluate the zero-crossings. Taking 4 points per period of the He:Ne also permits to measure enough information on the supercontinuum signal to perform spectrometry at wavelengths down to 316.4 nm without aliasing to occur. Since the data are recorded at uniform time intervals, the minimum sampling frequency is imposed by the

speed of the carriage by the following formula :

$$f_s = 16v\tilde{\nu}_{\text{He:Ne}}, \tag{3.1}$$

where f_s is the sampling frequency, v is the carriage speed in cm s^{-1} and $\tilde{\nu}_{\text{He:Ne}}$ is the wavenumber of the He:Ne laser in cm^{-1}. The factor 16 is due to the fact that 4 points are measured on a single period of the He:Ne laser and to the fact that the optical path difference is related by a factor 4 to the carriage displacement in our configuration, *i.e.* with the two corner cubes placed back-to-back in the carriage. Injecting the numerical value of the He:Ne wavenumber into equation (3.1) leads to :

$$f_s = 253v \text{ [kHz]}. \tag{3.2}$$

The first experimental data that have been measured were sampled at 625 kHz for a carriage displacing at 1.95 cm s^{-1}, meaning that almost 5 sampling points per period of the He:Ne laser were measured.

3.1.3 ADC resolution

ADCs convert analog signals into digital ones. The binary representation of the digital signal limits the resolution of the converter, that is precision with which it can convert an analog signal into a digital one. The resolution of the ADC is characterized by the number of bits that can be used to represent the analog signal. An ADC with N bits will be able to generate 2^N distinct discrete values. The full-scale voltage range, that is the range of voltages that can be coded by the ADC, is divided in $2^N - 1$ intervals. Two analog signals which lie in a same interval will be represented by a same discrete value. Most of the information is contained in the small ripples away from the centerburst. Inability to resolve them lowers the FTS resolution, no matter the maximum OPD allowed by the translation stage. The problem is even more important than the dynamic range of the interferogram, *i.e.* the ratio of the maximum intensity to the root-mean-noise level, is usually larger than 10^5 [7]. Figure 3.1 illustrates the consequences of a too-low ADC resolution by comparing the digitalized signals of a same interferogram sampled at two different ADC resolutions. The ripples on both sides of the centerburst are rapidly digitalized to zero in Figure 3.1a while they are discernible everywhere on the interferogram shown in Figure 3.1b.

In a near future, the `TiePie` oscilloscope used to record the first interferograms of the homemade FTS will be replaced by a 24-bits ADC. By way of comparison, the instrument presented in reference [29], which is at the state of the art, relies on a 22-bits ADC to sample interferograms. The authors indicated that an ADC with a resolution larger than 20 bits was necessary to get rid of digitization noise.

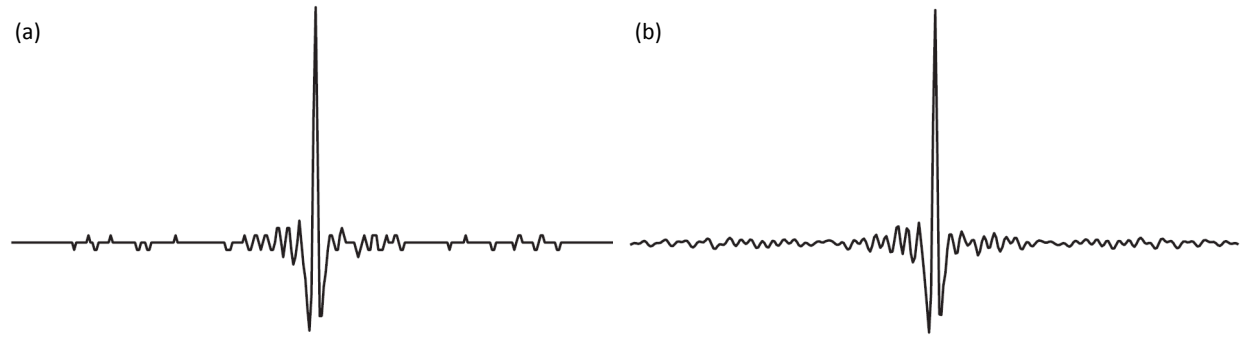

Figure 3.1: Same interferogram measured with the same FTS and sampled with (a) a 6-bits ADC (b) a 16-bits ADC. From Ref. [7].

3.2 Data processing pipeline

Before computing the spectrum of the supercontinuum laser, the raw data have to be measured and processed. The data processing pipeline used to analyze the first interferograms obtained with our homemade Fourier transform spectrometer is schematized in Figure 3.2. The beam of the supercontinuum laser passes through the gas sample under study and an optical bandpass filter. The role of the optical bandpass filter is to limit the passband of the supercontinuum laser to avoid aliasing. The supercontinuum and the He:Ne laser are injected in the Michelson interferometer. The output signals of the Michelson interferometer are measured by two photodiodes. They are recorded simultaneously by the two channels of the TiePie oscilloscope. The raw data are saved in a csv file in order to be processed on a personal computer.

The He:Ne signal is first digitally filtered to remove the out-of-range frequencies from the signal. Filtering of the He:Ne signal is the topic of section 3.2.1. In order to resample the supercontinuum on an uniform OPD grid, the times of the zero-crossings of the He:Ne laser signal have to be determined accurately. The way it is accomplished is the topic of section 3.2.2. The times of the zero-crossings are then used to resample the supercontinuum signal, as explained in section 3.2.3. After having resampled the supercontinuum signal, the data are numerically filtered with a bandpass filter to avoid aliasing and to suppress the dc and low frequencies from the signal. Section 3.2.4 concerns the function that carries out this task. The ultimate step before evaluating the Fourier transform of the interferogram is to place the centerburst at the centre of the vector containing the processed data and to ensure that the length of the vector is optimum to apply the Fast Fourier Transform (FFT) algorithm of Matlab. This step is detailed in section 3.2.5. A last function combines both the spectrum computation and the phase correction. This function is described in section 3.2.6.

All the functions that were used to process the data were written in Matlab, and the order in which they are introduced is the order in which they are invoked in the data processing pipeline. This order is based on references [28, 30, 31]. Some of the steps are illustrated by graphs plotted using the raw data of the first interferogram measured with the homemade FTS. To obtain the interferogram, the gas sample mentioned above was replaced by an optical bandpass filter with a FWHM of 10 ± 2 nm and a center wavelength of 750 ± 2 nm : the FB750-10 filter of Thorlabs. Advantages of using such optical filters in the development process of the FTS are that even very low resolution interferograms can be measured and that the resulting spectrum is a priori known, *i.e.* a Gaussian centred at 750 nm and with a FWHM of 10 nm.

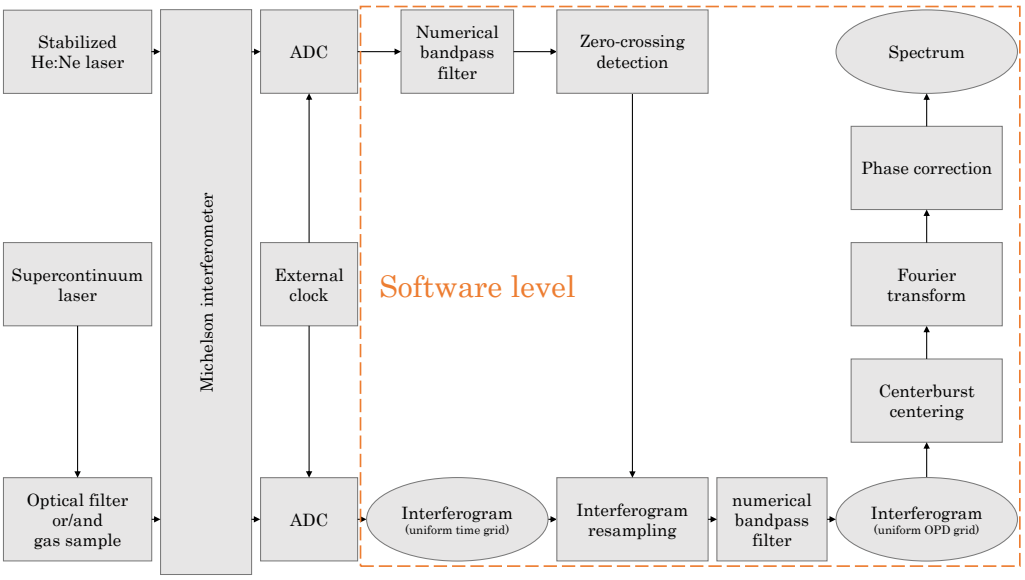

Figure 3.2: Data processing pipeline of the homemade Fourier transform spectrometer. The rectangular boxes represent the different stages of the process and the oval shapes represent the intermediate states of the supercontinuum signal. The stages that are performed at the software level are the ones contained in the dashed orange frame.

3.2.1 Reference signal filtering

The first step of the process is to apply a numerical bandpass filter on the He:Ne signal. Removing the low out-of-range frequencies allows getting rid of the dc component of the signal and to ensure that the average baseline of the sine wave is as close as possible to zero. This has to be done for the zero-crossing detection algorithm presented in the next section to work properly. Removing the high frequencies reduces the noise in the signal and smooths the data. The filtering relies on the use of a Butterworth bandpass filter designed with the function `butter` of MATLAB. The normalized passband of the filter is fixed and equal to 0.1-0.9, meaning that all the frequencies that are smaller to one tenth of the Nyquist frequency and those which are larger than nine tenths of the Nyquist frequency are removed. The signal is sampled at 625 kHz, and the Nyquist frequency is thus equal to 312.5 kHz. The bandpass frequency range of the filter is 31.25 kHz - 281.25 kHz. If the carriage mean speed is equal to 1.96 cm s^{-1}, the frequency of the sine wave of the He:Ne signal is about 125 kHz and the filter does not alter it at all. The reference signal is filtered by invoking the function `filterTheReferenceSignal.m` which takes the unfiltered data as an input and which returns the filtered data as an output. Its code is presented in appendix C.2.

3.2.2 Zero-crossing detection

After having filtered the reference signal, the times of the zero-crossings can be estimated with high accuracy. The method suggested by Yang *et al.* (see Ref. [28]) consists in interpolating between the data to determine the times of the zero-crossings. Since zero-crossings provide information about the carriage position, interpolation of the supercontinuum signal at the times of the zero-crossings allows retrieving a constant OPD-grid from the uniform time-sampling grid. The code of the function `findTheZeros.m` that was implemented to fulfill the task is given in appendix C.4. The inputs of this function are the values of the He:Ne interferogram and their indexes. Using the indexes as an input argument permits to subdivide the data into sub-datasets for the case where the initial dataset is too large to be completely loaded into the

memory. For a correct estimation of the zero-crossings, at least four points per period of the reference signal are needed. This value was determined by evaluating the mean percentage error and the mean absolute error between the computed zero-crossings and the analytic zero-crossings of an analytical sinusoidal function. The function `findTheZeros.m` returns a vector containing the fractional indexes for which the He:Ne signal is vanishing. The working principle of the function `findTheZeros.m` is illustrated in Figure 3.3 and it is developed step by step just below.

1. Supplementary data points are generated thanks to the function `interp` of MATLAB, which inserts zeros into the original signal and then applies a lowpass interpolating filter to the expanded sequence. The amount of data is multiplied by 8, as suggested in Ref. [28]. The supplementary data points are represented by blue squares in Figure 3.3 while the blue bullets correspond to the input data.

2. The indexes of the points located just before a zero-crossing are determined using the following formula :
$$\texttt{diff}(\texttt{sign}(signal))) = 0; \tag{3.3}$$
where the function `sign` returns the sign of each entry of the vector *signal*, that is +1 if $signal > 0$, -1 if $signal < 0$ and 0 if $signal = 0$. The function `diff` returns a vector containing the differences between adjacent entries of a vector in MATLAB. When there is a zero-crossing, the difference is equal to zero. The indexes of the zero-crossings are then determined by finding all the entries that are equal to zero in the vector resulting from the use of the formula above.

3. For each detected zero-crossing :

   (a) the same number of points is taken from both sides of the zero-crossing and these data are interpolated by a cubic function which is traced in green in Figure 3.3. The optimal number of points for the cubic interpolation is equal to 10 and it was determined in a similar way to the optimum number of points per period that have to be measured;

   (b) The roots of the function are evaluated and the ones that do not correspond to the actual zero-crossing are rejected. The remaining root corresponds to the fractional index at which the signal is vanishing. The zero-crossings are depicted by the red triangles in Figure 3.3.

The time complexity of this function is linear, meaning that the execution time t varies linearly with the length n of the input vector. The execution time can be estimated with the following formula :
$$t(n) = 4.10 \cdot 10^{-4} n + 0.1243. \tag{3.4}$$
The two numerical coefficients were evaluated on a personal computer with an Intel E6750 processor working at 2.67 GHz (released in 2007). If 5 points are measured on a single period of the He:Ne laser, and if the complete course of the translation stage is used, more than 44 million points must be analyzed. The execution time is about 5 hours long. This function is clearly the rate determining step of the data processing pipeline.

Another approach, suggested by Brault (see Ref. [27]), consists in determining the times of the zero-crossings analogically. It considerably reduces the time needed to analyze the data. In this approach, the signal of interest is still sampled at constant intervals of time. The working principle of the method is represented in Figure 3.4. Positive-going zero-crossings are detected with the help of a discriminator circuit, but instead of triggering the data acquisition, the square signal generated by the discriminator is used to gate an interval timer that permits to determine the times of the zero-crossings with a precision that depends on the frequency of the high frequency clock. Increase in the spatial sampling frequency is made possible by interpolating

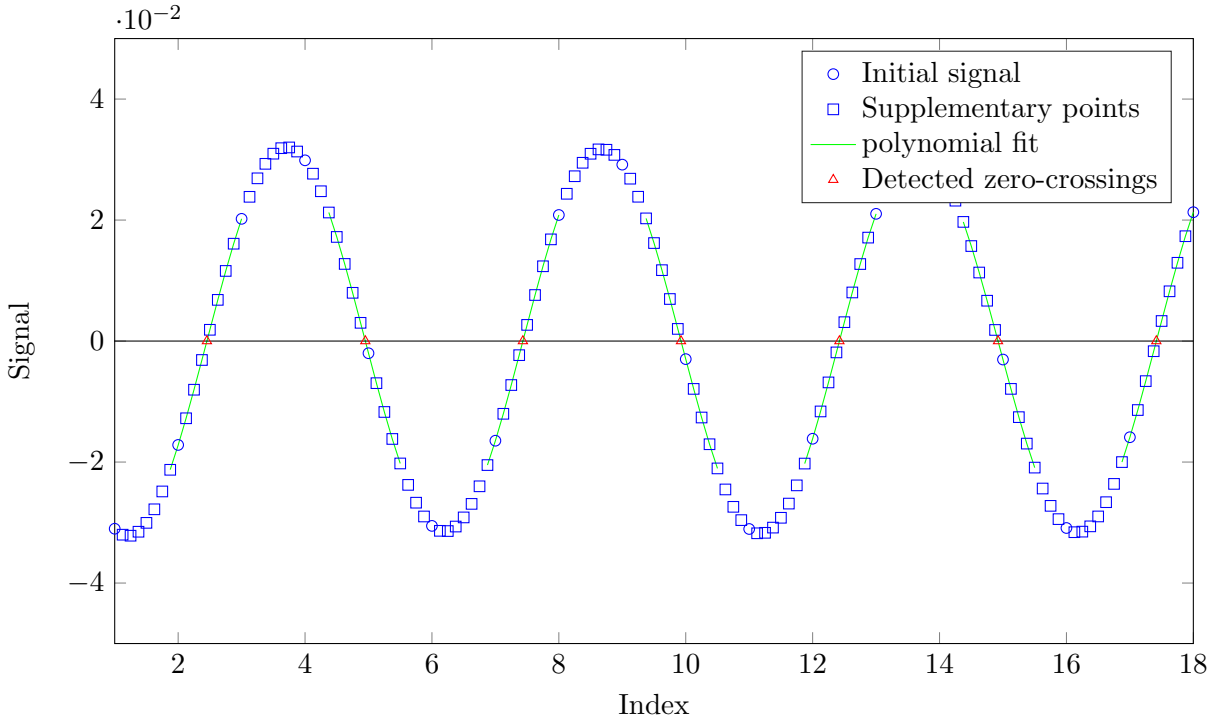

Figure 3.3: Illustration of experimental data of the He:Ne signal and the treatment of this signal by the function `findTheZeros.m`.

between the zero-crossings determined by the analog circuit and associated times. The number of ticks of the clock also permits to determine precisely the velocity of the carriage and to correct for errors arising from velocity fluctuations during the resampling process of the signal of interest.

[h!]

3.2.3 Interferogram resampling

Once the fractional indexes of the zero-crossings are accurately known, it is possible to resample the supercontinuum signal on an uniform OPD grid using the function `interp1` that is already implemented in MATLAB. The function allows to evaluate the values of the supercontinuum

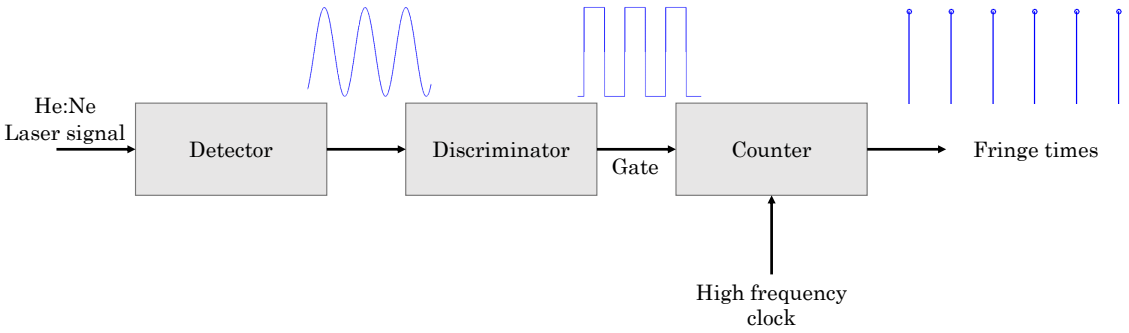

Figure 3.4: Measurement of the times of the zero-crossings with an interval timer. The figure is inspired from Ref. [27].

signal at the times of the zero-crossings. The three input arguments of this function are the signal sampled on the uniform time grid, the indexes of these values and the fractional indexes corresponding to the zero-crossings. It then gives back the values of the supercontinuum signal at these new indexes. The interpolated values are evaluated by means of a cubic interpolation.

The interferogram resampling, as performed here, was suggested by Yang *et al.* (see Ref. [28]). Another method, initially suggested by Brault (see Ref. [27]) is more efficient, but more complicated to implement.

3.2.4 Supercontinuum signal filtering

After having resampled the supercontinuum signal on the uniform OPD grid, the signal is filtered with a numerical bandpass filter. The removal of low frequencies allows to only keep the interferometric term of the supercontinuum signal while the removal of the high frequencies permits to avoid aliasing. Even if an optical filter is placed in the setup to ensure that the supercontinuum lies at frequencies below the Nyquist frequency, some high frequency noise can still remain and it has to be removed. In a similar way to the reference signal filtering, a Butterworth filter was used for the supercontinuum signal which is invoked when applying the function `filterTheSignal.m` to it. This function takes three input arguments : the resampled supercontinuum signal and the two cutoff wavelengths that determine the passband of the filter. The code of the function `filterTheSignal.m` is given in appendix C.3. The filtering step of the supercontinuum signal is performed after having resampled it on an uniform OPD grid to know exactly what are the cutoff wavenumbers, or equivalently the cutoff wavelengths of the digital filter. Indeed, the bandpass of the digital filter is implicitly expressed in terms of the Nyquist frequency which is equal to 15802.8 cm^{-1}, *i.e.* $\frac{1}{\lambda_{He:Ne}=632.8\cdot10^{-7}\text{ cm}}$, via the use of the normalized frequencies in the call of the function `butter` of MATLAB.

3.2.5 Centerburst recentering

Before taking the Fourier transform of the supercontinuum interferogram to obtain its spectrum, one more step is necessary : the vector containing the data has to be modified to place the centerburst at its centre and the same number of points has to be taken on both of its sides in order to obtain an interferogram as symmetric as possible. Importance of the symmetry of the interferogram with respect to the centerburst was explained in section 1.2.2. To do so, a simple algorithm inspired from reference [32] was implemented. The maximum of the signal is first located using the function `max` of MATLAB. There is few chances that this sampled point actually represents the optical contact, *i.e.* the true maximum of the interferogram. Therefore, to determine on which side of the true centerburst this point is located, a weighted sum of 128 terms taken on both sides of the maximum is evaluated, that is :

$$\text{weighted sum} = \sum_{i=-64}^{64} i\,|I_s(i)|\,, \tag{3.5}$$

where $I_s(i)$ is the i^{th} value of the signal with respect to the centerburst. Therefore, $I_s(0)$ corresponds to the centerburst. If the weighted sum is negative, the maximum value has to be located at the index[1] $N/2$, otherwise, it is located at the index $N/2+1$, where N is the largest power of two which is smaller than the length of the input vector, *i.e.* the interferogram. The new vector is shorter but its length is now equal to a power of two, making the fast Fourier transform algorithm more efficient than if it was not the case. Also, if all the interferograms are expressed

[1] In MATLAB, the index of the first element of a vector is equal to 1.

on the same OPD grid, *i.e.* two successive data are separated by the same distance and the scale positioning is fixed by the position of the centerburst, interferogram coaddition becomes straightforward. Coaddition was not mentioned before, but it simply consists in taking several inteferograms in the same experimental conditions and adding them in order to improve the signal-to-noise ratio (SNR). Unfortunately, it must be outlined that some of the information is lost since an important number of points is removed at the two extremities of the interferogram. However, by optimizing the distance travelled by the carriage, it is possible to minimize the number of points that have to be rejected. The centerburst recentering is performed with the help of the function `centerTheBurst.m` which is available in appendix C.1.

3.2.6 Phase correction and spectrum computation

The last two steps of the data processing pipeline are performed by invoking a single function : `getTheSpectrum.m`. This function evaluates both the normalized spectral irradiance of the signal and the wavenumber axis necessary to plot the spectrum from the resampled and recentred supercontinuum signal. The Fourier transform of the interferogram is evaluated via the FFT algorithm of MATLAB. As explained in section 1.2.2, since the double-sided interferogram is a real and even function with respect to the OPD, its Fourier transform has to be real and even as well. Therefore, only half of the output vector of the fast Fourier transform algorithm corresponds to the positive wavenumbers, and the other half is rejected. In practice, it is necessary to first correct the phase in order to obtain the irradiance spectrum of the source under study. Indeed, there are few chances to directly retrieve a real and even spectrum from the experimental data, and this for two main reasons. Firstly, none of the sampling positions usually coincides with the true centerburst, leading to a phase that varies linearly with the wavenumber. Secondly, the interferogram may be intrinsically asymmetric because of wavenumber-dependent phase delays in the optics, detectors, amplifiers and electronic filters of the setup [31]. The complex spectrum, denoted by $C(\tilde{\nu})$ can be represented by the sum of a real and an imaginary parts $R(\tilde{\nu})$ and $I(\tilde{\nu})$:

$$C(\tilde{\nu}) = R(\tilde{\nu}) + \mathrm{j}I(\tilde{\nu}), \tag{3.6}$$

or equivalently, by the product :

$$C(\tilde{\nu}) = S(\tilde{\nu}) \exp\left(\mathrm{j}\Phi\left(\tilde{\nu}\right)\right). \tag{3.7}$$

In this equation, $S(\tilde{\nu})$ is the true amplitude spectrum and $\Phi\left(\nu\right)$ is the phase. The aim of the phase correction is to extract the amplitude spectrum $S(\tilde{\nu})$ from the complex spectrum $C(\tilde{\nu})$. This can be achieved by multiplying $C(\tilde{\nu})$ by the inverse of the phase exponential and by taking the real part of the result :

$$S(\tilde{\nu}) = \mathrm{Re}\left[C(\tilde{\nu}) \exp\left(-\mathrm{j}\Phi\left(\tilde{\nu}\right)\right)\right]. \tag{3.8}$$

In the function `getTheSpectrum.m`, phase correction is applied to the complex spectrum by using equation (3.8).

For the moment, the configuration of the interferometer is optimized to take double-sided interferograms. In practice, to take full benefits of the translation stage length, single-sided interferograms should be measured instead. In such a case, phase correction is more complicated to implement. The double-sided interferogram is retrieved from the single-sided interferogram by measuring only a small extension of the interferogram beyond zero path difference. The phase error theoretically varies in smooth fashion with respect to the wavenumber, and that small extension is used to evaluate the phase of the whole interferogram [33]. However, this characteristic feature is not observed in our case. Figure 3.5 shows the phase angle with respect to the wavenumber before and after multiplying it by the inverse phase exponential. The phase

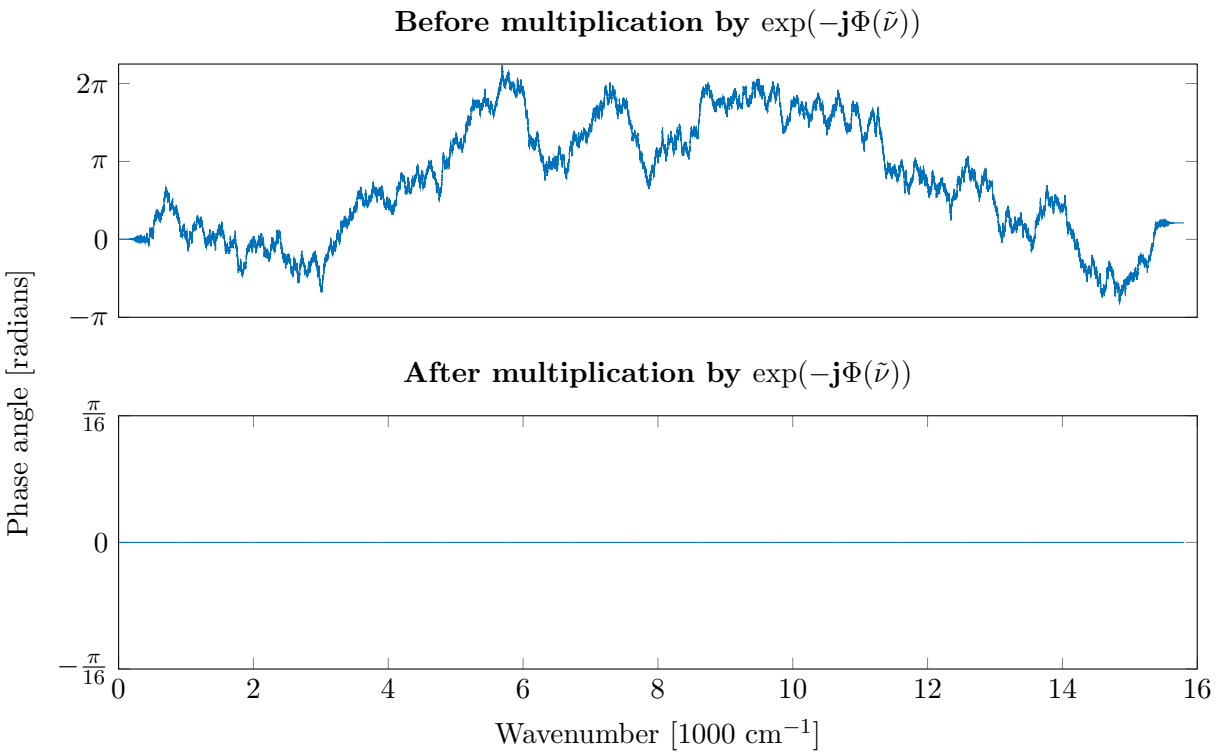

Figure 3.5: Phase angle with respect to the wavenumber before and after multiplying the complex spectrum by the inverse of the phase.

is equal to zero after doing so, but recording a single-sided interferogram and extrapolating the phase of the complete interferogram is clearly impossible in our case because of its erratic behaviour. Figure 3.6 shows the spectrum before and after applying the phase correction. Correcting the phase diminishes considerably the fast oscillations in the peak located at 13333 cm^{-1} but the SNR seems to deteriorate. The causes of the poor SNR are not clearly identified for the moment but variation in the carriage velocity is suspected to be amongst them. The carriage velocity was characterized by evaluating the difference of fractional indexes between successive zero-crossings. Velocity with respect to the carriage displacement is plotted in Figure 3.7, along with its representation in the frequency domain. The signal is periodic and the four main frequencies that compose it are 1.2 cm^{-1}, 9.4 cm^{-1}, 10.1 cm^{-1} and 11.1 cm^{-1}. The resolution of the measurement is 0.2411 cm^{-1}. The three peaks located in the vicinity of 10 cm^{-1} indicate that something happens twice per turn of the threaded shaft of the translation stage (the thread is equal to 2 mm) but the presence of a peak located at 1.2 cm^{-1} is not explained yet. In a upgraded version of the carriage with a new motor, the series of peaks in the vicinity of 10 cm^{-1} was suppressed but the peak at 1.2 cm^{-1} was still present, along some of its harmonics. Also, it is possible to observe some very sharp oscillations (like the peak located at - 0.095 cm) in the instantaneous velocity of the carriage. They are due to a poor estimation of some of the zero-crossings, resulting in a not perfectly uniform-OPD sampling grid. This non-uniform-OPD grid may be responsible for the poor SNR as well. Further improvements of the zero-crossing detection and of the mechanics are necessary to allow for the measurement of high resolution spectra.

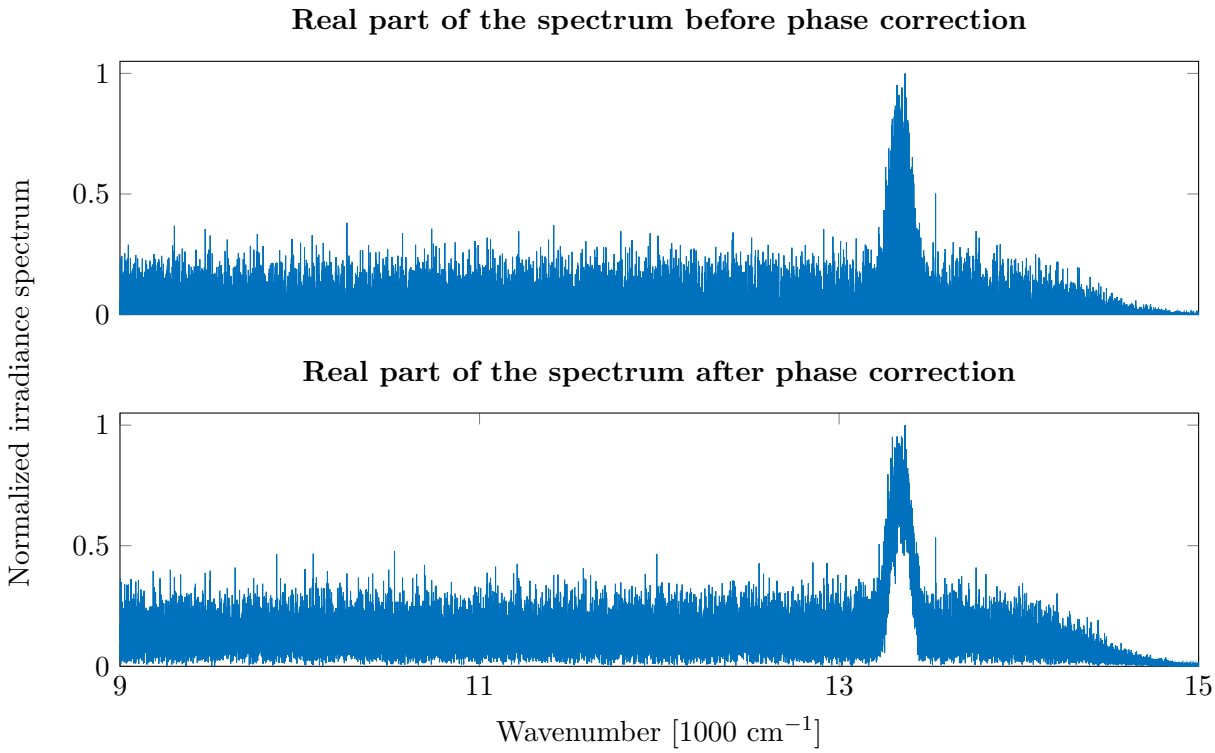

Figure 3.6: Comparison of the spectra before and after applying the phase correction.

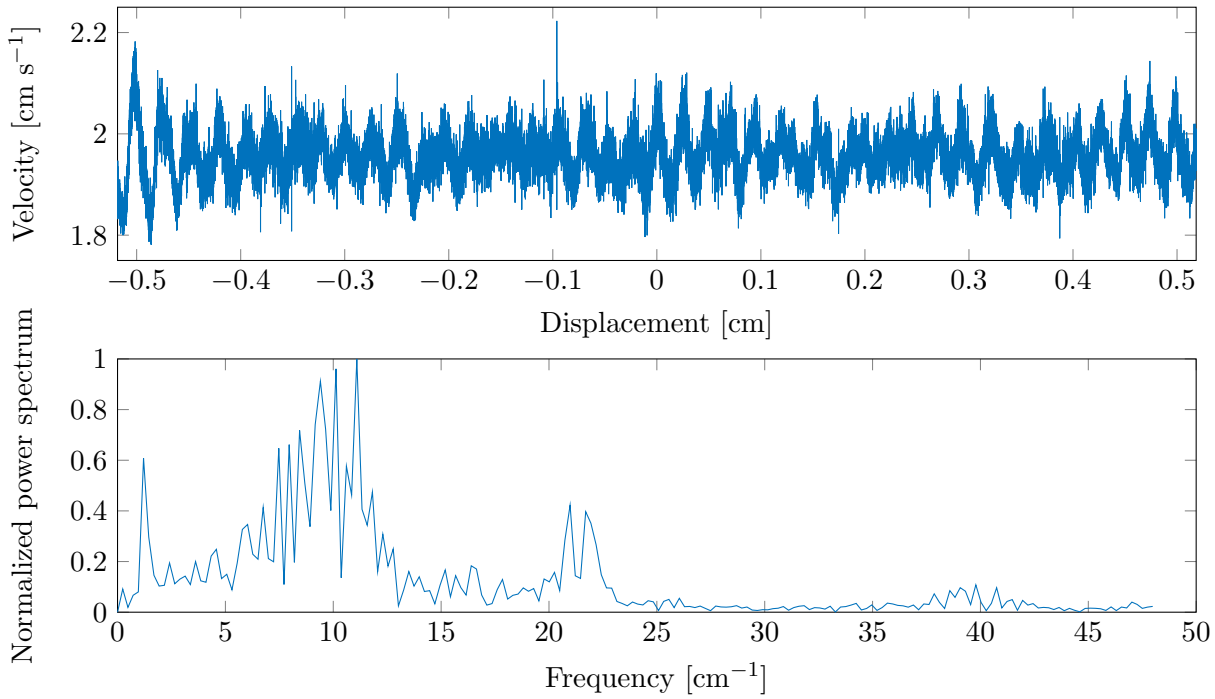

Figure 3.7: Instantaneous velocity of the carriage. Top : spatial domain. The origin of the x-axis corresponds to the optical contact. Bottom : Frequency domain.

3.3 Discussion

The aim of this section is to validate the results obtained with our homemade FTS by comparing them with two commercial spectrometers : the HR4000CG-UV-NIR grating spectrometer of Ocean optics and the OSA201 Fourier transform spectrometer of Thorlabs. To do so, the measurement of the transmittance of a FB750-10 optical filter was performed with the three instruments. Transmission with respect to the wavelength of the FB750-10 optical filter is given in Figure A.5.

The interferogram obtained with the homemade spectrometer is first compared with the one obtained with the OSA201 spectrometer in Figure 3.8. The maximum retardation of the OSA201 is twice longer for their spectrometer, leading to a higher resolution spectrum. However, while the measurement was taken with the maximum achievable resolution of the OSA201 (0.25 cm^{-1}), the maximum OPD can be considerably increased in the homemade spectrometer (about 35 times). The OSA201 and the homemade FTS are designed to measure double-sided interferograms. A structured pattern is observed on both sides of the centerburst of the OSA201 interferogram that is not present in ours. Both spectrometers make use of a 16 bits ADC. Surprisingly, the baseline of the interferogram of the OSA201 spectrometer is a bit inclined while the baseline of our interferogram is flat. This last feature is particularly interesting because it may explain why there are rapid oscillations in the peak of the OSA201 spectrum which is shown in Figure 3.9. Indeed, if the baseline of the reference laser interferogram is inclined as well, the uniform OPD grid sampling may not be correctly performed by the spectrometer. Nevertheless, the location of the Gaussian corresponding to the optical filter detected by our spectrometer and the one obtained with the OSA201 spectrometer do agree with the one of the calibrated grating spectrometer of Ocean Optics. It can be seen that the SNR ratio of the OSA201 is better than the one obtained with our spectrometer by a factor 3. However, the fluctuations in the Gaussian curve of the optical filter that are observed on the spectrum recorded with the OSA201 are not present in the spectrum of the homemade FTS. The general appearance of the spectrum recorded with the homemade FTS is more similar to the one recorded with the grating spectrometer than the spectrum recorded with the OSA201.

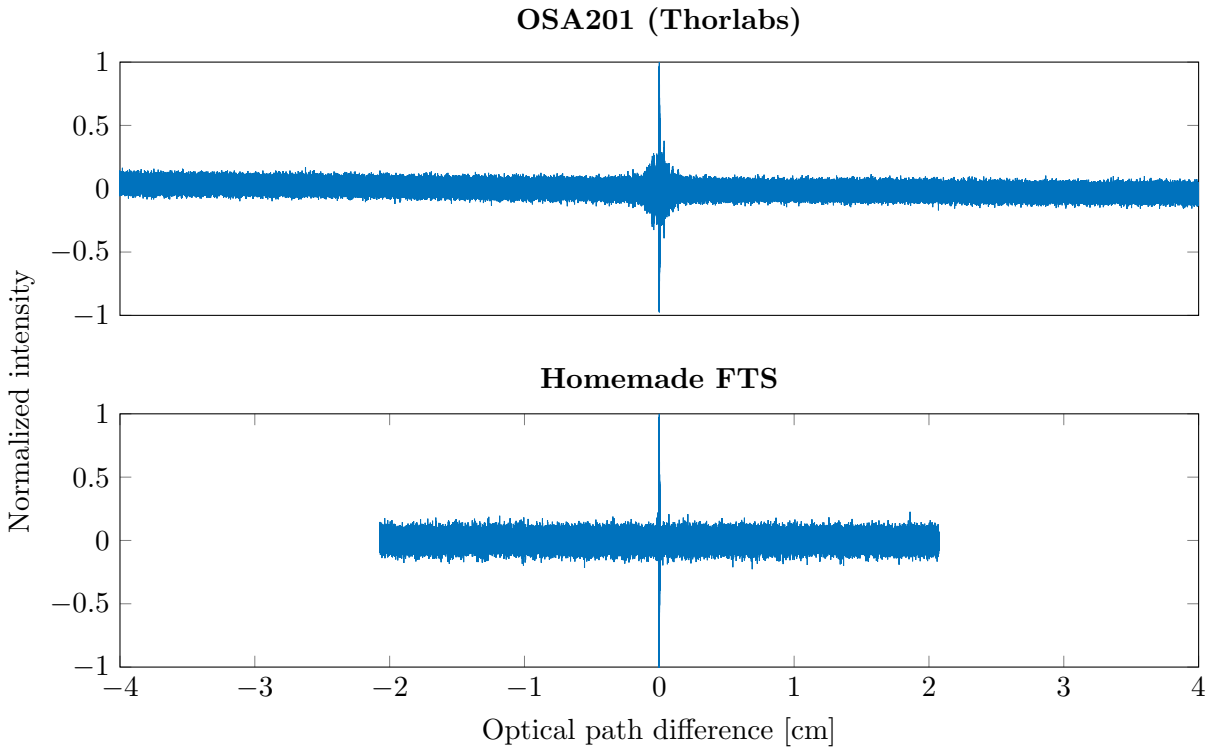

Figure 3.8: Comparison between the interferogram obtained with the OSA201 Fourier transform spectrometer of THORLABS and the resampled and filtered interferogram of the homemade Fourier transform spectrometer.

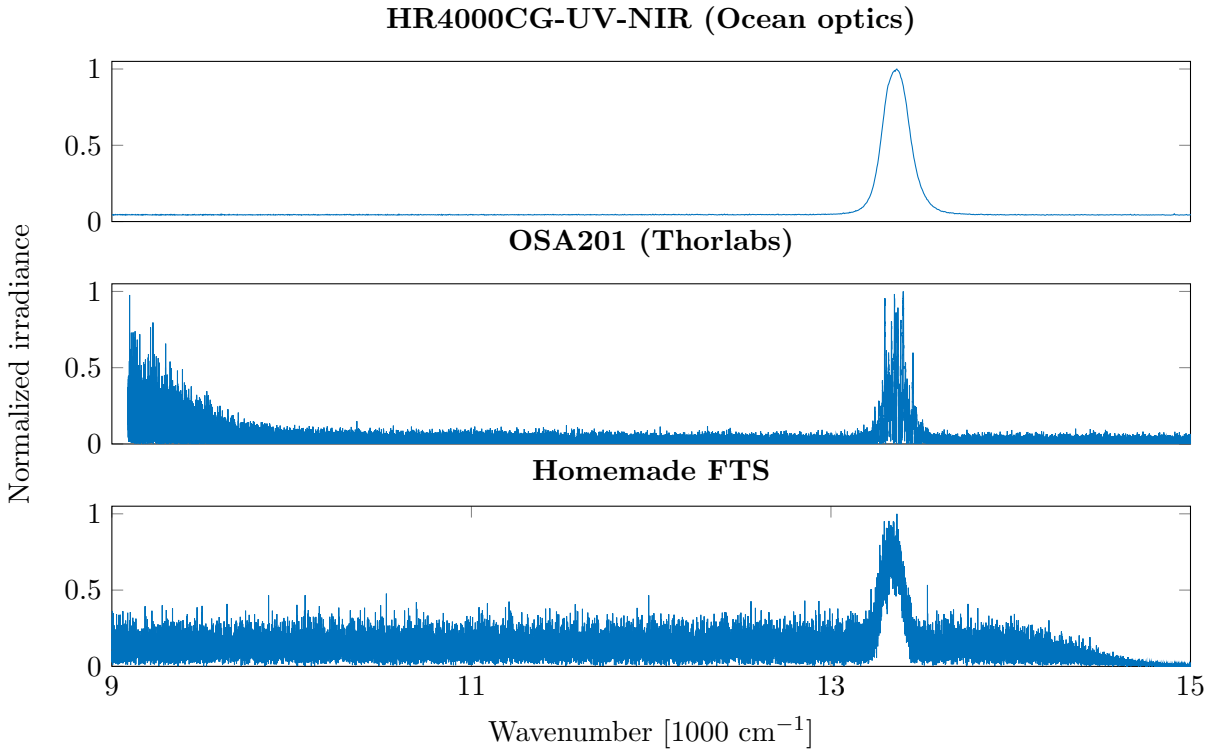

Figure 3.9: Comparison between the irradiance spectra obtained with the HR4000CG-UV-NIR grating spectrometer of OCEAN OPTICS (integration time : 100 ms, resolution : 1.77 cm^{-1}), the OSA201 Fourier transform spectrometer of THORLABS (resolution ADC : 16 bits, resolution : 0.25 cm^{-1}) and the homemade Fourier transform spectrometer (resolution : 0.48 cm^{-1}).

Conclusion

Fabrication of a homemade Fourier transform spectrometer is not a simple task. In order to obtain high quality spectra, these instruments require state-of-the-art technologies in mechanics, optics and electronics, but also an efficient data processing. The prototype that was built during the master thesis allowed to be aware of the numerous issues of such instruments but it also reassured us in the feasibility of the project. Indeed, a first low-resolution spectrum of an optical bandpass filter was measured at the end of the master thesis. The measurement was validated by comparing it with spectra taken with commercialized instruments. However, improvements that have to be done are numerous before meeting all the expectations of a good quality Fourier transform spectrometer.

Concerning the mechanics, the design of a new translation stage is necessary to keep variations in the carriage velocity and vibrations to a minimum. The actual threaded shaft of the translation stage is too long (1.5 meters) for its actual diameter (1 centimeter) and it bends under its own weight. A difference in height of about 2 milimeters is observed between the extremity of the shaft and its centre. This bending may be at the origin of the vibrations and it thus has to be avoided. One solution would be to increase the shaft diameter but it requires all the optical mounts to be changed because the height of the carriage would be modified. Another solution is to reduce the length of the threaded shaft, but this is done at the expanse of resolution. However, if single-sided interferograms are recorded instead of double-sided interferograms, the actual resolution can still be reached with shorter translations stages but it implies to implement a more elaborated algorithm than the actual one to correct the phase (it is necessary to first interpolate the phase on the complete spectrum from the knowledge of the phase on a small portion of negative OPD before applying the phase correction strictly speaking). If this phase correction algorithm is implemented, a last possibility would be to make use of commercialized translation stages designed especially for optical applications. Indeed, most of these translation stages are not longer than 60 centimeters. Advantage of using a commercialized translation stage is to ensure that the mechanics is flawless.

Improvements regarding the frequency-stabilized He:Ne laser are mandatory for the Fourier-transform spectrometer to work properly. Its non-reliability is a severe drawback of the actual instrument because it forces the user to check its stability before each measurement and to postpone it if necessary. Two solutions are conceivable: either the actual stabilization scheme has to be upgraded to make it reliable or a commercialized frequency-stabilized He:Ne laser is purchased. In the first case, the heaters could be replaced by Peltier cells or the duty point of the He:Ne laser could be modified by continuously heating the laser discharge tube with a moderate constant current flow. Doing so would permit to respond to any kind of perturbation, either by cooling down or heating up the discharge tube with the Peltier cell, or by increasing or decreasing the current flow in the heaters. In any case, a pre-heating system should be incorporated to decrease the time necessary to stabilize the laser (more than one hour is necessary for the moment).

The implementation of a software with an user interface that would incorporate the control of

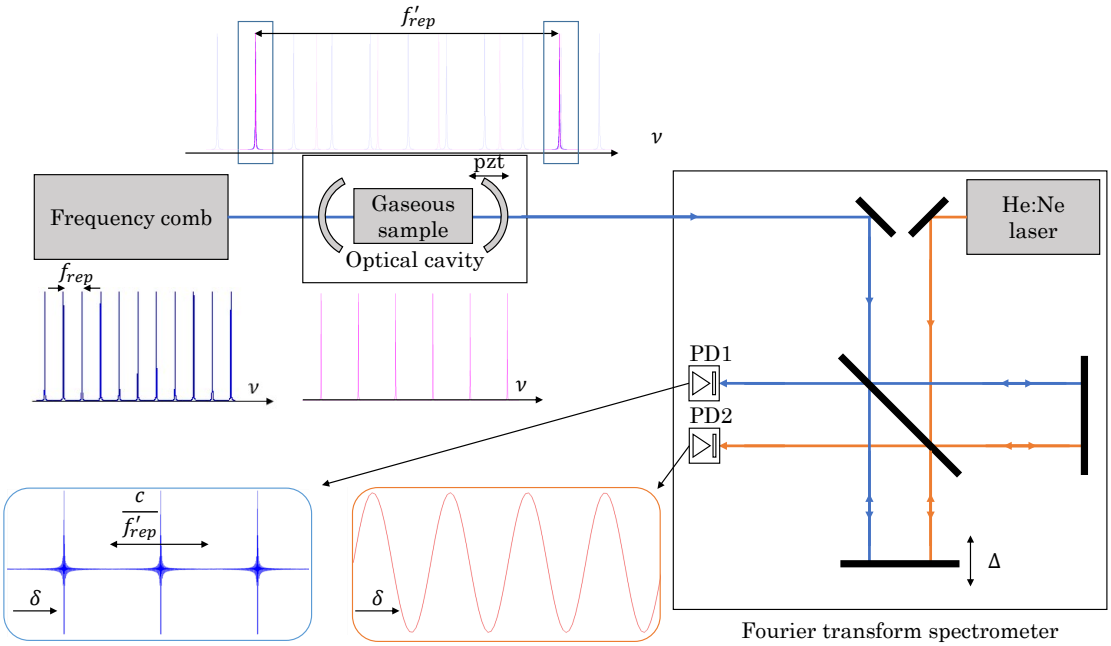

Figure: Scheme of the future setup. The Fourier transform spectrometer will be combined to a phase-stabilized frequency comb coupled with an optical cavity. PD stands for photodetector and pzt stands for piezoelectric crystal, ν is the frequency and δ is the OPD induced by a mechanical displacement Δ of the carriage.

the translation stage, the data acquisition and the data processing pipeline would make the instrument much more user-friendly. Also, it would be convenient to detect the zero-crossings at the hardware level via the method suggested by Brault (see section 3.2.2) in order to reduce the computation time of the irradiance spectrum from several hours to a few seconds. Moreover, high resolution spectroscopy implies to deal with huge amounts of data. These data have to be stored and processed. Another language should therefore supplant MATLAB to produce an efficient implementation regarding both throughput and storage in the future.

Once the FTS will be fully operational, perspectives associated with it will be numerous. One possibility would be to measure the molecular spectrum of any gas placed in a cell. Another possibility would be to combine the FTS with a supersonic expansion in order to record cold molecular spectra. Finally, the supercontinuum source of the Fourier transform spectrometer could be replaced by a femtosecond Ti:sapphire laser coupled with an optical cavity in order to considerably increase the sensitivity of the instrument. If doing so, the complete setup would look like the instrument depicted in the figure above. Benefits from using a femtosecond laser and an optical cavity in the setup are explained in the two following sections.

Cw lasers are characterized by a high spectral brightness and by the accurate knowledge of their emission frequency. These two features allow for highly sensitive and quantitative absorption measurements of molecules in the gas phase. However, this technique suffers from a severe drawback : its inability to study broadband spectra. Thankfully, the optical frequency combs that are generated by mode-locked femtosecond lasers allow to extend the advantages of cw laser absorption spectroscopy to the analysis of broadband spectra. They can be seen as the combination of thousands of lasers with narrow linewidths and with evenly spaced emission frequencies. Difference in emission frequency between adjacent teeth of the frequency comb, the so-called repetition frequency, can be maintained constant and is equal to f_{rep}. The phase shift between the carrier and the envelope in the time domain corresponds to an offset frequency f_0 in the frequency domain. The knowledge of both the repetition frequency and the offset

frequency allows to express unequivocally the frequency of all the teeth of the frequency comb [29]. One more thing is needed to perform spectroscopy with frequency combs : the ability to measure their spectral irradiance after their interaction with the gas sample under study. To do so, a Fourier transform spectrometer can be used. The signal-to-noise ratio of the FTS is enhanced and allows to reduce measurement times by orders of magnitude when combined with a femtosecond laser [34]. In contrast to conventional FTS, in comb-based FTS, the interferogram consists of a series of bursts spaced by a distance c/f_{rep} (where c is the velocity of light) instead of a single centerburst at ZPD. The interferogram is depicted in the figure of the previous page. In order to resolve the discrete modes of the optical frequency comb, the minimum optical path difference that has to be induced by the carriage displacement must be equal to c/f_{rep}. If the offset frequency and the repetition frequency do not vary during the measurement, recording an interferogram containing several bursts enhances the resolution [35]. But it is even more interesting to record the interferogram on an optical path difference that is exactly equal to c/f_{rep} because the sinc ILS due to the limited OPD (see Figure 1.7b of page 12) is such that there is no more crosstalk between the different teeth of the frequency comb after the Fourier transformation [34]. In the best case, resolution is limited by the linewidth of the teeth, which is about 10 kHz.

The optical cavity plays an important role in the setup : it considerably enhances the sensitivity of the instrument by increasing the interaction length of the femtosecond laser from a few centimeters to several kilometers. However, this is done at the expense of the instrument resolution since the repetition frequency of the frequency comb is modified by the cavity. The teeth of the frequency comb that are transmitted by the cavity are the ones that match with its longitudinal modes, as shown in the figure above. However, acquiring several interferograms with different repetition frequencies permits to increase the resolution again [34].

Bibliography

[1] A. D. McNaught and A. Wilkinson, *IUPAC gold book : Compendium of chemical terminology*. Blackwell Scientific Publications, 1997.

[2] E. Kretschmer, *Modelling of the instrument spectral response of conventional and imaging fourier transform spectrometers*. Université Laval, 2014.

[3] A. Matveev, C. G. Parthey, K. Predehl, J. Alnis, A. Beyer, R. Holzwarth, T. Udem, T. Wilken, N. Kolachevsky, M. Abgrall, *et al.*, "Precision measurement of the hydrogen 1 s- 2 s frequency via a 920-km fiber link," *Physical Review Letters*, vol. 110, no. 23, p. 230801, 2013.

[4] M. A. D. Sumner and J. Brault, *Fourier transform spectrometry*. Academic Press, 2001.

[5] V. Saptari, *Fourier transform spectroscopy instrumentation engineering*. SPIE Optical Engineering Press, 2003.

[6] C. A. Michaels, T. Masiello, and P. M. Chu, "Fourier transform spectrometry with a near-infrared supercontinuum source," *Applied spectroscopy*, vol. 63, no. 5, pp. 538–543, 2009.

[7] P. Griffiths and J. De Haseth, *Fourier transform infrared spectrometry*, vol. 171. John Wiley & Sons, 2007.

[8] E. Hecht, *Optics*. Addison-Wesley world student series, Addison-Wesley, 1998.

[9] J. Genest and P. Tremblay, *Understanding Fourier-transform spectrometers*. Centre d'optique, photonique et laser, Université Laval, 20017.

[10] W. Perkins, "Fourier transform-infrared spectroscopy: Part l. instrumentation," *Journal of Chemical Education*, vol. 63, no. 1, p. A5, 1986.

[11] T. Deleporte, *Quantitative infrared Fourier transform spectroscopy: absolute intensities for 13CO2 and HOBr*. PhD thesis, Université Libre de Bruxelles, 2008.

[12] S. Haykin and B. V. Veen, *Signals and systems*. John Wiley & Sons, 2007.

[13] Thorlabs, "Protected silver mirrors." `https://www.thorlabs.de/newgrouppage9.cfm?objectgroup_id=903`. Accessed 15 july 2016.

[14] K. C. Cossel, *Techniques in molecular spectroscopy : from broad bandwidth to high resolution*. PhD thesis, California Institute of Technology, 2007.

[15] Thorlabs, "Polarization change after propagation through a prism retroreflector,"

[16] S. Hooker and C. Webb, *Laser Physics*. Oxford Master Series in Physics, OUP Oxford, 2010.

[17] I. optics & photonics marketplace, "Gaussian beam optics." `http://marketplace.idexop.com/store/SupportDocuments/All_About_Gaussian_Beam_OpticsWEB.pdf`. Accessed 16 june 2016.

[18] F. company, "Whitelase sc series." http://www.fianium.com/pdf/WhiteLase_SC400_UV_v1.pdf. Accessed 29 may 2016.

[19] J. Kauppinen and P. Saarinen, "Line-shape distortions in misaligned cube corner interferometers," *Applied optics*, vol. 31, no. 1, pp. 69–74, 1992.

[20] T. Eom, H. Choi, and S. Lee, "Frequency stabilization of an internal mirror he–ne laser by digital control," *Review of scientific instruments*, vol. 73, no. 1, pp. 221–224, 2002.

[21] L. Luhs, "Hene laser frequency stabilization," *LD didactic*, vol. reference note 4747111, 2012.

[22] Y. Zhao, "Implementing thermal feedback control of a helium-neon laser for frequency stabilization," 2008.

[23] R. Balhorn, H. Kunzmann, and F. Lebowsky, "Frequency stabilization of internal-mirror helium–neon lasers," *Applied optics*, vol. 11, no. 4, pp. 742–744, 1972.

[24] Thorlabs, "Pid tutorial." http://www.thorlabs.de/tutorials.cfm?tabID=5dfca308-d07e-46c9-baa0-4defc5c40c3e. Accessed 15 june 2016.

[25] G. Woolsey, M. Y. Sulaiman, and M. Mokhsin, "Correlation of changes in laser tube temperature, cavity length, and beam polarization for an internal-mirror helium–neon laser," *American Journal of Physics*, vol. 50, no. 10, pp. 936–940, 1982.

[26] X. Diao, J. Tan, P. Hu, H. Yang, and P. Wang, "Frequency stabilization of an internal mirror he–ne laser with a high frequency reproducibility," *Applied optics*, vol. 52, no. 3, pp. 456–460, 2013.

[27] J. W. Brault, "New approach to high-precision fourier transform spectrometer design," *Applied Optics*, vol. 35, no. 16, pp. 2891–2896, 1996.

[28] H. Yang, P. R. Griffiths, and C. J. Manning, "Improved data processing by application of brault's method to ultra-rapid-scan ft-ir spectrometry," *Applied spectroscopy*, vol. 56, no. 10, pp. 1281–1288, 2002.

[29] A. Foltynowicz, T. Ban, P. Masłowski, F. Adler, and J. Ye, "Quantum-noise-limited optical frequency comb spectroscopy," *Physical review letters*, vol. 107, no. 23, p. 233002, 2011.

[30] D. A. Naylor, T. R. Fulton, P. W. Davis, I. M. Chapman, B. G. Gom, L. D. Spencer, J. V. Lindner, N. E. Nelson-Fitzpatrick, M. K. Tahic, and G. R. Davis, "Data processing pipeline for a time-sampled imaging fourier transform spectrometer," in *Optical Science and Technology, the SPIE 49th Annual Meeting*, pp. 61–72, International Society for Optics and Photonics, 2004.

[31] W. Herres and J. Gronholz, "Understanding ft-ir data processing," *Part*, vol. 1, pp. 352–356, 1984.

[32] A. Ben-David and A. Ifarraguerri, "Computation of a spectrum from a single-beam fourier-transform infrared interferogram," *Applied optics*, vol. 41, no. 6, pp. 1181–1189, 2002.

[33] M. L. Forman, W. H. Steel, and G. A. Vanasse, "Correction of asymmetric interferograms obtained in fourier spectroscopy," *JOSA*, vol. 56, no. 1, pp. 59–63, 1966.

[34] P. Maslowski, K. F. Lee, A. C. Johansson, A. Khodabakhsh, G. Kowzan, L. Rutkowski, A. A. Mills, C. Mohr, J. Jiang, M. E. Fermann, *et al.*, "Surpassing the path-limited resolution of fourier-transform spectrometry with frequency combs," *Physical Review A*, vol. 93, no. 2, p. 021802, 2016.

[35] M. Zeitouny, P. Balling, P. K**r**en, P. Ma**s**ika, R. C. Horsten, S. T. Persijn, H. P. Urbach, and N. Bhattacharya, "Multi-correlation fourier transform spectroscopy with the resolved modes of a frequency comb laser," *Annalen der Physik*, vol. 525, no. 6, pp. 437–442, 2013.